

# Impacts of Sequential Microbial Electron Accepting Processes on Natural Attenuation of Selected Petroleum Hydrocarbons in the Subsurface Environment

J. Steven Brauner

Dissertation submitted to the Faculty of  
Virginia Polytechnic Institute and State University  
in partial fulfillment of the requirements for the degree of:

Doctor of Philosophy  
in  
Civil and Environmental Engineering

Advisory Committee:

Dr. M.A. Widdowson, Chair

Dr. T.J. Burbey

Dr. G.V. Loganathan

Dr. N.G. Love

Dr. J.T. Novak

February 2000  
Blacksburg, VA 24061

Key Words: groundwater, petroleum, bioremediation, natural attenuation, modeling

Copyright 2000, J. Steven Brauner

# Impacts of Sequential Microbial Electron Accepting Processes on Natural Attenuation of Selected Petroleum Hydrocarbons in the Subsurface Environment

J. Steven Brauner

*The Charles E. Via, Jr. Department of Civil and Environmental Engineering*

## (ABSTRACT)

Regulatory acceptance of monitored natural attenuation (MNA) requires demonstration that natural processes, such as sorption and biodegradation, attenuate specific contaminants of concern on a time scale that is comparable to other remediation options while concurrently preventing contaminant migration to site-specific points of contact. Two of the tools used to demonstrate the efficacy of MNA, microcosm experiments and numerical fate and transport modeling, were examined in this study. In the first phase of this work, laboratory microcosm studies were initiated as part of an overall MNA site assessment to determine whether a native microbial consortia collected with a soil sample from a petroleum-hydrocarbon contaminated site was capable of biodegrading specific polynuclear aromatic hydrocarbon (PAH) compounds. Results indicated that selected PAH compounds were biodegraded under simulated natural conditions using oxygen and sulfate as electron acceptors. In the second phase of this study, a numerical experiment was conducted using the three-dimensional, multiple substrate, multiple electron acceptor fate and transport model SEAM3D (Waddill and Widdowson, 1997) to evaluate the impact of including iron(III)-reducing conditions during numerical simulations of natural attenuation. Results for this phase of the study indicated that the mass of hydrocarbon simulated as biodegraded by the iron(III)-reducing population was significantly larger than hydrocarbon biodegradation under aerobic conditions. The final component of research used the SEAM3D model to interpret field observations recorded during a natural attenuation experiment where the fate and transport of selected hydrocarbon contaminants (BTEX and naphthalene) was tracked through an extremely heterogeneous, but well-instrumented test aquifer. Results from the calibrated model for the NATS experiment indicated that the majority of the contaminant remained in the non-aqueous phase during the first year of the experiment, and that aerobic biodegradation was the dominant natural attenuation process. Model results were particularly sensitive to the rate of contaminant release and the starting mass of electron acceptor.

## ACKNOWLEDGEMENTS

I am forever indebted to the Via Foundation of Virginia Tech's Charles Edward Via, Jr. Department of Civil and Environmental Engineering for the Via Scholar Fellowship that financially contributed to three-years and a half years of my doctoral education. My freedom to explore new and challenging problems was notably facilitated by the financial support offered from this fellowship.

I am also deeply appreciative of the support, advice, guidance, and friendship from my major advisor, Dr. Mark Widdowson. His support of my endeavors, both academically and personally, made it possible for me to learn and experience more than I could have ever imagined during the four years of my doctoral education.

This quality of this work was greatly improved with the advice and critical review offered by the members of my advisory committee. I am grateful for their patience in answering my questions, prudence in guiding my work, and encouragement to keep looking deeper into the topics discussed in this work.

Much appreciation is also extended to Dan Waddill and Marc Killingstad for their friendship and sharing of ideas on how to model natural attenuation. I am also thankful for the many friends who shared in the good times here in Blacksburg.

I am also indebted to my parents, John and Judy Brauner, who, from the earliest time that I can remember, instilled in me a desire to learn and explore new ideas, while also reminding me to take some time to enjoy life each day. Their love, support, and faith in me were a constant source of inspiration during this work.

Finally, I am grateful for the love and support from Jennifer, my soul mate and best friend. It may not be possible to put into words how deeply I appreciate her encouragement during the countless days and nights that I was in the office or laboratory, working on this dissertation. We did it!

## TABLE OF CONTENTS

Abstract .....	ii
Acknowledgements.....	iii
Table of Contents.....	iv
List of Tables.....	vii
List of Figures.....	ix
<b>CHAPTER 1. INTRODUCTION .....</b>	<b>1</b>
BACKGROUND.....	1
OBJECTIVES AND SCOPE .....	1
REFERENCES.....	3
<b>CHAPTER 2. LITERATURE REVIEW .....</b>	<b>4</b>
THE BIODEGRADATION ENVIRONMENT .....	4
ELECTRON TOWER THEORY AND SEQUENTIAL ELECTRON ACCEPTORS .....	4
PETROLEUM HYDROCARBON REMOVAL BY SEQUENTIAL ELECTRON ACCEPTOR PROCESSES .....	5
MODELING NATURAL ATTENUATION OF PETROLEUM HYDROCARBONS .....	7
REFERENCES.....	9
<b>CHAPTER 3. BIODEGRADATION OF SELECTED POLYCYCLIC AROMATIC-     HYDROCARBONS BY NATIVE MICROBIAL POPULATIONS UNDER     SIMULATED NATURAL CONDITIONS.....</b>	<b>12</b>
ABSTRACT.....	12
INTRODUCTION.....	12
EXPERIMENTAL SECTION .....	14
Site selection and soil collection. ....	14
Microcosm construction.....	14
Analytical Methods.....	15
Degradation Rate Estimation.....	15
Stoichiometric Mass Balance Procedure.....	16
RESULTS AND DISCUSSION.....	18
PAH Degradation and Electron Acceptor Disappearance.....	18

Mass Balance Analysis.....	20
Variability in PAH Degradation with Location.....	21
ACKNOWLEDGEMENTS .....	23
LITERATURE CITED	33
<b>CHAPTER 4. INVESTIGATION OF IRON(III)-BASED DEGRADATION OF PETROLEUM HYDROCARBONS: MATHEMATICAL MODELING AS AN INTERPRETIVE TOOL .....</b>	<b>34</b>
ABSTRACT .....	34
INTRODUCTION .....	35
HYPOTHETICAL MODEL .....	38
Model Assumptions.....	38
Groundwater Flow Model and Numerical Grid.....	39
Hydraulic Conductivity Field .....	40
Solute Transport Model .....	40
Solute Transport and Biodegradation Parameters .....	43
Iron(III) Concentration and Distribution .....	45
METHOD OF ANALYSIS.....	45
RESULTS .....	47
Tracer and Aerobic Biodegradation .....	47
Sequential Aerobic/Ferrogenic Biodegradation .....	47
Variation in Iron(III) Concentration .....	51
Variation in Iron(III) Distribution .....	54
Iron(III) Distribution Correlated to Hydraulic Conductivity.....	55
Microbial Population Correlated to Hydraulic Conductivity .....	56
Sensitivity of Results to Hydraulic Conductivity Distribution .....	57
SUMMARY AND CONCLUSIONS .....	60
ACKNOWLEDGEMENTS .....	62
REFERENCES.....	86
<b>CHAPTER 5. NUMERICAL SIMULATION OF A NATURAL ATTENUATION EXPERIMENT WITH A NAPL SOURCE: CONTAMINANT DISSOLUTION AND REACTIVE TRANSPORT .....</b>	<b>89</b>
ABSTRACT.....	89
INTRODUCTION.....	90
PREVIOUS WORK	91

NATS EXPERIMENT: HYDROCARBON AND GEOCHEMICAL	
OBSERVATIONS .....	93
Hydrocarbon and TEAP Distribution.....	93
Variability in Hydrocarbon Biodegradation .....	94
CONCEPTUAL MODEL .....	94
Solutes.....	96
Sorption, Phase Transfer, and the Dual Domain Approach .....	96
NAPL Release .....	97
Biodegradation .....	97
NUMERICAL MODEL.....	97
Reactive Solute Transport Model.....	97
Grid Design and Boundary Conditions.....	98
Single Porosity Model: Governing Equations.....	99
Dual Domain Model: Governing Equations.....	100
NAPL Dissolution .....	100
Biodegradation Kinetics.....	101
MODEL PARAMETER SELECTION .....	103
Solute Transport and Phase Transfer Parameters .....	103
NAPL Dissolution Parameters .....	103
Biodegradation Parameters .....	104
RESULTS AND DISCUSSION.....	104
Model Calibration.....	104
Single Porosity Model.....	105
Dual Domain Model .....	107
Model Sensitivity.....	108
PHC Attenuation .....	109
CONCLUSIONS .....	110
REFERENCES.....	132
Vita .....	135

## LIST OF TABLES

### CHAPTER 3.

Table 1. Oxidation-Reduction Reactions for PAH Mineralization to Carbon Dioxide under Aerobic and Sulfate-reducing Conditions, Assuming Zero Biomass Yield. (Modified from (14)) .....	24
Table 2. Electron Acceptor Use Coefficients by PAH and Electron Acceptor Condition for Stoichiometric Calculations Assuming Zero Biomass Yield.....	25
Table 3. Oxidation-reduction Reactions for PAH Mineralization to CO <sub>2</sub> Under Aerobic and Sulfate-reducing Conditions, Assuming Biomass Growth Using a Non-limiting Mass of Reduced Nitrogen. Yield Coefficients (mg <sub>biomass</sub> /mg <sub>PAH</sub> ) for the Aerobic and Sulfate-reducing Microbial Populations Were 0.33 and 0.06, Respectively. . . . .	26
Table 4. Electron Acceptor Use for Stoichiometric Calculations when Yield Coefficients (mg <sub>biomass</sub> /mg <sub>PAH</sub> ) of 0.33 and 0.06 were used for the Aerobic and Sulfate-reducing Microbial Populations, Respectively. . . . .	27
Table 5. First-order Rate Constants, Confidence Intervals, and R-Squared Coefficients for Disappearance of Selected PAH Compounds in Microcosms Containing Soil from Site A. ....	28
Table 6. Stoichiometric Accounting for PAH Mass Loss in the Site A Live Microcosms.....	29
Table 7. Comparison of First-order Rate Constants in Microcosms Containing Either Soil A or Soil B.....	30

### CHAPTER 4.

Table 1. Statistical parameters for the hydraulic conductivity field, as reported by Carsel and Parrish (1988).....	63
Table 2. Solute transport parameters for the hypothetical transport model. ....	64
Table 3. Biodegradation parameters for the hypothetical reactive solute transport model. ....	65
Table 4. Designations used to identify assumptions for a given simulation. For example, Case A3 was a simulation using hydraulic conductivity distribution 'A' and a heterogeneous iron(III) distribution of 150 µg Fe <sup>3+</sup> /g soil. ....	66

### CHAPTER 5.

Table 1. Range of values for the retardation factor and first-order biodegradation rate for benzene, p-xylene, and naphthalene reported from MADE-2 (Boggs et al., 1993).....	113
---	-----

Table 2. Composition and chemical properties of the NAPL source for the NATS experiment. Solubility, molecular weight, and initial percentage of the NAPL (by weight) were required SEAM3D input parameters .....	114
Table 3. SEAM3D input parameters for aquifer, soil, and PHC sorption properties. ....	115
Table 4. Biodegradation parameters for microbial kinetics, inhibition, electron acceptor consumption and reaction endproduct formation .....	116
Table 5. Maximum specific utilization rates ( $n_{x,ls,le}^{max}$ ) and initial microbial population concentration ( $M_x$ ) for each simulated electron acceptor condition. NS means that hydrocarbon biodegradation was not simulated for that electron accepting condition .....	117

## LIST OF FIGURES

### CHAPTER 2.

- Figure 1. Electron acceptor utilization sequence determined by electron potential energies. (After Suflita and Sewell, 1991) ..... 5
- Figure 2. Spatial variation of electron acceptor conditions for a typical groundwater contaminant plume. (Adapted from Lyngkilde et al., 1991) ..... 6
- Figure 3. Microbially mediated contaminant removal by sequential microbial (aerobic/iron(III)-reducing/sulfate-reducing) electron accepting processes ..... 7

### CHAPTER 3.

- Figure 1. PAH concentration versus time for (A) acenaphthene, (B) fluorene, (C) phenanthrene, (D) pyrene, and (E) benzo(b)fluoranthene in microcosms containing soil from Site A. The dash dotted (— · ·) line represents the best fit regression line for the control microcosms. The solid (—) line represents the best fit through the live microcosms during the ‘active’ phase, while the dashed (— —) line represents the best fit line during periods when the live microcosms were inactive. Error bars represent  $\pm$  one standard deviation in the concentration measurement. .... 31
- Figure 2. PAH concentration versus time for (A) acenaphthene, (B) fluorene, (C) phenanthrene, and (D) pyrene in microcosms containing soil from Site B. The dash dotted (— · ·) line represents the best fit regression line for the control microcosms. The solid (—) line represents the best fit through the live microcosms during the ‘active’ phase, while the dashed (— —) line represents the best fit line during periods when the live microcosms were inactive. Error bars represent  $\pm$  one standard deviation in the concentration measurement. (Modified from (12).) ..... 32

### CHAPTER 4.

- Figure 1. Boundary conditions and dimensions for hypothetical numerical model domain. .... 67
- Figure 2. Cross sections of hydraulic conductivity distribution ‘A’ through the vertical ( $z = 1.5$  m) and horizontal ( $y = 10$  m) centerlines of the model domain..... 68
- Figure 3. Horizontal and vertical cross sections through the centerline of the model domain depicting tracer (top row), hydrocarbon (middle row) and oxygen distributions (bottom row) for Case A0, taken at 1000 (left column) and 2000 (right column) days into the simulation. Hydrocarbon biodegradation for Case A0 was simulated under aerobic conditions. .... 69

Figure 4. Horizontal and vertical cross sections through the centerline of the model domain depicting hydrocarbon (top row), oxygen (middle row), and Fe <sup>3+</sup> distribution (bottom row) for Case A1, taken at 1000 (left column) and 2000 (right column) days into the simulation. Hydrocarbon biodegradation in Case A1 was simulated under sequential aerobic/Fe <sup>3+</sup> -reducing conditions for a uniform initial Fe <sup>3+</sup> concentration of 100 µg Fe <sup>3+</sup> /g soil.....	70
Figure 5. Tracer and hydrocarbon mass remaining in the model domain (A) and cumulative hydrocarbon mass biodegraded (B) as a function of time for model Cases A0 and A1. ....	71
Figure 6. Spatial moments versus time for the centroid (left column) and spatial standard deviation (right column) in the longitudinal (x), transverse (y), and vertical (z) directions for the tracer, aerobically biodegraded hydrocarbon (A0), and sequentially biodegraded hydrocarbon (A1).....	72
Figure 7. Tracer and hydrocarbon breakthrough curves at hypothetical monitoring points MP1 and MP2 for the aerobic only (A0) and sequential aerobic/ferrogenic (A1) biodegradation cases. ....	73
Figure 8. Horizontal hydrocarbon and electron acceptor distributions at z = 1.5 m and 2000 days for Case A2 (left column, [Fe <sup>3+</sup> ] = 50 µg Fe <sup>3+</sup> /g soil) and Case A3 (right column, [Fe <sup>3+</sup> ] = 150 µg Fe <sup>3+</sup> /g soil). ....	74
Figure 9. Tracer and hydrocarbon mass remaining in the model domain (A) and location of the longitudinal center of mass (B) versus time for Cases A0 through A3.....	75
Figure 10. Percentage of hydrocarbon biodegraded by each electron acceptor process. ..	76
Figure 11. Hydrocarbon breakthrough curves at hypothetical monitoring points MP1 and MP2 for initial Fe <sup>3+</sup> concentrations of 50 µg Fe <sup>3+</sup> /g soil (Case A2), 100 µg Fe <sup>3+</sup> /g soil (Case A1), and 150 µg Fe <sup>3+</sup> /g soil (Case A3). ....	77
Figure 12. Hydrocarbon (top), initial Fe <sup>3+</sup> (middle), and 2000 day Fe <sup>3+</sup> (bottom) concentrations at z = 1.5 m and 2000 days for Cases A4 (left) and Case A5 (right). ....	78
Figure 13. Hydrocarbon (top), initial Fe <sup>3+</sup> (middle), and 2000-day Fe <sup>3+</sup> (bottom) concentration distributions at z = 1.5 m for simulations using an initial Fe <sup>3+</sup> concentration distribution that was correlated to hydraulic conductivity (Case A6). ....	79
Figure 14. Hydrocarbon (top) and oxygen (bottom) concentration distributions for simulations using microbial population distributions that are correlated to hydraulic conductivity at 1000 days (left) and 2000 days (right) into simulation A7.....	80

Figure 15. Longitudinal spatial moments calculations for the tracer and hydrocarbon of Cases A1, A6, A7, and A8 when either the Fe <sup>3+</sup> concentration (A6), the microbial populations (A7), or both (A8) are correlated to hydraulic conductivity distribution A.....	81
Figure 16. Cross sections of hydraulic conductivity distribution ‘B’, taken through the vertical (z = 1.5 m) and horizontal (y = 10 m) centerlines of the model domain. ....	82
Figure 17. Horizontal and vertical cross sections through the centerline of the model domain depicting tracer (top row) and hydrocarbon distribution for Cases B0 (middle row) and B1 (bottom row), taken at 1000 (left column) and 2000 (right column) days into the simulation. Hydrocarbon biodegradation was simulated under aerobic conditions for Case B0 and under sequential aerobic/Fe <sup>3+</sup> -reducing conditions for Case B1. ....	83
Figure 18. Horizontal and vertical cross sections through the centerline of the model domain depicting oxygen for Cases B0 (top row) and B1 (middle row) and Fe <sup>3+</sup> for Case B1 (bottom row), taken at 1000 (left column) and 2000 (right column) days into the simulation. Hydrocarbon biodegradation was simulated under aerobic conditions for Case B0 and under sequential aerobic/Fe <sup>3+</sup> -reducing conditions for Case B1. ....	84
Figure 19. Method of moments calculations for the hydrocarbon mass remaining in the model domain (A) and the location of the longitudinal centroid, x <sub>c</sub> (B) as a function of time for model simulations through hydraulic conductivity field ‘B’. ....	85
<b>CHAPTER 5 .</b>	
Figure 1. NATS test site location map and orientation map for model domain relative to multi-level sampling locations and the NAPL source trench location .....	118
Figure 2. Correlation between contaminant contours (ppm) and hydraulic conductivity for a vertical slice taken 4 m west of the source trench centerline at Snapshot 3. The top figure depicts toluene concentrations, while the bottom figure is for ethylbenzene .....	119
Figure 3. Electron acceptor and reaction endproduct concentration distributions at Snapshots 3 and 4. All cross sections are taken 4-m west of the source centerline, as shown in Figure 1 .....	120
Figure 4. Comparison of field measured toluene and ethylbenzene concentrations for all monitoring points. Filled diamonds (◆) are for Snapshot 3 and empty diamonds (◇) are for Snapshot 4 .....	121
Figure 5. Comparison of field measured benzene and ethylbenzene concentrations for all monitoring points. Filled diamonds (◆) are for Snapshot 3 and empty diamonds (◇) are for Snapshot 4 .....	122

Figure 6. Hydraulic conductivity distribution immediately down-gradient of the NAPL source area .....	123
Figure 7. Comparison of field measured BTEX and naphthalene concentrations with model simulations for the single porosity model along a vertical cross section 4-m west of the source centerline for Snapshot 3 .....	124
Figure 8. Comparison of field measured BTEX and naphthalene concentrations with model simulations for the single porosity model along a vertical cross section 4-m west of the source centerline for Snapshot 4 .....	125
Figure 9. Comparison of field measured toluene concentrations with model simulated values for a horizontal cross section at z = 60m at Snapshots 3 and 4 .....	126
Figure 10. Comparison of model calculated toluene and ethylbenzene concentrations for all monitoring points. Filled diamonds (◆) are for Snapshot 3 and empty diamonds (◇) are for Snapshot 4 .....	127
Figure 11. Comparison of model calculated benzene and ethylbenzene concentrations for all monitoring points. Filled diamonds (◆) are for Snapshot 3 and empty diamonds (◇) are for Snapshot 4 .....	128
Figure 12. Model calculated electron acceptor and reaction endproduct concentration distributions at Snapshots 3 and 4 for the single porosity reactive transport model. All cross sections are taken 4-m west of the source centerline .....	129
Figure 13. BTEX and naphthalene concentrations for model simulations using the dual domain reactive transport model along a vertical cross section 4-m west of the source centerline for Snapshots 3 and 4 .....	130
Figure 14. Mass balance calculations for hydrocarbon transformation at Snapshots 3 and 4. ....	131

# CHAPTER 1

## Introduction

### Background

Environmental and public health concerns over the carcinogenic properties of certain petroleum hydrocarbon compounds has brought increasing attention to the uncontrolled release of xenobiotic petroleum hydrocarbons into the subsurface environment. Active remediation strategies, such as pump and treat, soil excavation, and air-sparging, are generally successful at short-term removal of aqueous phase hydrocarbon contaminants, but these techniques may be expensive in both energy and economic requirements. Additionally, long term monitoring of aqueous phase contaminant concentrations at some sites shows that contaminant levels may increase with time after the active remediation has stopped. This rebound in aqueous phase contaminant concentration is attributed to desorption of sorbed contaminants from the aquifer media back into the bulk pore water. The desire to reduce financial costs while permanently removing petroleum contaminants has led to increased interest in determining whether natural *in situ* processes, collectively grouped under the term natural attenuation, may serve as an effective petroleum contaminant remediation strategy.

Research over the last two decades has shown that biologically mediated redox reactions under aerobic and anoxic conditions can permanently remove many petroleum hydrocarbon contaminants *in situ*. The more recent discovery of additional *in situ* processes, such as naturally occurring iron(III) and sulfate based biodegradation of petroleum contaminants, has the potential to make natural attenuation a realistic and cost-effective alternative in the effort to clean the nation's groundwater.

### Objectives and Scope

As indicated by the USEPA (1999), regulatory acceptance of monitored natural attenuation (MNA) requires that natural processes attenuate the contaminants of concern on a time scale that is comparable to other remediation options while concurrently preventing contaminant migration to site-specific points of contact. The common theme for the three phases of research presented in this study was to that each investigation corresponded to a different

aspect of MNA site assessment. A brief review of previous research into petroleum hydrocarbon biodegradation in the subsurface under sequential electron accepting conditions is provided as background in Chapter 2. Chapter 3 contains the method and results from a laboratory microcosm study that was conducted as part of an larger MNA site assessment for a No. 2 fuel oil-contaminated site located in the Atlantic Coastal Aquifer of northeastern Virginia. Specifically, the objective of this microcosm experiment was to determine whether a native microbial population, collected with a soil sample at highly contaminated location, was able to biologically transform specific polycyclic aromatic hydrocarbon compounds (PAH) under simulated *in situ* conditions. If biodegradation was shown to occur, the secondary objective of the microcosm study was to estimate rates of biodegradation for each PAH compound that could then be used in the larger MNA assessment to estimate a time until contaminant removal.

The impact of iron(III)-based biodegradation on numerical model simulations of natural attenuation was investigated using a series of numerical experiments, as discussed in Chapter 4. Multiple researchers have shown that iron(III)-based biodegradation of hydrocarbons is occurring at petroleum hydrocarbon-contaminated sites (e.g. Lovely et al., 1994), but few attempts have been made to assess the impact of including iron(III)-based biodegradation in numerical modeling of MNA. The impact of including iron(III)-based biodegradation in modeling of MNA was quantified via a series of numerical experiments in a hypothetical heterogeneous aquifer that simulated hydrocarbon biodegradation under sequential aerobic and iron(III)-reducing (i.e. ferrogenic) conditions using the SEAM3D solute transport model (Waddill and Widdowson, 1997). Variation in the initial iron(III) concentration and distribution was investigated during this study, and the implications of model results on MNA site assessment was discussed.

Numerical models provide unique insights into MNA site assessment by aiding in both the interpretation of collected solute concentration data and future predictions of contaminant fate and transport. In Chapter 5, both a conceptual and numerical model are developed for the Natural Attenuation Study (NATS) field experiment, during which a known mass of hydrocarbon contaminant was released under natural-gradient conditions. Using the suite of solute concentrations measured in the dense three-dimensional sampling grid installed prior to the NATS contaminant release, a calibrated numerical model was developed and used to interpret results of the NATS experiment.

## References

- Lovley, D.R., F.H. Chapelle, and J.C. Woodward. 1994. Use of dissolved H<sub>2</sub> concentrations to determine distribution of microbially catalyzed redox reactions in anoxic groundwater. *Environ. Sci. Tech.* 28(7):1205-1210.
- U.S. Environmental Protection Agency. 1999. Use of monitored natural attenuation at Superfund, RCRA corrective action, and underground storage tank sites. *U.S. Environmental Protection Agency OSWER Directive 9200.4-17P*.
- Waddill, D.W. and M.A. Widdowson. 1997. SEAM3D: A numerical model for three-dimensional solute transport and sequential electron acceptor-based biodegradation in groundwater. *Documentation and User's Guide*. US Army Corps of Engineers Waterways Experiment Station, Vicksburg, MS.

## CHAPTER 2

### Literature Review

#### The Biodegradation Environment

As Wilson et al. (1986) indicate, the local microbial population, the concentration of available electron acceptor, or the concentration of the electron donor limits biodegradation in the natural environment. Microbial populations require a carbon, energy, and respiratory source to survive and grow (Bedient et al., 1994). In bioremediation, a groundwater contaminant, such as an aromatic hydrocarbon, can serve as the energy and carbon source, or substrate, and respiration is satisfied by an electron acceptor, such as oxygen, nitrate, iron(III), or sulfate. Wilson et al. (1986) also note that many aquifers support a microbial population capable of degrading various groundwater contaminants, and cite the work of Ghiorse and Balkwill (1983) as evidence that these aquifers are capable of supporting this population, even at deeper locations. Given an adequate microbial population in the presence of suitable concentrations of both a substrate and electron acceptor, contaminant oxidation (i.e. biodegradation) may occur, unless limited by the presence of one or more inhibitory substances.

#### Electron Tower Theory and Sequential Electron Acceptors

Microorganisms gain energy from the oxidation of organic matter by coupling substrate oxidation to the reduction of various electron acceptors. The electron tower theory, based on a thermodynamic analysis of free energy potential, demonstrates that some electron acceptors contain more energy potential than others. Suflita and Sewell (1991) report the electron acceptor utilization order, shown schematically as Figure 1, by examining the energy potential for each reduction process. Jørgensen (1989) uses the Gibbs free energies for the electron acceptor half reactions, calculated by Stumm and Morgan (1981), to support a similar electron acceptor sequence. Stumm and Morgan (1981) note that microbes tend to oxidize organic substrate by preferentially using the electron acceptor that provides the most energy. The results of Stumm and Morgan's work, combined with field observations by Lyngkilde et al. (1991), Lovley et al. (1994) and others, has led to the interpretation that biological activity in contaminant plumes

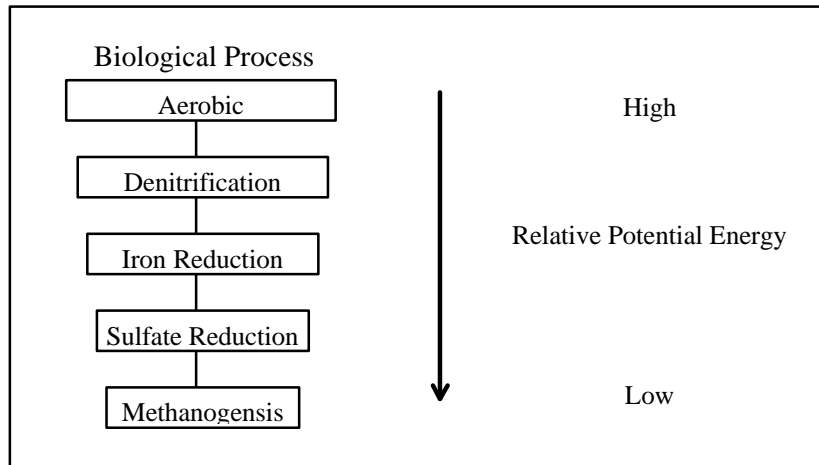


**Figure 1. Electron acceptor utilization sequence determined by electron potential energies. (After Suflita and Sewell, 1991)**

varies from a highly reactive aerobic plume boundary, through interior zones of nitrate and iron(III) reduction, to a central core where highly reduced sulfate and methanogenic conditions dominate, as shown in Figure 2. Rates of contaminant oxidation will vary within the contaminant plume based on each contaminant's susceptibility to microbial attack, the presence of a suitable microbial population, the availability and quantity of an appropriate electron acceptor, and the presence (or absence) of specific biological inhibitors. For example, the introduction of oxygen during anoxic and anaerobic degradation of petroleum hydrocarbons has been shown to inhibit further oxidation of the hydrocarbon under nitrate-, iron-, and sulfate reducing conditions (Hutchins, 1991; Chang et al., 1993; Coates et al., 1996). Similarly, Coates et al. (1996) show that iron(III)-reducing conditions may inhibit petroleum hydrocarbon oxidation by sulfate-reducers, but it is not clear whether this inhibition is due to a real disruption of the sulfate-reduction process or whether the increased reduction potential of iron(III) allows iron(III)-reducers to simply out-compete sulfate-reducers for the available substrate.

### **Petroleum Hydrocarbon Removal by Sequential Electron Acceptor Processes**

Early research into organic compound degradation recognized only the importance of oxygen-based, or aerobic, respiration. Lee et al. (1987) found that petroleum hydrocarbons, such as gasoline, aviation fuels, and heating oils, are some of the most aerobically biodegradable compounds found in the subsurface environment. Severe limits may be placed on aerobic biodegradation of petroleum hydrocarbons, however, due to the low solubility of oxygen and the

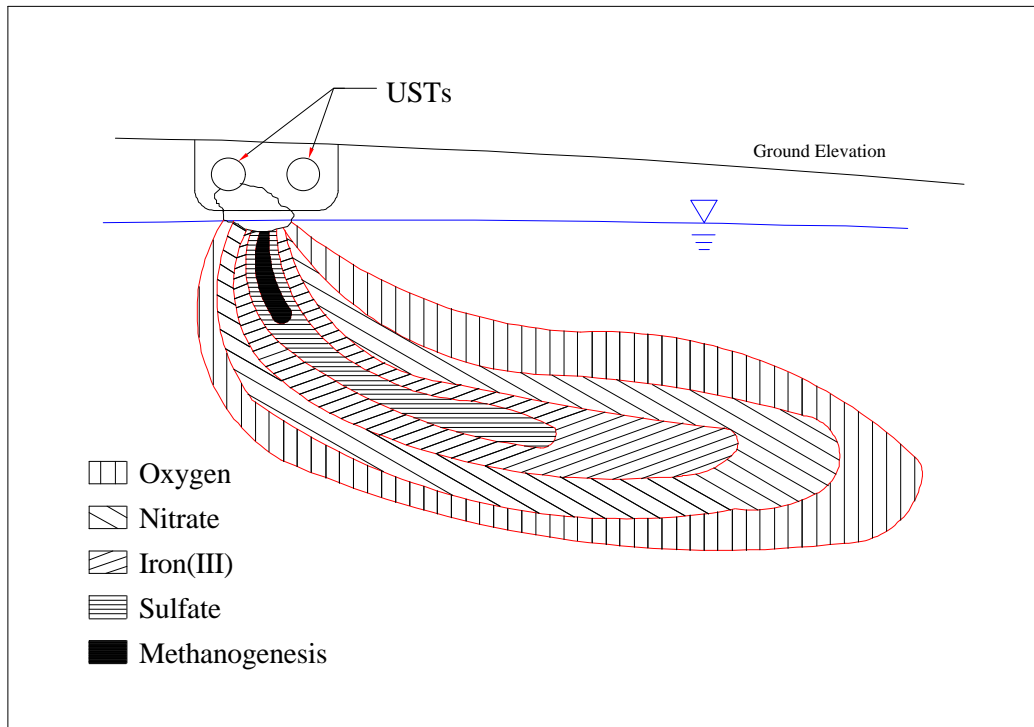


**Figure 2. Spatial variation of electron acceptor conditions for a typical groundwater contaminant plume. (Adapted from Lyngkilde et al., 1991)**

rapid reaction rates typical of oxygen reducing environments (Wilson et al., 1986; Zeyer et al. 1986; Barker et al., 1987).

More recent investigations have led researchers to recognize the significance of anaerobic degradation of aromatic hydrocarbons. Investigation of aromatic hydrocarbon oxidation using nitrate-reducing (Zeyer et al., 1986; Hutchins, 1991; Arcangeli and Arvin, 1994), iron(III)-reducing (Lovley and Lonergan, 1990; Lovley et al., 1993), sulfate-reducing (Haag et al., 1991; Edwards and Grbic-Galic, 1992) and methanogenic (Wilson and Rees, 1985; Grbic-Galic and Vogel, 1987) organisms has helped generate more interest into natural attenuation as an effective treatment strategy. According to Chapelle (1995), iron(III) and sulfate terminal electron accepting process may exhibit a rate constant two to three orders of magnitude less than aerobic conditions, but still adequately contain the contaminant plume if the groundwater velocity is slow relative to the rate of substrate biodegradation. The large degradation potential of iron(III)- and sulfate reducing processes is attributed to the greater mass of iron(III) and sulfate in the subsurface environment which allows for longer reaction times of anaerobic degradation (Wilson et al., 1986; Hutchins, 1991; Landmeyer et al., 1996). Furthermore, the biodegradation impact of

iron(III)- and sulfate-reducing microorganisms on a substrate, which is biodegradable under multiple electron acceptors (e.g. toluene), may be the difference between attaining a contaminant threshold level or not. For example, if the mass (or concentration) of oxygen and nitrate is low, the mass of contaminant consumed during anaerobic degradation may be much greater than the mass lost under aerobic or anoxic conditions, as shown in Figure 3. From this hypothetical example, the recognition of anaerobic degradation of petroleum hydrocarbons is critical to the overall success and regulatory acceptance of natural attenuation as a complete remediation strategy.

Unfortunately, not all hydrocarbons readily degrade under multiple electron acceptor conditions. Some hydrocarbons, such as benzene, appear to degrade under multiple electron acceptor conditions at some sites, while degrading solely under aerobic conditions at other sites. Other compounds, such as pyrene, have only been shown to degrade under aerobic conditions and are considered recalcitrant under both anoxic and anaerobic conditions.

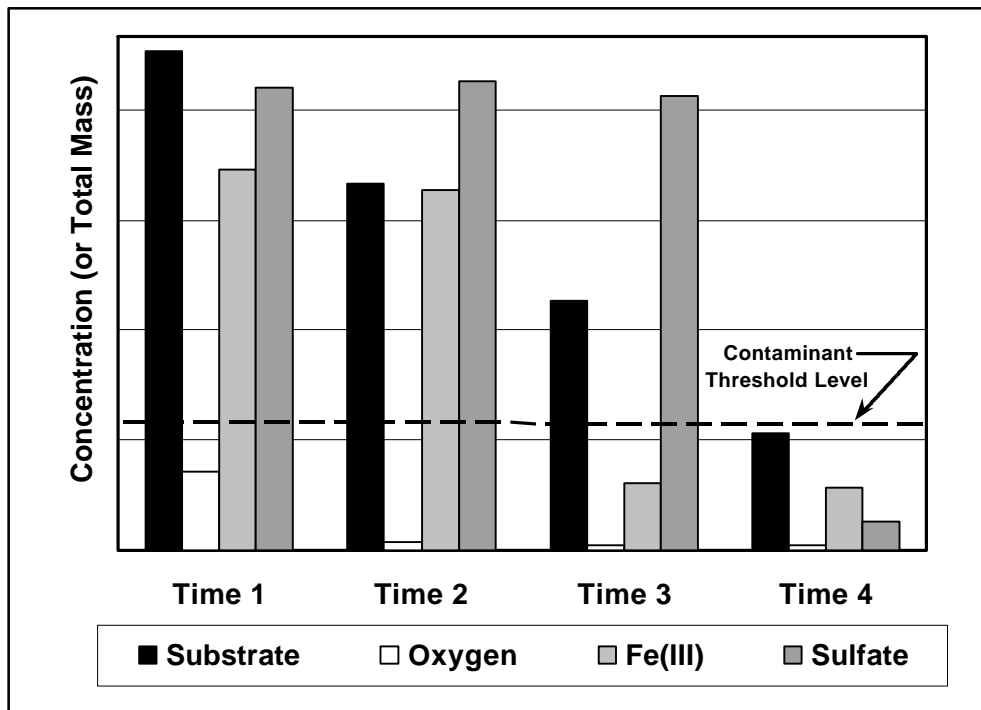


**Figure 3. Microbially mediated contaminant removal by sequential microbial (aerobic/iron(III)-reducing/sulfate-reducing) electron accepting processes.**

### Modeling Natural Attenuation of Petroleum Hydrocarbons

Given the uncertainty in determining whether a specific contaminant is degrading in a given aquifer location, regulators and other interested parties are turning to mathematical models

of natural attenuation as important interpretive and predictive tools. To accurately simulate petroleum contaminant plume migration, mathematical models of natural attenuation need to include biodegradation under multiple electron acceptor conditions. Considering that different petroleum hydrocarbons degrade at different rates and under specific reducing environments, tracking of multiple hydrocarbon substrates is also important. The concentration distribution of potential electron acceptors is also likely to vary with both space and time, and these distributions will affect migration and degradation of hydrocarbon contaminant plumes.

Limitations of computational power, mathematical model complexity, and techniques for characterization of heterogeneous aquifers necessarily confined early *in situ* biodegradation to simplified models. Early reactive solute transport models were generally limited to homogeneous flow fields which simulated either two-dimensional or quasi-three dimensional solute transport. Biodegradation kinetics in these models were also simplistic, generally using instantaneous, single electron acceptor reaction kinetics. Advances in computational power have allowed current models, such as the SEAM3D model developed by Waddill and Widdowson (1997), to use sequential, Monod-type reaction kinetics while tracking three-dimensional transport of multiple substrates, multiple electron acceptors, and multiple reaction end products.

Based on these improvements in computation ability in numerical models for biologically reactive solute transport, researchers such as Gelhar (1986) initiated investigations into how stochastically generated heterogeneous flow fields affect solute transport. MacQuarrie and Sudicky (1990) and Miralles-Wilhelm et al. (1997) use single electron acceptor (aerobic) biodegradation models of hydrocarbon fate and transport to demonstrate that increases in aquifer heterogeneity produce increases in the total mass of biodegraded hydrocarbon under simulated natural conditions. In contrast to these findings of a positive correlation between heterogeneity and hydrocarbon biodegradation under natural attenuation, Schäfer and Kinzelbach (1992) show that increasing aquifer heterogeneity decreases biodegradation effectiveness of active remediation strategies for model simulations that pump oxygen into a hypothetical hydrocarbon plume in an effort to increase biodegradation. Of greater concern is that MacQuarrie and Sudicky (1990), Schäfer and Kinzelbach (1992), and Miralles-Wilhelm et al. (1997) agree that using a homogeneous flow field and macrodispersivity (i.e.  $\alpha_L > 10$  cm) to simulate biologically reactive transport in truly heterogeneous flow fields causes numerical models to overpredict hydrocarbon biodegradation due to artificial mixing between the hydrocarbon and oxygenated water.

Published research into modeling sequential electron acceptor biodegradation in heterogeneous aquifers is limited to the work of Waddill (1998), which uses the SEAM3D model to examine the effects of aquifer heterogeneity under sequential aerobic/sulfate-reducing conditions. Waddill (1998) indicates that increasing aquifer heterogeneity increases degradation of petroleum hydrocarbons under sequential (oxygen/sulfate-reducing) electron acceptor conditions, although his work was limited to a single hydraulic conductivity realization.

## References

- Arcangeli, J.P. and E. Arvin. 1994. Biodegradation of BTEX compounds in a biofilm system under nitrate reducing conditions. In: R.E. Hinchee, B.C. Alleman, R.E. Hoepfel, and R.N. Miller, Eds., *Hydrocarbon Bioremediation*. Lewis Publishers, Boca Raton, FL. pp. 374-382.
- Barker, J.F., G.C. Patrick, and D. Major. 1987. Natural attenuation of aromatic hydrocarbons in a shallow sand aquifer. *Ground Water Monit. Rev.* 7:64-71.
- Bedient, P.B., H.S. Rifai, and C.J. Newell. 1994. *Ground Water Contamination: Transport and Remediation*. PTR Prentice-Hall, Inc., Englewood Cliffs, NJ.
- Chang, M-K, T.C. Voice, and C.S. Criddle. 1993. Kinetics of competitive inhibition and cometabolism in the biodegradation of benzene, toluene, and p-xylene by two *Pseudomonas* isolates. *Biotechnol. Bioeng.* 41(11):1057-1065.
- Chapelle, F.H. 1995. Factors affecting the efficiency of intrinsic bioremediation under anaerobic conditions. In *Platform Abstracts, In Situ and On-Site Bioreclamation, The Third Int'l Symp.*, April 24-27, 1995, San Diego, CA.
- Coates, J.D., R.T. Anderson, J.C. Woodward, E.J.P. Phillips, and D.R. Lovley. 1996. Anaerobic hydrocarbon degradation in petroleum-contaminated harbor sediments under sulfate-reducing and artificially imposed iron-reducing conditions. *Environ. Sci. Tech.* 30:2784-2789.
- Edwards, E.A. and D. Grbic-Galic, 1992. Complete mineralization of benzene by aquifer microorganisms under strictly anaerobic conditions. *Appl. Environ. Microbiol.* 58(8):2663-2666.
- Gelhar, L.W. 1986. Stochastic subsurface hydrology: From theory to applications. *Water Resour. Res.* 22(9):135S-145S.
- Ghiorse, W.C. and D.L. Balkwill. 1983. Enumeration and morphological characterization of bacteria indigenous to subsurface environments. *Dev. Ind. Microbiol.* 24:213-225.
- Grbic-Galic, D. and T.M. Vogel. 1987. Transformation of toluene and benzene by mixed methanogenic cultures. *Appl. Environ. Microbiol.* 53(2):254-260.
- Haag, F.M., M. Reinhard, and P.L. McCarty. 1991. Degradation of toluene and p-xylene in anaerobic microcosms: Evidence for sulfate as a terminal electron acceptor. *Environ. Toxicol. Chem.* 10:1379-1390.

- Hutchins, S.R. 1991. Biodegradation of monoaromatic hydrocarbons by aquifer microorganisms using oxygen, nitrate, or nitrous oxide as the terminal electron acceptor. *Appl. Environ. Microbiol.* 57(8):2403-2407.
- Jørgensen, B.B. 1989. Biochemistry of Chemoautotrophic Bacteria. In H.G. Schlegel and B. Bowien, eds., *Autotrophic Bacteria*. Science Tech Publishers, Madison, WI. pp. 117-146
- Landmeyer, J.E, F.H. Chapelle, and P.M. Bradley. 1996. Assessment of intrinsic bioremediation of gasoline contamination in the shallow aquifer, Laurel Bay Exchange, Marine Corps Air Station, Beaufort, South Carolina. *USGS Water-Resources Investigations Report 96-4026*.
- Lee, M.D., V.W. Jamison, and R.L. Raymond. 1987. Applicability of in situ bioreclamation as a remedial action alternative. In *Proceed. of the Petroleum Hydrocarbons and Organic Chemicals in Ground Water: Prevention, Detection, and Restoration*. Houston, TX, National Water Well Association, Dublin, OH, pp. 167-185.
- Lovley, D.R., F.H. Chapelle, and J.C. Woodward. 1994. Use of dissolved H<sub>2</sub> concentrations to determine distribution of microbially catalyzed redox reactions in anoxic groundwater. *Environ. Sci. Tech.* 28(7):1205-1210.
- Lovley, D.R., S.J. Giovannoni, D.C. White, J.E. Champine, E.J.P. Phillips, Y.A. Gorby, and S. Goodwin. 1993. *Geobacter metallireducens*, new genus species, a microorganism capable of coupling the complete oxidation of organic compounds to the reduction of iron and other metals. *Archive Microbiol.* 159(4):336-344.
- Lovley, D.R. and D.J. Lonergan. 1990. Anaerobic oxidation of toluene, phenol, and *p*-cresol by the dissimilatory iron-reducing organism, GS-15. *Appl. Environ. Microbiol.* 56(6):1858-1864.
- Lyngkilde, J., T.H. Christensen, B. Skov, and A. Foverskov. 1991. Redox zones down gradient of a landfill and implications for biodegradation of organic compounds. In R.E. Hinchee and R.F. Olfenbittel, eds., *In Situ Bioreclamation: Applications for Hydrocarbon and Contaminated Site Remediation*. Butterworth-Heinemann, Boston. pp. 363-376.
- MacQuarrie, K.T.B. and E.A. Sudicky. 1990. Simulation of biodegradable organic contaminants in groundwater: 2. Plume behavior in uniform and random flow fields. *Water Resour. Res.* 26(2):223-239.
- Miralles-Wilhelm, F., L. Gelhar, and V. Kapoor. 1997. Stochastic analysis of oxygen-limited biodegradation in three-dimensionally heterogeneous aquifers. *Water Resour. Res.* 24(4):615-619.
- McFarland, M.J. and R.C. Sims. 1991. Thermodynamic framework for evaluating PAH degradation in the subsurface. *Ground Water.* 29(6):885-896.
- Schäfer, W. and W. Kinzelbach. 1992. Stochastic modeling of in situ bioremediation in heterogeneous aquifers. *J. Contam. Hydrol.* 10:47-73.
- Stumm, W. and J.J. Morgan. 1981. *Aquatic Chemistry*. J. Wiley & Sons, New York. Chapter 7.
- Suflita, J.M. and G.W. Sewell. 1991. Anaerobic biotransformation of contaminants in the subsurface. EPA/600/90/024, Robert S. Kerr Research Laboratory, Ada, OK.

- Waddill, D.W. 1998. Three-dimensional modeling of solute transport with in situ bioremediation based on sequential electron acceptors. *Ph.D. Dissertation submitted to the Faculty of VPI&SU*, Blacksburg, VA
- Waddill, D.W. and M.A. Widdowson. 1997. SEAM3D: A numerical model for three-dimensional solute transport and sequential electron acceptor-based bioremediation in groundwater. *Tech. Report submitted to the U.S. Army Corps of Engineers, Waterways Experiment Station*, Vicksburg, MS.
- Wilson, J.T., L.E. Leach, M. Henson, and J.N. Jones. 1986. In situ bioremediation as a ground water remediation technique. *Ground Water Monit. Rev.* 6:56-64
- Wilson, B.H. and J.F. Rees. 1985. Biotransformation of gasoline hydrocarbons in methanogenic aquifer material. *Proceedings of the NWWA/API Conference on Petroleum Hydrocarbons and Organic Chemicals in Ground Water*. November 13-15, 1985, Houston, TX, National Water Well Association, Dublin, OH.
- Zeyer, J., E.P. Kuhn, and R.P. Schwarzenbach. 1986. Rapid microbial mineralization of toluene and 1,3-dimethylbenzene in the absence of molecular oxygen. *Appl. Environ. Microbiol.* 52(4):944-947

## CHAPTER 3

### Biodegradation of Selected Polycyclic Aromatic Hydrocarbons by Native Microbial Populations under Simulated Natural Conditions

J. STEVEN BRAUNER, MARK A. WIDDOWSON, JOHN T. NOVAK, AND NANCY G. LOVE

*200 Patton Hall, Department of Civil and Environmental Engineering  
Virginia Polytechnic Institute and State University  
Blacksburg, VA 24061-0105*

#### ABSTRACT

A laboratory microcosm study was initiated to estimate site-specific biodegradation rates for five polycyclic aromatic hydrocarbon compounds (PAHs) under simulated intrinsic conditions. This work was part of a natural attenuation assessment at a No. 2 fuel oil-contaminated site in the Atlantic Coastal Plain of Virginia. First-order biodegradation rates for acenaphthene, fluorene, phenanthrene, pyrene, and benzo(b)fluoranthene were calculated as 1.57 year<sup>-1</sup>, 1.45 year<sup>-1</sup>, 1.13 year<sup>-1</sup>, 1.58 year<sup>-1</sup>, and 1.65 year<sup>-1</sup>, respectively, prior to cessation due to electron acceptor limitation. No observable lag period was noted. Stoichiometric mass balance calculations suggest that the majority of PAH mass loss (38-53%) was due to aerobic biodegradation, although sulfate-reduction also accounted for a measurable portion of PAH mass loss (~9%). During a previous microcosm study at this site using an identical methodology but a soil sample from a less contaminated location, first-order biodegradation rates for fluorene, phenanthrene, and pyrene were reported as 2.41 year<sup>-1</sup>, 3.28 year<sup>-1</sup>, and 2.98 year<sup>-1</sup> after an approximately 75 day acclimation period. Acenaphthene and benzo(b)fluoranthene biodegradation was not observed in microcosms containing soil from the less contaminated site. Results indicate that both the acclimation period and biodegradation rate for specific PAH compounds will vary with location at this site.

#### Introduction

Regulatory acceptance of monitored natural attenuation (MNA) at petroleum hydrocarbon sites is dependent on site-specific data that show attenuation of specific contaminants which are of health and environmental concern. One line of evidence for

determining whether MNA may be considered as part of a remediation plan for a specific site is to perform microcosm experiments using soil samples collected from that site to demonstrate contaminant biodegradation under simulated natural conditions (1). As part of a MNA remediation plan, an estimate of the time to contaminant removal is also required. Biodegradation rates obtained from microcosm studies are useful for estimating the time to removal for individual compounds under either enhanced or natural conditions.

Although biodegradation has been demonstrated for most PAH compounds under at least one electron acceptor condition, the extent of PAH biodegradation by native microbial consortia under intrinsic conditions is not fully known when these compounds are found as either a sole or mixed substrate. The term “intrinsic conditions” is intended to refer to field conditions or laboratory experiments in which biostimulation (i.e. addition of electron acceptors, nutrients, and cometabolites) and/or bioaugmentation (i.e. addition of specific cultures of microorganisms) was not employed to stimulate PAH biodegradation. Research has demonstrated PAH biodegradation under aerobic conditions when an appropriate mixture of microorganisms, nutrients, and oxygen were present (e.g. 2-4). Biotransformation of acenaphthene, acenaphthylene, anthracene, fluorene, naphthalene, and phenanthrene, and pyrene under strictly anaerobic, nitrate-reducing conditions has also been shown to occur (4-7). Two recent studies were the first to demonstrate PAH biodegradation under sulfate-reducing conditions, as a native microbial population collected with marine sediments was shown to biodegrade fluorene, fluoranthene, phenanthrene, and naphthalene (8,9). Variation in microbial population size and ability to biodegrade specific PAHs has also been observed to vary by location in a native fresh-water population at a former manufactured gas plant site (10).

The goal of the present study was to establish whether a native, non-specific microbial consortia, collected with a deep soil sample from a contaminated location at a No. 2 fuel oil contaminated site, was able to biologically transform a mixture of five PAH compounds under simulated intrinsic conditions. The PAHs investigated in this study (acenaphthene, benzo(b)fluoranthene, fluorene, phenanthrene, and pyrene) were selected based on a previous site investigation (11) that found each of these compounds in measurable quantities at various locations of the site. Biodegradation rates for PAHs were estimated based on the difference in mass loss rates between live and autoclaved control microcosms that were prepared under aerobic conditions. Using measurements of observed electron acceptor consumption, the

theoretical mass of biodegraded PAH was calculated to determine if one microbial process was dominant in the live microcosms. Two stoichiometric methods for calculating the theoretical hydrocarbon mass loss were applied and compared. PAH biodegradation rates observed in microcosms containing the deep soil were compared with results from a previous study (12) at a less contaminated location of the site. Based on results from the microcosm experiments, implications for applying natural attenuation to this site are discussed.

## Experimental Section

**Site selection and soil collection.** Soil samples were collected from the Atlantic Coastal Plain in northern Virginia, in an area where No. 2 fuel oil had leaked from a large number of underground storage tanks (USTs) serving residential housing. Samples were collected aseptically, placed in sterilized jars, transported to the laboratory, and stored at 20 °C until used in the microcosm experiment. The soil used in the present study (hereafter referred to as Site A) was collected from well cuttings brought to the surface during the installation of a monitoring well into an area previously shown as highly-contaminated with fuel oil. Analysis by gas chromatography using mass spectrometry (GC-MS) indicated that this soil sample contained relatively low concentrations of CH<sub>2</sub>Cl<sub>2</sub> extractable hydrocarbons, although a strong petroleum smell exuded from the sample. An identical analytical procedure was applied to a near land surface soil collected as part of a previous study (12) that will be discussed in the results section. GC-MS analysis of this second sample (hereafter referred to as Site B) indicated that this soil was contaminated with a series of alkane hydrocarbons, but there was no evidence of previous exposure to PAHs.

**Microcosm construction.** Microcosm samples were prepared under aerobic conditions in sterilized, 10 mL, threaded test tubes and sealed with Teflon<sup>®</sup>-lined caps. Acenaphthene, fluorene, phenanthrene, pyrene, and benzo(b)fluoranthene were dissolved in hexane and added to a portion (approximately 40 percent, by weight) of each soil sample. Prior to contacting the soil with the PAH/hexane mixture, soil particles that were larger than a few millimeters in diameter were broken into smaller pieces using a mortar and pestle to promote a more homogenous PAH distribution. After thorough mixing, the solvent (hexane) was allowed to evaporate from the sample. The freshly PAH-contaminated soil was combined with the remaining portion of soil (which had not been contacted with hexane to preserve the native microbiota) and well mixed. A

small portion (~ 5g) of mixed soil was added to each microcosm along with 5 mL of deionized, autoclaved water. An identical set of abiotic ‘control’ microcosms was created for each soil by repeatedly autoclaving (10 repetitions of 25-minute duration at 121°C and 15 psi) the soil prior to addition of the hexane/PAH mixture. Other than providing a fresh source of PAHs and oxygen (in the deionized water), no other chemical or biological amendments were added to the microcosms. The microcosms were incubated in the dark at 12 °C until destructively sacrificed in triplicate.

**Analytical Methods.** PAH compounds were extracted from each microcosm by combining the microcosm contents with 15 mL CH<sub>2</sub>Cl<sub>2</sub> in 40 mL amber vials. The 40 mL vials were sealed with screw-on caps containing Teflon coated septa and rotated for 24 hours to promote thorough contact between the microcosm contents and CH<sub>2</sub>Cl<sub>2</sub>. After rotation, the contents of the 40 mL vials were allowed to settle and were stored in the dark at 4°C for a minimum of 4 and maximum of 24 hours prior to analysis by a gas chromatograph using a flame ionization detector (GC-FID). Extractable PAHs were measured in duplicate by injecting a 2 µL sample into the GC-FID. PAH concentrations (mg PAH per liter CH<sub>2</sub>Cl<sub>2</sub>) were quantified using a series of external standards, and converted to mass of PAH per mass of soil by considering the volume of solvent (15 mL) and initial mass of soil (5 g) in each microcosm vial.

Oxygen concentrations were measured using a dissolved oxygen (DO) probe. A two point calibration procedure was performed by successively bubbling nitrogen gas (0% oxygen) and breathing air (21% oxygen) through a calibration cell. Electrode calibration was monitored and adjusted (when needed) before and after each set of measurements to account for the effects of drift inherent to the electrode. Nitrate and sulfate concentrations were measured concurrently by removing approximately 1.5 mL of water from the microcosms (prior to CH<sub>2</sub>Cl<sub>2</sub> extraction) and analyzing the sample using ion chromatography (IC). Prior to injection into the ion chromatograph, the sample was filtered using an IC syringe filter (0.45 µm pore size, polyethersulfone, and hydrophilic, bi-directional membrane). External standards were used to calculate nitrate and sulfate concentrations.

**Degradation Rate Estimation.** Degradation rates were calculated using a linear regression on log transformed PAH concentrations, yielding first-order exponential rate constants. PAH degradation rates in the control microcosms were calculated using all available data points. PAH degradation rates in the live microcosms from Site A were calculated for two

distinct periods. The first period, which consisted of the first nine data points, corresponded to the time when oxygen and sulfate were present in the microcosm. The second period of PAH measurements consisted of data points ten through thirteen, which were collected after DO was measured below the detection limit of 0.1 mg/L. R-squared values for Site A controls varied over a wider range (0.43 to 0.88) than values for the Site A live samples during the initial degradation period (0.75 to 0.90). Statistical comparison of degradation rates in the live and control microcosms was accomplished using a method similar to that developed in a previous microcosm study on slowly degrading chlorinated compounds (13). The degradation rate in the live microcosms was considered statistically greater than the rate in the control microcosms when the 95 percent confidence interval of the degradation rate in the live microcosms did not include the degradation rate of the controls.

**Stoichiometric Mass Balance Procedure.** Stoichiometric mass balance equations were developed to estimate the mass of PAH that could theoretically be oxidized to carbon dioxide for observed changes in electron acceptor mass. Because the five PAHs added during microcosm construction served as a mixed substrate, calculations for the theoretical PAH mass loss could only be estimated as the total for all five PAHs. A theoretical estimate for the total PAH mass mineralized under electron accepting condition  $n$  ( $\Delta\text{PAH}_n^{\text{theoretical}}$ ) was estimated using

$$\Delta\text{PAH}_n^{\text{theoretical}} = \frac{\Delta\text{EA}_n^{\text{observed}}}{\bar{\gamma}_n} \quad (1)$$

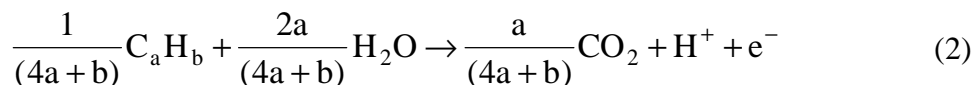
where  $\Delta\text{EA}_n^{\text{observed}}$  was the observed mass of electron acceptor  $n$  consumed and  $\bar{\gamma}_n$  was the mean electron acceptor use coefficient for the mass of electron acceptor  $n$  reduced per mass of PAH mineralized [ $M_{\text{EA}}/M_{\text{PAH}}$ ]. The aqueous phase  $\Delta\text{EA}_n^{\text{observed}}$  was estimated by subtracting the difference between the electron acceptor concentration measured in the live microcosms at the end of the experiment from the concentrations measured in the controls, and multiplying this concentration differential by the volume of water in the microcosm (5 mL). For oxygen, the gaseous phase  $\Delta\text{EA}_n^{\text{observed}}$  was calculated by assuming that 21 percent of the air in the 2.5 mL headspace was oxygen, and added to the aqueous phase component. The mass of oxygen in the headspace was included in the total mass of consumed oxygen because gaseous oxygen was

assumed to readily diffuse from the headspace into the aqueous phase to replenish aqueous phase oxygen consumed during biodegradation.

For the five PAH substrate mixture used in this experiment,  $\bar{\gamma}_n$  was estimated as

$$\bar{\gamma}_n = \frac{1}{M} \sum_{m=1}^{M=5} \gamma_{m,n} \quad (1)$$

where  $\gamma_{m,n}$  was the use coefficient for mineralization of PAH  $m$  under electron acceptor condition  $n$ . Each electron acceptor use coefficient was calculated based on PAH and electron acceptor molecular weights and the molar ratio of PAH to electron acceptor estimated from stoichiometrically balanced equations, which were developed using half cell reactions for PAH mineralization and electron acceptor reduction. The least complex stoichiometric formulation assumes that the PAHs were the sole electron donors, carbon dioxide and water were the only products, and none of the hydrocarbon was converted to biomass (i.e. zero yield). Half cell reactions for phenanthrene and pyrene mineralization (14) and electron acceptor reduction (15) have been previously developed, whereas half cell reactions for acenaphthene, fluorene, and benzo(b)fluoranthene mineralization were developed in this study using the general electron donor half cell reaction given by



and described in (16). The constants  $a$  and  $b$  in Equation 2 represent the number of carbon and hydrogen atoms, respectively, in the original hydrocarbon compound. Table 1 contains the stoichiometric equations for the zero yield case for all five PAHs under aerobic and sulfate-reducing conditions. Table 2 contains electron acceptor use coefficients for each PAH under aerobic and sulfate-reducing conditions for the zero yield case, which were calculated using the stoichiometric ratios from Table 1. As shown in Table 1,  $\bar{\gamma}_n$  was therefore estimated as 2.96 mg- $O_2$ /mg $_{PAH}$  and 4.45 mg $_{SO_4}$ /mg $_{PAH}$  for aerobic and sulfate-reducing conditions, respectively, when yield was not included in the stoichiometric equations.

Because the stoichiometric calculations in Table 1 neglect biomass yield, the values for  $\bar{\gamma}_n$  presented in Table 2 will result in an underestimation the theoretical mass of PAH mineralized for a given mass of electron acceptor consumed. Previous work, which assumed that

a portion of the hydrocarbon is converted to biomass, demonstrated that one method of accounting for microbial growth in stoichiometric formulations was to treat biomass production as a reaction endproduct given by the empirical formula  $C_5H_7O_2N$  (17). This method also incorporated a biomass yield coefficient (Y) to account for the efficiency of biomass production on a given substrate. Theoretical estimates for the average biomass yield during PAH oxidation under aerobic and sulfate-reducing conditions have been reported as  $0.33 \text{ g}_{biomass}/\text{g}_{PAH}$  and  $0.06 \text{ g}_{biomass}/\text{g}_{PAH}$ , respectively (14), using a bioenergetic model that assumed ammonium was a non-limiting source of nitrogen (18). Based on these theoretical estimates for the yield coefficients, stoichiometric equations that include biomass yield were developed for PAH oxidation to  $CO_2$  under aerobic and sulfate-reducing conditions, and are presented in Table 3. The corresponding use coefficients for each PAH are presented in Table 4, with values for  $\bar{\gamma}_n$  estimated as  $1.98 \text{ mg}_{O_2}/\text{mg}_{PAH}$  and  $4.18 \text{ mg}_{SO_4}/\text{mg}_{PAH}$  for aerobic and sulfate-reducing conditions, respectively, when yield was included in the stoichiometric equations.

## Results and Discussion

**PAH Degradation and Electron Acceptor Disappearance.** Results for PAH concentration versus time are reported in Figure 1 for each of the five PAH compounds measured in the Site A live and control microcosms. Each data point represents the average concentration of three sacrificially sampled microcosms, with error bars representing  $\pm$  one standard deviation. The starting concentrations of the five PAHs ranged between 15 and  $100 \text{ mg}_{PAH}/\text{kg}_{soil}$  and were consistent with the range of maximum PAH concentrations measured at the site. The slopes of the best fit lines through the first nine data points in the Site A live microcosms and all of the data points in the Site A control microcosms are reported in Table 5 as the live and control degradation rates, respectively, for each PAH. During the first three and a half months of the experiment, PAH mass loss rates in the Site A live microcosms ranged from  $1.65 \text{ year}^{-1}$  to  $2.23 \text{ year}^{-1}$  and were greater than the rates observed for the Site A controls, which ranged from  $0.36$  to  $1.06 \text{ year}^{-1}$ . Statistical regression ( $p \leq 0.05$ ) of Site A degradation rates, calculated using log-transformed data, showed that rates of removal were statistically greater in the live microcosms than in the control microcosms for all five PAHs. At approximately 112 days into the experiment, mass loss rates in the Site A live microcosms (computed from the last

four data points) were statistically similar to mass loss rates in the control microcosms for all five PAHs.

Dissolved oxygen concentrations recorded 112 days into the experiment were below detection (less than 0.1 mg/L) in the Site A live microcosms, indicating that the available oxygen had been consumed. Sulfate concentrations in the live microcosms were measured as 1.2 ( $\pm 0.9$ ) mg/L at day 218. In comparison, dissolved oxygen and sulfate concentrations in the Site A control microcosms were measured as 5 ( $\pm 1.8$ ) mg/L and 53 ( $\pm 2.3$ ) mg/L, respectively, at day 218. Measured concentrations of nitrate, another potential electron acceptor, were less than 1 mg/L for all samples tested (both live and control microcosms), suggesting that little or no PAH oxidation occurred due to nitrate-reduction. Addition of sulfate to the microcosms 314 days into the experiment did not produce additional PAH or sulfate consumption.

PAH mass losses in the control microcosms were believed to reflect irreversible abiotic processes produced by a combination of micropore diffusion and oxidative coupling. Several studies have shown that long contact times between PAHs and soil may result in a decrease in extractable hydrocarbon mass with time (19,20). These researchers attributed this phenomenon to diffusion of hydrophobic compounds into soil micropores when contact times were on the order of several days to several months. The solvent extraction procedure used in this study measured the combined mass of aqueous and 'reversibly' sorbed PAH per dry soil mass, as the portion of PAH mass located in the soil micropores (i.e. irreversibly sorbed PAH) was not likely to come into contact with  $\text{CH}_2\text{Cl}_2$ . Additional research has suggested that oxidative coupling can irreversibly bind PAH compounds and their intermediates to soil (21), further contributing to abiotic losses during microcosm studies.

Based on the statistically greater loss rates calculated for the Site A live microcosms, relative to the Site A control microcosms, it was evident that biodegradation was responsible for a portion of PAH mass loss in the Site A live microcosms. The observed depletion of oxygen and sulfate as terminal electron acceptors coincided with PAH disappearance in the live microcosms, suggesting that aerobic and sulfate-reducing microorganisms were active during PAH biodegradation in the Site A microcosms. It is not known whether all PAH compounds were biodegraded as a result of solely these two terminal electron accepting processes. PAH biodegradation in the Site A microcosms was believed to have ceased around Day 112 due to electron acceptor limitation, as indicated by (1) a decrease in the PAH mass loss rates in the live

microcosms (2) the similarity in the degradation rates in the live and control microcosms after Day 112, and (3) the observed consumption of oxygen and sulfate. Biodegradation rates for the live Site A microcosms (last column of Table 5) were calculated as the difference in mass loss rates between the live and control samples for each PAH compound, and represent the average PAH biodegradation rate for each PAH under all active electron acceptor conditions.

**Mass Balance Analysis.** The total observed PAH mass loss in the Site A live microcosms was calculated by summing up the observed losses of each individual PAH. Based on the first order degradation rates listed in Table 5, the total PAH mass loss in the Site A live microcosms was calculated as 0.64 mg. The abiotic portion of this mass loss was calculated as 0.21 mg using the mass loss rates from the control microcosms (Table 5, Column 5). Biodegradation was assumed to have removed the remaining 0.43 mg, representing roughly 67 percent of the total hydrocarbon lost.

The total theoretical PAH mass loss was estimated using the mass of electron acceptor consumed in the Site A microcosms, and was calculated for both stoichiometric formulations (i.e. with and without growth). PAH mass loss calculations were performed assuming that oxygen and sulfate were the only available electron acceptors, as these electron acceptors were the only two observed to decline between the Site A control and live microcosms. The observed mass of oxygen and sulfate consumed in the Site A live microcosms was 0.65 mg and 0.27 mg, respectively. Using the stoichiometric relationships for the no-growth model (Table 1) the theoretical mass of PAH loss due to aerobic biodegradation in the Site A microcosms was calculated as 0.24 mg or 38 percent of the total hydrocarbon lost. Theoretical calculations for sulfate-based PAH mass loss in the Site A indicated that approximately 0.06 mg (9 percent) of the PAH mass loss was consumed due to sulfate-reduction. As indicated in Table 6, adding the theoretical PAH mass loss under aerobic and sulfate-reducing conditions with the abiotic losses left approximately 20 percent of the observed mass loss unaccounted for when using the zero yield stoichiometric calculations. Although other microbial processes may have been active in the live microcosms, there were no visual indications of iron-reduction during the experiment.

Theoretical mass balance calculations were also made for the stoichiometric relationships listed in Table 3, which assume that a portion of the PAH degraded was converted into biomass. The small yield coefficient for sulfate had a negligible effect on the total PAH predicted to biodegrade. The mass of PAH theoretically biodegraded under aerobic conditions, however,

increased to 0.31 mg, or 53 percent of the total observed PAH loss in the Site A live microcosms. As indicated in Table 6, inclusion of yield in the theoretical PAH mass loss calculations reduced the discrepancy between the theoretical and observed estimates for PAH mass loss to less than 5 percent of the total mass loss.

Although the agreement between the theoretical and observed PAH mass loss is improved when PAH mass loss under sulfate-reducing conditions was included, no distinguishable change in the degradation rate in the Site A live microcosms was noted, as may be expected if biodegradation conditions shifted sequentially from aerobic to sulfate-reduction. The microcosm vials were not agitated during the experiment and it is probable that sulfate-reduction may have been active in the portion of the microcosm which was furthest from the headspace, even though oxygen was still detectable in the headspace. Prior to oxygen depletion in the headspace, oxygen measurements collected just below the water/soil interface were consistently lower (by > 50%) than concentrations measured in the water above the soil (unpublished data), but it is unknown whether the presence of the soil interfered with oxygen data collection using the needle probe.

The discrepancy between the theoretical estimate and observed PAH mass loss may have been caused by incomplete hydrocarbon mineralization, which would reduce the electron acceptor demand per mass of PAH observed to disappear. Accumulation of PAH intermediates was not detected during GC-FID analysis of the CHCl<sub>2</sub> extractable hydrocarbons, implying that PAH oxidation was complete or that the PAH intermediates were irreversibly bound to the soil by oxidative coupling.

**Variability in PAH Degradation with Location.** The results from this study were different in three ways from results from a previous microcosm study (12) conducted using an identical experimental method and a soil sample from a different location of this same site (Site B). First, a lag period of approximately two months was noted prior to biodegradation in the Site B microcosms (shown in Figure 2), whereas no lag period was observed in PAH degradation in the Site A live microcosms (Figure 1). This variation in lag period between the present and previous studies was attributed to different contaminant exposure histories of the soil and its impact on the microbial consortium. Biodegradation of a new substrate by non-specific microbial consortia often requires time for metabolic adaptation prior to the substrate removal. During a previous microcosm study of PAH biodegradation, a lag period was observed prior to the onset

of biodegradation when a mixture of anthracene, phenanthrene, and pyrene was introduced as the sole substrate for a pseudomonad strain that had been cultured from an uncontaminated soil (7). In the same study, PAH biodegradation was observed to begin without a detectable lag period in two separate experiments where the microcosms were inoculated with pseudomonad strains that were cultured from PAH-contaminated soils. Considering that the Site A soil sample was collected from a known area of PAH contamination, it is reasonable to assume that the microbial population collected with this soil was acclimated to PAHs, and that no time was required for microbial adaptation to PAH degradation. In contrast, GC-MS analysis of the Site B soil indicated that exposure of the microbial population in this sample may have been limited to petroleum hydrocarbons that were more volatile and soluble than the 3-, 4- and 5- ring PAHs (12). The time period observed prior to PAH degradation in the Site B live microcosms of Figure 2 may therefore represent the time required for the microbial population in an ‘unacclimated’ sample to adapt to PAH degradation.

A second difference between the two studies was an observed variation in the biodegradation capability. In live microcosm containing the Site A soil, all five PAH compounds were observed to biodegrade, whereas only fluorene, phenanthrene, and pyrene were observed to biodegrade in the live microcosms containing soil from Site B. The lack of previous exposure to a range of PAHs may explain why microbes in the Site B soil were not observed to degrade acenaphthene and benzo(b)fluoranthene. During microcosm studies of PAH biodegradation by other researchers, acenaphthalene was observed to resist biodegradation in soil samples which biodegraded multiple other PAHs (22). The agreement between these studies may suggest that the structure of acenaphthalene makes this compound less susceptible to biodegradation than other PAHs, although the observed biodegradation of acenaphthene in the acclimated Site A microcosms indicates that this compound is not completely recalcitrant.

A third difference between these studies was in the rate of PAH biodegradation. Table 6 presents first-order PAH biodegradation rates for the two samples, indicating that the biodegradation rates in the live Site A microcosms were consistently less than the degradation rates observed in the live Site B microcosms. Biodegradation rates for Site B microcosms were greater than biodegradation rates found for the Site A by a factor varying from 1.7 to 2.9 and may be the result of either the presence of excess hydrocarbons, a difference in the amount of catabolically-capable biomass, and/or a difference in microbial physiological state. Another

contributing factor may be that the microorganisms in the unacclimated sample were at a physiological state capable of supporting faster PAH metabolism than the microbes in the acclimated sample. Variation in physiological state has previously been shown to influence the biodegradation rate of a single substrate in the presence of a compound-specific microbial population poised at different growth levels (23).

Results of this study demonstrate that a native microbial consortium was capable of biodegrading a mixture of five PAH compounds under simulated intrinsic conditions. Comparison of results from this study with those from a different location at the site indicate that both the biodegradation rate and the ability of the native microbial population to biodegrade specific PAHs is likely to vary with location. Three compounds (fluorene, phenanthrene, and pyrene) were observed to biodegrade at two different locations of this site, providing one line of evidence that MNA is a potential remediation option for these PAHs. Two other PAHs (acenaphthene and benzo(b)fluoranthene) were observed to biodegrade during the present study, but neither of these PAHs was shown to biodegrade during a microcosm study using soil collected from a different location (12). More investigation is required for these two compounds, through either additional laboratory microcosm studies or the initiation of a field microcosm study, to determine whether MNA is an appropriate treatment technology for acenaphthene or benzo(b)fluoranthene. Theoretical estimates for the mass of PAH biodegraded during this experiment, based on the mass of electron acceptor consumed, were closer to the observed total PAH mass loss when theoretical yield coefficients were included in stoichiometric formulations. This result indicates that including PAH conversion to biomass in stoichiometric equations of PAH oxidation may improve future estimates of PAH mass loss for a given mass of electron acceptor.

## **Acknowledgments**

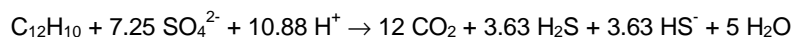
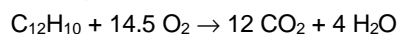
Partial funding for this research was received from the Via Foundation of the Charles E. Via, Jr. Department of Civil and Environmental Engineering at Virginia Polytechnic Institute and State University. The authors also appreciate the assistance and advice of Marilyn Grender and Julie Petruska during the experimental portion of this work.

---

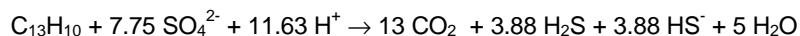
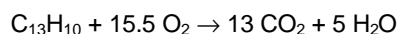
TABLE 1

Oxidation-Reduction Reactions for PAH Mineralization to Carbon Dioxide under Aerobic and Sulfate-reducing Conditions, Assuming Zero Biomass Yield. (Modified from (14).)

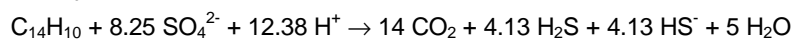
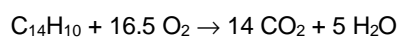
**Acenaphthene**



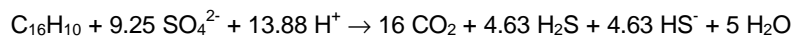
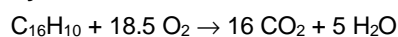
**Fluorene**



**Phenanthrene**



**Pyrene**



**Benzo(b)fluoranthene**

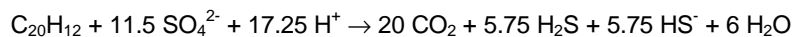
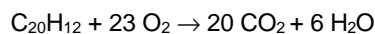


TABLE 2  
 Electron Acceptor Use Coefficients by PAH and Electron  
 Acceptor Condition for Stoichiometric Calculations  
 Assuming Zero Biomass Yield.

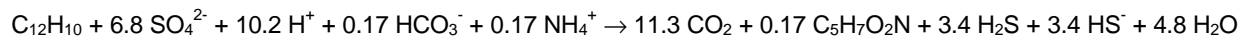
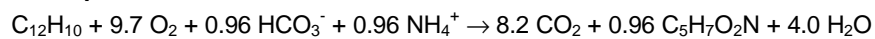
compound	Use Coefficient, $\gamma_{m,n}$	
	aerobic [mg <sub>O2</sub> /mg <sub>PAH</sub> ]	sulfate-reducing [mg <sub>O2</sub> /mg <sub>PAH</sub> ]
Acenaphthene	3.01	4.52
Fluorene	2.98	4.48
Phenanthrene	2.96	4.45
Pyrene	2.93	4.39
Benzo(b)fluoranthene	2.92	4.39
<b>Average (<math>\bar{\gamma}_n</math>) =</b>	<b>2.96</b>	<b>4.45</b>

---

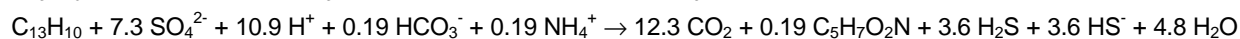
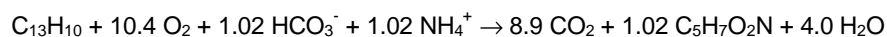
TABLE 3

Oxidation-reduction Reactions for PAH Mineralization to CO<sub>2</sub> Under Aerobic and Sulfate-reducing Conditions, Assuming Biomass Growth Using a Non-limiting Mass of Reduced Nitrogen. Yield Coefficients (mg<sub>biomass</sub>/mg<sub>PAH</sub>) for the Aerobic and Sulfate-reducing Microbial Populations Were 0.33 and 0.06, Respectively.

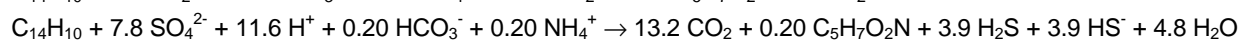
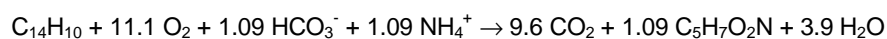
**Acenaphthene**



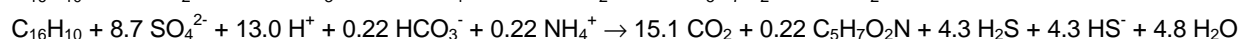
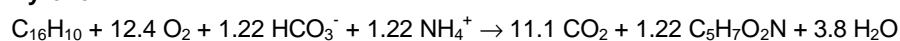
**Fluorene**



**Phenanthrene**



**Pyrene**



**Benzo(b)fluoranthene**

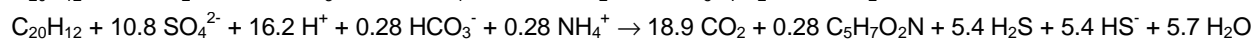
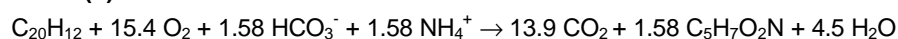


TABLE 4  
 Electron Acceptor Use for Stoichiometric Calculations when  
 Yield Coefficients ( $\text{mg}_{\text{biomass}}/\text{mg}_{\text{PAH}}$ ) of 0.33 and 0.06 were used  
 for the Aerobic and Sulfate-reducing Microbial Populations,  
 Respectively.

compound	Use Coefficient, $\gamma_{m,n}$	
	aerobic [ $\text{mg}_{\text{O}_2}/\text{mg}_{\text{PAH}}$ ]	sulfate-reducing [ $\text{mg}_{\text{O}_2}/\text{mg}_{\text{PAH}}$ ]
Acenaphthene	2.02	4.25
Fluorene	2.00	4.21
Phenanthrene	1.98	4.18
Pyrene	1.96	4.13
Benzo(b)fluoranthene	1.96	4.12
<b>Average (<math>\bar{\gamma}_n</math>) =</b>	<b>1.98</b>	<b>4.18</b>

TABLE 5

First-order Rate Constants, Confidence Intervals, and R-Squared Coefficients for Disappearance of Selected PAH Compounds in Microcosms Containing Soil from Site A.

compound	<u>Live Microcosms</u>			<u>Control Microcosms</u>			<u>Net Degradation Rate</u>
	average rate [year <sup>-1</sup> ]	(± 95% C.I.) [year <sup>-1</sup> ]	R <sup>2</sup>	average rate [year <sup>-1</sup> ]	(± 95% C.I.) [year <sup>-1</sup> ]	R <sup>2</sup>	[year <sup>-1</sup> ]
Acenaphthene	-2.20	(±1.20)	0.87	-0.63	(±1.06)	0.55	-1.57
Fluorene	-1.91	(±0.60)	0.89	-0.46	(±0.47)	0.77	-1.45
Phenanthrene	-1.65	(±0.50)	0.90	-0.52	(±0.36)	0.88	-1.13
Pyrene	-1.85	(±1.09)	0.83	-0.27	(±0.57)	0.43	-1.58
Benzo(b)fluoranthene	-2.23	(±1.67)	0.75	-0.58	(±0.92)	0.58	-1.65

loss mechanism	<u>No Growth Model</u>		<u>Yield Included</u>	
	PAH mass loss (mg)	% of observed PAH mass loss	PAH mass loss (mg)	% of observed PAH mass loss
Aerobic	0.24	38	0.34	53
Sulfate-reducing	0.06	9	0.06	9
Abiotic	0.21	33	0.21	33
Unaccounted	0.13	20	0.03	5

---

TABLE 7  
Comparison of First-order Rate Constants in Microcosms  
Containing Either Soil A or Soil B.

compound	Degradation Rate	
	Site A [year <sup>-1</sup> ]	Site B <sup>a</sup> [year <sup>-1</sup> ]
Acenaphthene	-1.57	0.0 <sup>b</sup>
Fluorene	-1.45	-2.41
Phenanthrene	-1.13	-3.28
Pyrene	-1.58	-2.98
Benzo(b)fluoranthene	-1.65	0.0 <sup>b</sup>

<sup>a</sup> First-order degradation rates for a soil sample collected from a location of the site where PAH compounds were not found, as reported previously (12).

<sup>b</sup> Biodegradation of acenaphthene and benzo(b)fluoranthene was not observed in the PAH degradation microcosm study conducted using soil from Site B.

---

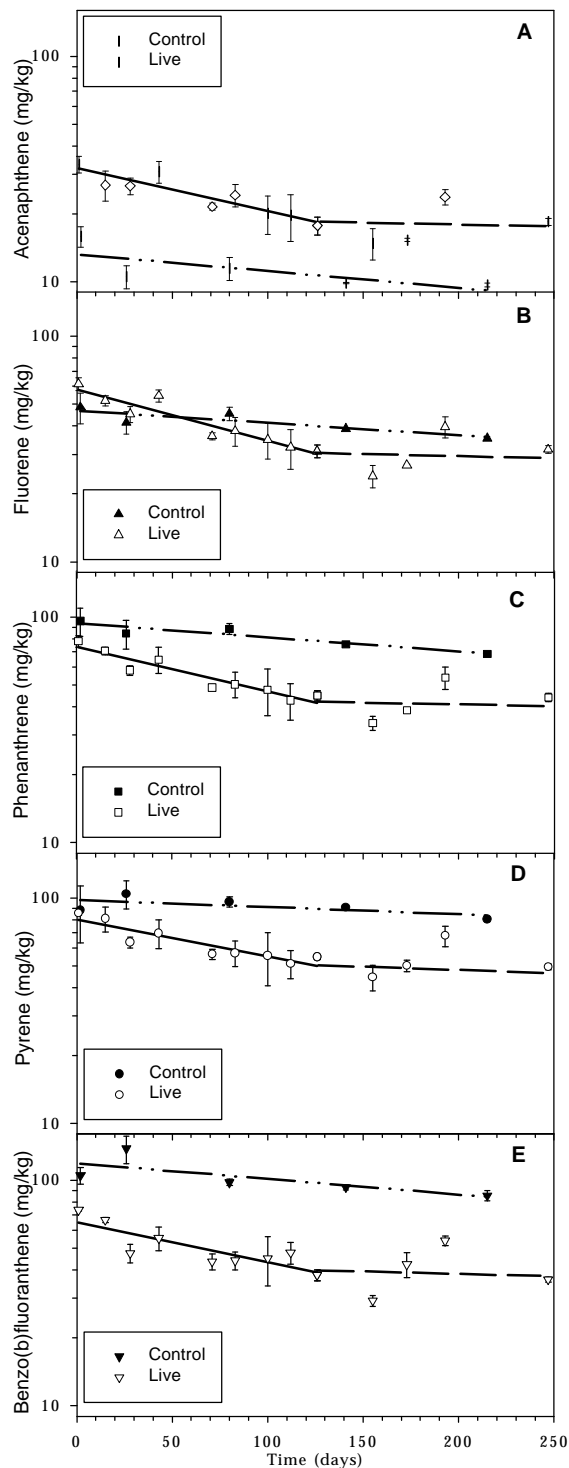


**FIGURE 1. PAH concentration versus time for (A) acenaphthene, (B) fluorene, (C) phenanthrene, (D) pyrene, and (E) benzo(b)fluoranthene in microcosms containing soil from Site A. The dash dotted (— · ·) line represents the best fit regression line for the control microcosms. The solid (—) line represents the best fit through the live microcosms during the ‘active’ phase, while the dashed (— —) line represents the best fit line during periods when the live microcosms were inactive. Error bars represent  $\pm$  one standard deviation in the concentration measurement.**

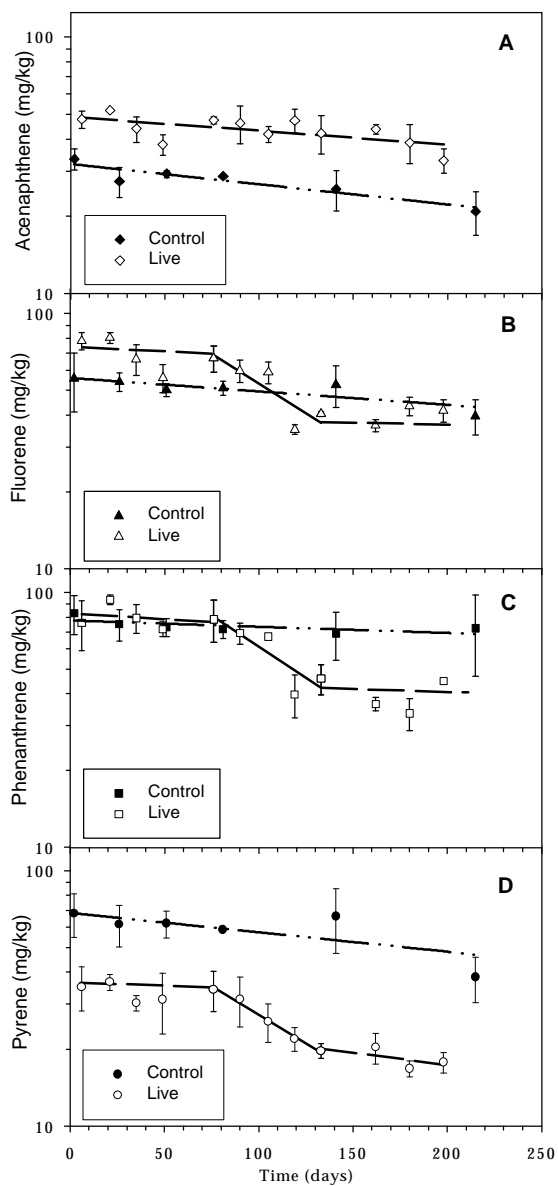


**FIGURE 2. PAH concentration versus time for (A) acenaphthene, (B) fluorene, (C) phenanthrene, and (D) pyrene in microcosms containing soil from Site B. The dash dotted (— · ·) line represents the best fit regression line for the control microcosms. The solid (—) line represents the best fit through the live microcosms during the ‘active’ phase, while the dashed (— —) line represents the best fit line during periods when the live microcosms were inactive. Error bars represent  $\pm$  one standard deviation in the concentration measurement. (Modified from (12).)**

## Literature Cited

- (1) U.S. Environmental Protection Agency. Use of Monitored Natural Attenuation at Superfund, RCRA Corrective Action, and Underground Storage Tank Sites. Directive 9200.4-17P. 1999.
- (2) Gibson, D.T.; Mahadevan, V.; Jerina, D.M.; Hagi, H.J.; Yeh, H.J.C. 1975. *Science*. 189, 295-297.
- (3) Bauer, J.E.; Capone, D.G.. **1988**, *Appl. Environ. Microbiol.* 54, 1649-1655.
- (4) Leduc, R.; Sampson, R.; Al-Bashir, B.; Al-Hawari, J.; Cseh, T. **1992**, *Environ. Sci. Tech.* 26, 51-60.
- (5) Mihelcic, J.R.; Luthy, R.G. **1988a**, *Appl. Environ. Microbiol.* 54, 1182-1187.
- (6) Mihelcic, J.R.; Luthy, R.G. **1988b**, *Appl. Environ. Microbiol.* 54, 1188-1198.
- (7) McNally, D.L.; Mihelcic, J.R.; Lueking, D.R. **1998**, *Environ. Sci. Tech.* 32, 2633-2639.
- (8) Coates, J.D.; Anderson, R.T.; Lovley, D.R. **1996**, *Appl. Environ. Microbiol.* 62(3), 1099-1101.
- (9) Coates, J.D.; Woodward, J.; Allen, J.; Philip, J.; Lovley, D.R. **1997**, *Appl. Environ. Microbiol.* 63(9), 3589-3593.
- (10) Durant, N.D.; Wilson, L.P.; Bouwer, E.J. **1995**, *J. Contam. Hydrol.* 17, 213-237.
- (11) Lee, W.L. (pers. comm., 1996)
- (12) Brauner, J.S.; Widdowson, M.A.; Novak, J.T.; Love, N.G. In *The Fifth International Symposium on in Situ and On-Site Bioremediation*. April 19-22, 1999, San Diego, CA; Leeson, A., Alleman, B.C., Eds.; Battelle Press: Columbus, OH, 1999; Vol 5(8), pp.19-24.
- (13) Wilson, B.H.; Wilson, J.T., and Luce, D. **1996**, Proceedings of the Symposium on Natural Attenuation of Chlorinated Organics in Ground Water. Dallas, TX, September 11-13. p. 23-30.
- (14) McFarland, M.J.; Sims, R.C. **1991**, *Ground Water*. 29(6):885-896.
- (15) Zehnder and Stumm. Geochemistry and biochemistry of anaerobic habitats. In: *Biology of Anaerobic Microorganisms*; Zehnder, A.J.B., Ed.; John Wiley and Sons, Inc. New York, 1988.
- (16) Stumm, W.; Morgan, J.J. *Aquatic Chemistry*. J. Wiley & Sons, New York.. 1981. Chapter 7.
- (17) Grady, C.P.L.; Daigger, G.T.; Lim, H.C. *Biological Wastewater Treatment, 2<sup>nd</sup> Ed.*; Marcel Dekker, Inc., New York. 1999, pp. 61-78.
- (18) McCarty, P.L. Energetics and Bacterial Growth. *Organic Compounds in Aquatic Environments*; Marcel Dekker, Inc., New York. 1971.
- (19) Karickhoff, S.W. In *Contaminants and Sediments. Volume 2. Fate and Transport Studies, Modeling, Toxicity*; Baker, R.A., Ed.; Ann Arbor Science, Ann Arbor, MI, 1980, pp. 193-205.
- (20) Hatzinger, P.B; Alexander, M. **1995**, *Environ. Sci. Tech.* 29(2):537-545.
- (21) Novak, J.T.; Burgos, W.B.; Bhandari, A. In *Soil and Aquifer Pollution. Non-aqueous Phase Liquids – Contamination and Reclamation*; Rubin, H., Narkis, N., Carberry, J., Eds.; Springer-Verlag, Berlin, 1998, pp.191-206.
- (22) Knightes, C.D.; Peters, C.A. In *The Fifth International Symposium on in Situ and On-Site Bioremediation*. April 19-22, 1999, San Diego, CA; Leeson, A., Alleman, B.C., Eds.; Battelle Press: Columbus, OH, 1999; Vol 5(8), pp. 173-178.
- (23) Sokol, W. **1987**, *Biotech. Bioeng.* 30, 921-927.

## CHAPTER 4

### Impact of Iron(III) and Microbial Distributions on Numerical Modeling of Petroleum Hydrocarbon Fate and Transport

J. STEVEN BRAUNER AND MARK A. WIDDOWSON

*THE CHARLES E. VIA, JR. DEPARTMENT OF CIVIL AND ENVIRONMENTAL ENGINEERING*

*VIRGINIA POLYTECHNIC INSTITUTE AND STATE UNIVERSITY*

#### ABSTRACT

Ferrogenic hydrocarbon biodegradation has been observed during monitored natural attenuation (MNA) studies at numerous petroleum hydrocarbon-contaminated sites. Although hydrocarbon utilization rates under iron(III)-reducing conditions and the concentration of bioavailable iron(III) present in various aquifer systems has been reported in the literature, and the quantitative influence of these factors (i.e., assimilative capacity) has been investigated, an understanding of the potential role of ferrogenic biodegradation on the natural attenuation of petroleum hydrocarbon compounds in groundwater has not been fully explored. In an effort to further our understanding, numerical experiments were conducted using a three-dimensional solute transport model (SEAM3D) to simulate an instantaneous release of biodegradable hydrocarbon into a hypothetical, but realistic heterogeneous hydraulic conductivity field. The purpose of this study was to evaluate the quantitative impact of ferrogenic biodegradation on hydrocarbon plume transport and dispersion, biodegraded mass and peak concentration reduction by comparing sequential aerobic/ferrogenic model results with results in which hydrocarbon biodegradation occurred solely under aerobic conditions.

The results indicated that, for the range of initial conditions for the iron(III) concentration variable considered (50-150  $\mu\text{g Fe}^{3+}/\text{g soil}$ ) and the simulation time (2,000 days), the majority of

hydrocarbon biodegradation (70-80%) was attributed to iron reduction, while the remaining percentage of hydrocarbon biodegradation (20-30%) was aerobic. Ferrogenic biodegradation was identified as the dominant terminal electron accepting process, in terms of hydrocarbon mass biodegraded, within 200 days after contaminant release. Ferrogenic biodegradation was responsible for an order of magnitude decrease in the maximum hydrocarbon concentration in and immediately downgradient of the source area, such that concentrations at one downgradient monitoring point were reduced from 8 mg/L to < 1 mg/L for a initial iron(III) concentration of  $\geq 100 \mu\text{g Fe}^{3+}/\text{g}$  soil. Spatial moment calculations indicate that sequential aerobic/ferrogenic biodegradation caused a greater decrease in the longitudinal center of mass and spatial standard deviation than aerobic only biodegradation. Similar trends were observed in hydrocarbon fate when a second heterogeneous hydraulic conductivity field, of equal statistical parameters but different local hydraulic conductivity distribution than the original heterogeneous flow field, was used. Results from a series of experiments, conducted using multiple heterogeneous distributions of equal mean for the initial iron(III) concentration distribution, showed variation in plume concentration and mass biodegraded, but the level of iron(III) concentration in and immediately downgradient of the source area ultimately determined the extent of hydrocarbon biodegradation. Correlating either the initial iron(III) concentration or initial ferrogenic microbial population to hydraulic conductivity did not consistently increase or decrease biodegradation relative to simulations using a homogeneous initial distribution for either of these parameters. Given the ubiquitous nature of iron(III) in the subsurface, these results suggest that the inclusion of ferrogenic biodegradation is essential for proper evaluation of MNA as a remediation strategy at petroleum-contaminated sites, as ferrogenic biodegradation will effectively shorten the time estimate for contaminant mass removal, while also reducing peak hydrocarbon contaminant concentrations and enhancing plume attenuation.

## Introduction

Regulatory acceptance of monitored natural attenuation (MNA) as a remediation strategy for petroleum hydrocarbon-contaminated sites is dependent on the efficacy of aerobic and anaerobic

microbial processes removing contaminants within a reasonable time frame when compared to other available remediation options and before reaching site-specific points of concern (USEPA, 1999). Although the rates of biodegradation for anaerobic processes have often been reported as an order of magnitude or more less than aerobic biodegradation rates, anaerobic biodegradation may contribute significantly to the overall mass of contaminant removed if the groundwater velocity is slow relative to the rate of substrate biodegradation (Sturman et al., 1995; Chapelle and Bradley, 1998). Using a mass balance approach where the ability of an aquifer system to biodegrade hydrocarbon compounds under specific redox conditions was estimated, Kennedy et al. (1999) calculated that the assimilative capacity for hydrocarbon biodegradation by iron(III)-reduction was much greater than the combined assimilative capacity of oxygen and nitrate in a gasoline contaminated aquifer in Oklahoma. Numerical models for natural attenuation may serve as an important tool for interpreting whether the assimilative capacity of an aquifer system will allow site-specific treatment goals to be attained for specific contaminants of concern by incorporating the effects of solute transport, biodegradation kinetics, and electron acceptor in calculations of hydrocarbon fate and transport.

Research by Lovley et al. (1993) has shown that ferrogenic bacteria are capable of biodegrading a wide variety of organic groundwater contaminants. The total mass of  $\text{Fe}^{3+}$  measured in aquifer sediments at petroleum hydrocarbon-contaminated sites has been reported as approximately 1 percent of the dry weight of soil sediments ( $\sim 10,000$  mg  $\text{Fe}^{3+}$ /g soil) by Parkhurst et al. (1993), Libelo et al. (1997), and Kennedy et al. (1999). Work by Munch and Ottow (1980), Lovley and Phillips (1986), and Lovley et al. (1989) showed that iron found in amorphous  $\text{Fe}^{3+}$  oxyhydroxides (e.g. ferrihydrite) were preferentially used over crystalline forms during microbial  $\text{Fe}^{3+}$ -reduction in laboratory incubations. Lovley and Phillips (1987) adapted a hydroxylamine extraction technique developed by Chao and Zhou (1983) and found that hydroxylamine-reducible iron concentrations were representative of bioavailable iron concentrations at two hydrocarbon contaminated sites. Maximum hydroxylamine-reducible iron concentrations were observed to range from zero to  $6700$   $\mu\text{g}$   $\text{Fe}^{3+}$ /g soil in fresh water river sediment samples and from zero to

22  $\mu\text{g Fe}^{3+}/\text{g}$  soil in a mixed sand and gravel aquifer (Lovely and Phillips, 1987). More recently, field measurements by Kennedy et al. (1999) reported the bioavailable  $\text{Fe}^{3+}$  concentration using a 0.5 M hydrochloric acid assay in a finely grained, poorly cemented, sandstone aquifer to be greater than 200  $\mu\text{g Fe}^{3+}/\text{g}$  soil. Kennedy et al. (1999) also reported that bioavailable  $\text{Fe}^{3+}$  was distributed non-uniformly by an unknown depositional or geological process.

Research has shown increased microbial activity in zones of higher hydraulic conductivity in heterogeneous flow systems (Chapelle and Lovley, 1990; Konopka and Turco, 1991; Thomas and Ward, 1992; Aelion and Long, 1994). Chapelle and Lovley (1990) indicated a correlation between microbial activity and hydraulic conductivity that may have occurred due to increased microbial and nutrient mobility in sandy aquifer sediments relative to clayey sediments. Intermediate scale experiments in a meter long flow cell by Murphy et al. (1997) found that biomass detachment to the aqueous phase and advective transport through zones of higher hydraulic conductivity produced local variations in the biomass distribution which were correlated to zones of higher hydraulic conductivity. Waddill (1998) correlated the microbial population to the hydraulic conductivity distribution for hydrocarbon solute transport simulations under sequential aqueous phase electron acceptor conditions and found that the mass of hydrocarbon biodegraded was more sensitive to variations in hydraulic conductivity than it was to variations in the microbial population. To date, there is no research on how heterogeneity in the ferrogenic microbial population affects either hydrocarbon or  $\text{Fe}^{3+}$  consumption.

The purpose of this study was to evaluate the impact of microbially-based  $\text{Fe}^{3+}$  reduction and the initial bioavailable  $\text{Fe}^{3+}$  concentration on natural attenuation of a hypothetical petroleum hydrocarbon plume. Specifically, this study investigates how the mass, concentration, center of mass, and longitudinal spreading of the hydrocarbon plume are affected by the inclusion of ferrogenic biodegradation. Numerical experiments were conducted using the numerical transport model SEAM3D (Waddill and Widdowson, 1998) to simulate three-dimensional solute transport and biodegradation of an instantaneous slug injection of biodegradable hydrocarbon through a hypothetical, but realistic hydraulic conductivity field. Currently,

SEAM3D is the only fate and transport model that explicitly simulates  $\text{Fe}^{3+}$  utilization when hydrocarbon biodegradation is occurring under ferrogenic conditions, thus allowing SEAM3D to limit the mass of hydrocarbon biodegraded based on the availability of  $\text{Fe}^{3+}$ . The impact of including  $\text{Fe}^{3+}$ -reduction in numerical simulations of MNA was evaluated by comparing model results from the base case model, which simulated sequential aerobic/ $\text{Fe}^{3+}$ -reducing biodegradation and homogeneous initial electron acceptor conditions, with results from a model that simulated hydrocarbon biodegradation solely under aerobic conditions. Both the starting  $\text{Fe}^{3+}$  concentration and the spatial  $\text{Fe}^{3+}$  concentration distribution were varied to quantify the impact of the starting  $\text{Fe}^{3+}$  condition on numerical simulations of natural attenuation. Numerical results from a simulation where the microbial population was correlated to hydraulic conductivity were also examined and compared to the base case. Hydrocarbon fate and transport through a second heterogeneous flow field was simulated for selected initial  $\text{Fe}^{3+}$  conditions to determine whether earlier findings were dependent on the original heterogeneous flow field. Variation between simulations was assessed using model results for hydrocarbon and electron acceptor concentration distributions, the mass of biodegraded hydrocarbon, and spatial moment calculations for the hydrocarbon plume centroid and spatial standard deviation.

## Hypothetical Model

The hypothetical model used in this study consisted of numerical model for groundwater flow through a heterogeneous hydraulic conductivity field and a solute transport model that simulated sequential aerobic/ferrogenic biodegradation for both homogeneous and heterogeneous initial  $\text{Fe}^{3+}$  concentration distributions. This section describes both the assumptions and components of the groundwater flow and solute transport models in detail.

### Model Assumptions

A conceptual model for biodegradation was developed using the following assumptions. A single hydrocarbon compound was subjected to sequential biodegradation in the presence of aerobic and ferrogenic microbial populations. Aerobic biodegradation was simulated during each simulation, as the

majority of hydrocarbon spills occur in near-surface aquifers that are naturally aerobic. The hydrocarbon served as the sole electron donor and carbon-source for microbial growth. To isolate the effects of biodegradation, the hydrocarbon was modeled as non-sorbing. A uniform ambient oxygen concentration was assumed and the specified initial  $\text{Fe}^{3+}$  concentration was considered the only source of bioavailable  $\text{Fe}^{3+}$  (i.e. microbially-reduced  $\text{Fe}^{2+}$  was assumed to precipitate into a non-bioavailable form). Aqueous phase  $\text{Fe}^{2+}$  reaction with oxygen was not simulated, as oxygen was assumed to inhibit  $\text{Fe}^{3+}$ -reducing activity and limit interaction between these compounds. Other environmental conditions (e.g. temperature, pH, nutrient concentrations) were assumed as favorable for biodegradation and constant with respect to space and time. Microbial growth was assumed to occur for two independent microbial populations, one aerobic and one ferrogenic. This conceptual model for biodegradation facilitates interpretation of ferrogenic biodegradation effects and may be an appropriate model for aquifers where the background concentrations of nitrate is close to zero and the contribution of sulfate-based and methanogenic activity to hydrocarbon biodegradation is insignificant when compared to aerobic and/or ferrogenic biodegradation.

### **Groundwater Flow Model and Numerical Grid**

MODFLOW (MacDonald and Harbaugh, 1988) was used to simulate fully three-dimensional, steady state groundwater flow, through the confined aquifer system shown in Figure 1. The governing equation for steady state groundwater flow in a confined aquifer is given by:

$$\frac{\partial}{\partial x} \left( K_x \frac{\partial h}{\partial x} \right) + \frac{\partial}{\partial y} \left( K_y \frac{\partial h}{\partial y} \right) + \frac{\partial}{\partial z} \left( K_z \frac{\partial h}{\partial z} \right) = 0 \quad (1)$$

where  $K_x$ ,  $K_y$ , and  $K_z$  are the hydraulic conductivity in the longitudinal, transverse, and vertical directions, respectively [L/T], and  $h$  is hydraulic head [L].

No flow boundaries were specified along the top, bottom, and longitudinal boundaries of the model domain. Heads along the transverse boundaries were specified as constant, and a 0.1 m head differential between the upstream ( $x = 0$  m) and downstream ( $x = 40$  m) boundaries produced an average

hydraulic gradient of 0.0025 m/m in the longitudinal direction. All model layers were simulated as fully saturated, with flow between layers simulated using the MODFLOW vertical leakance term.

As shown in Figure 1, the dimensions of the hypothetical model domain were 40-m by 20-m by 3-m. The horizontal and vertical grid spacing was chosen based on research by Ababou (1988), which indicated that a minimum of 4 nodes per correlation scale is required when using discretized models to capture variability in heterogeneously distributed parameters. Based on this criterion, a fine horizontal and vertical grid spacing of 0.5 m and 0.05 m, respectively, was used to discretize the model domain into 80 rows, 40 columns, and 30 layers.

### **Hydraulic Conductivity Field**

A hypothetical heterogeneous hydraulic conductivity field, designated as distribution A, was developed for the model domain using statistical parameters that were reported as typical for a sandy loam soil by Carsel and Parrish (1988). Horizontal hydraulic conductivity was assumed locally isotropic, while geological deposition was assumed to produce vertical hydraulic conductivities that were smaller than the horizontal component. Using the statistical parameters listed in Table 1, specific values for the horizontal components of hydraulic conductivity at each node were generated using the turning bands method (Mantoglou and Wilson, 1982) as implemented by Tompson et al. (1987). A horizontal to vertical anisotropy ratio ( $K_x$  to  $K_z$ ) was specified as 2:1 at all locations. Figure 2 shows horizontal and vertical cross sections of the hydraulic conductivity distribution, taken through the centerline of the model domain. Values for the horizontal component of hydraulic conductivity in distribution A ranged from a minimum of 0.013 m/d to a maximum of 75.6 m/d.

### **Solute Transport Model**

SEAM3D (Waddill and Widdowson, 1997) was used to simulate solute transport and microbial utilization of two solutes (a reactive hydrocarbon and oxygen) and one solid phase electron acceptor ( $\text{Fe}^{3+}$ ). Solute transport of a conservative tracer was also simulated, with model results for tracer transport serving as a baseline for evaluation of reactive transport. Solute transport and electron acceptor-limited

biodegradation is simulated in SEAM3D using the advection-dispersion equation, as developed in Waddill and Widdowson (1998), and given by

$$R \frac{\partial C}{\partial t} = \frac{\partial}{\partial x_i} \left( D_{ij} \frac{\partial C}{\partial x_j} \right) - \frac{\partial}{\partial x_i} (v_i C) - R_{sink,C}^{Bio} \quad (2)$$

where  $R$  is the retardation factor [-];  $C$  is the aqueous phase solute concentration for either the tracer (T), substrate (S), or oxygen (O) [ $M L^{-3}$ ];  $t$  is time [T];  $x_i$  is distance in the  $i^{th}$  direction [L];  $D_{ij}$  is the hydrodynamic dispersion coefficient tensor [ $L^2 T^{-1}$ ];  $v_i$  is the average pore water velocity in the  $i^{th}$  direction [ $L T^{-1}$ ]; and  $R_{sink,C}^{Bio}$  is the rate of solute loss due to biodegradation [ $M_S L^{-3} T^{-1}$ ]. Since sorption effects were ignored for the hypothetical model,  $R$  was equal to one for all solutes. Conservative transport of the tracer was simulated by setting  $R_{sink,C}^{Bio}$  equal to zero. The mass balance equation for the solid phase electron acceptor,  $Fe^{3+}$ , is

$$\frac{\partial F}{\partial t} = -R_{sink,F}^{Bio} \quad (3)$$

where  $F$  is the solid phase iron(III) concentration [ $M_{Fe3} M_{soil}^{-1}$ ] and  $R_{sink,F}^{Bio}$  is the rate of  $Fe^{3+}$  loss due to biodegradation [ $M_{Fe3} L^{-3} T^{-1}$ ].

Hydrocarbon biodegradation under sequential aerobic,  $Fe^{3+}$ -reducing conditions was calculated using a dual Monod kinetic expression for oxygen and a single Monod kinetic term for  $Fe^{3+}$ , given by

$$R_{sink,S}^{Bio} = \frac{I}{q} \left( M_1 \mathbf{n}_1^{max} \left[ \frac{\bar{S}}{\bar{K}_O^S + \bar{S}} \right] \left[ \frac{\bar{O}}{\bar{K}^O + \bar{O}} \right] + M_2 \mathbf{n}_2^{max} \left[ \frac{\bar{S}}{\bar{K}_F^S + \bar{S}} \right] I_{F,O} \right) \quad (4)$$

where  $\bar{S}$  is the effective concentration of the substrate [ $M_S L^{-3}$ ];  $\bar{O}$  is the effective concentration of oxygen [ $M_O L^{-3}$ ];  $q$  is the effective porosity [-],  $M_x$  is the biomass concentration for the aerobic ( $x = 1$ ) and ferrogenic ( $x = 2$ ) populations [ $M_B L^{-3}$ ];  $\mathbf{n}_x^{max}$  is the maximum specific rate of substrate utilization for each population  $x$  [ $M_S M_B^{-1} T^{-1}$ ];  $\bar{K}_O^S$  is the effective half saturation constant for aerobic substrate utilization [ $M_S L^{-3}$ ];  $\bar{K}^O$  is the effective half saturation constant for oxygen [ $M_O L^{-3}$ ];  $\bar{K}_F^S$  is the effective

half saturation constant for substrate utilization under ferrogenic conditions [ $M_F L^{-3}$ ]; and  $I_{F,O}$  is an inhibition function defined by

$$I_{F,O} = \left[ \frac{\mathbf{k}_{F,O}}{\mathbf{k}_{F,O} + \bar{O}} \right] \quad (5)$$

where  $\mathbf{k}_{F,O}$  is the inhibition coefficient representing oxygen inhibition of  $Fe^{3+}$  consumption [ $M_O L^{-3}$ ]. In the event that microbial utilization results in depletion of  $Fe^{3+}$ , the single Monod term for substrate utilization by the  $Fe^{3+}$ -reducing population in Equation (4) is set equal to zero.

Oxygen consumption during biodegradation is calculated using a dual Monod kinetic expression given by

$$R_{sink,O}^{Bio} = \frac{M_1}{q} \mathbf{g}_O \mathbf{n}_1^{max} \left[ \frac{\bar{S}}{\bar{K}_O^S + \bar{S}} \right] \left[ \frac{\bar{O}}{\bar{K}^O + \bar{O}} \right] \quad (6)$$

where  $\gamma_O$  is the oxygen use coefficient [ $M_O M_S^{-1}$ ].  $Fe^{3+}$  utilization is calculated using a single Monod kinetic expression, given as

$$R_{sink,F}^{Bio} = \frac{M_2}{r_b} \mathbf{g}_F \mathbf{n}_2^{max} \left[ \frac{\bar{S}}{\bar{K}_F^S + \bar{S}} \right] I_{F,O} \quad (7)$$

where  $\gamma_F$  is the  $Fe^{3+}$  use coefficient [ $M_F M_S^{-1}$ ] and  $r_b$  is the bulk mass density of the porous medium [ $M_{SOLID} L^{-3}$ ]. When  $Fe^{3+}$  is depleted or reaches a user defined minimum threshold, Equation (7) is set to zero.

Growth for the aerobic and ferrogenic microbial populations were calculated using

$$\frac{1}{M_1} \frac{\partial M_1}{\partial t} = Y_1 \mathbf{n}_1^{max} \left[ \frac{\bar{S}}{\bar{K}_O^S + \bar{S}} \right] \left[ \frac{\bar{O}}{\bar{K}^O + \bar{O}} \right] - k_{d,1} \quad (8a)$$

and

$$\frac{1}{M_2} \frac{\partial M_2}{\partial t} = Y_2 \mathbf{n}_2^{max} \left[ \frac{\bar{S}}{\bar{K}_F^S + \bar{S}} \right] I_{F,O} - k_{d,2} \quad (8b)$$

where  $Y_x$  is the yield coefficient for population  $x$  [ $M_B M_S^{-1}$ ], representing the biomass produced per unit mass of substrate consumed, and  $k_{d,x}$  is the decay coefficient for each microbial population  $x$  [ $T^{-1}$ ].

For the numerical experiments in this study, heterogeneity in the groundwater flow and solute transport field was simulated using a randomly generated flow field with local-scale dispersivity ( $\alpha_L \leq 10$  cm). This approach was used so that the influence of aquifer heterogeneity on hydrocarbon transport could be investigated, while the impact of large-scale dispersivity on biodegradation could be minimized. For example, MacQuarrie and Sudicky (1990) found that simulating biologically reactive hydrocarbon transport using a random heterogeneous hydraulic conductivity distribution with local scale dispersivity produced model results that were in agreement with field observations of benzene in the Borden aquifer, whereas using a homogeneous hydraulic conductivity distribution and large-scale macrodispersivity to simulate the effects of heterogeneous transport caused the model to overpredict aerobic hydrocarbon biodegradation. MacQuarrie and Sudicky (1990) and later research by Miralles-Wilhelm et al. (1997) indicated that the use of macrodispersivity is largely inappropriate for biologically reactive solute transport models, as large values for dispersivity produce artificial mixing between the hydrocarbon and aqueous phase electron acceptors. Brauner and Widdowson (2000) found that results from biologically reactive solute transport through heterogeneous hydraulic conductivity fields were insensitive to adjustments in local-scale longitudinal dispersivity values.

### **Solute Transport and Biodegradation Parameters**

Solute transport equations were solved using a third order TVD scheme based on the ULTIMATE algorithm (Leonard, 1988). A Courant number of 1.0 was used to satisfy stability and accuracy requirements of the SEAM3D model. Based on this criterion, the model-calculated maximum allowable time step was 1.06 days. Solute transport during each simulation was simulated for 2000 days, which translated into run times of approximately 12 hours on a Pentium 400MHz PC with 256MB of RAM. The remaining solute transport parameters (dispersivity, effective porosity, and soil bulk density) were assumed constant throughout the model domain and are listed in Table 2. The ratio of longitudinal to transverse to vertical dispersivity was specified as 1.0 to 0.1 to 0.01. A porosity of 0.35 was considered

typical for sandy aquifers. Carsel and Parrish (1988) reported a soil bulk density of  $1.66 \times 10^{-6} \text{ g/m}^3$  as typical for sandy soils.

Initial and boundary conditions were designed to simulate an instantaneous slug injection of a dissolved mixture of conservative tracer and reactive hydrocarbon. The slug injection was specified using an initial concentration of 60 mg/L for both the tracer and hydrocarbon in all model cells of the 4 x 4 x 0.4 m source area shown in Figure 1. Tracer and hydrocarbon concentrations at all other locations were specified as zero. The initial concentration of aqueous phase electron acceptor (i.e. oxygen) was 3.0 mg/L throughout the entire domain. Distribution of  $\text{Fe}^{3+}$  varied by simulation, but the mean starting concentration was  $100 \mu\text{g Fe}^{3+}/\text{g soil}$ , unless otherwise indicated. The upgradient ( $x = 0$ ) boundary was specified as a constant concentration boundary, with the constant concentrations specified as identical to the background concentrations for all constituents. Zero-gradient conditions were specified along the top, bottom, longitudinal, and downgradient boundaries.

Hydrocarbon biodegradation under sequential aerobic/iron(III)-reducing conditions was simulated using the biodegradation parameters listed in Table 3. Both the maximum specific utilization rate and initial microbial populations were chosen within the range of values reported from a calibrated modeling study at one site where aerobic and ferrogenic microbial activity was simulated (Brauner and Widdowson, 2000). For all but two simulations, the starting microbial population distributions were assumed as uniformly distributed throughout the model domain. For the remaining two simulations, the distribution of both the aerobic and ferrogenic microbial populations was assumed to be correlated to the hydraulic conductivity field. For this special case, the minimum and maximum initial concentrations for the aerobic microbial population were 0.011 and  $0.86 \text{ g}_{\text{bio}}/\text{m}^3$ , respectively. Minimum and maximum concentrations for the ferrogenic population were exactly one order of magnitude less than the values of the aerobic population. Values for the yield coefficient and half saturation constants were chosen within the range reported for monoaromatic hydrocarbons in the literature (e.g. Suarez and Rifai, 1999). Electron acceptor use coefficients were based on stoichiometric calculations for complete mineralization of toluene

to carbon dioxide. The inhibition coefficient chosen for this study resulted in significant inhibition of iron(III)-reduction in locations where oxygen concentrations were greater than 0.10 mg<sub>O<sub>2</sub></sub>/L.

### **Iron(III) Concentration and Distribution**

Three homogeneous and eleven heterogeneous Fe<sup>3+</sup> distributions were used to investigate how changes in the Fe<sup>3+</sup> initial condition affected model results. The starting concentration of bioavailable Fe<sup>3+</sup> for the base case model was specified as 100 µg Fe<sup>3+</sup>/g soil, which falls between the 22 µg Fe<sup>3+</sup>/g soil bioavailable Fe<sup>3+</sup> concentration reported by Lovley and Phillips (1987) and the greater than 200 µg Fe<sup>3+</sup>/g soil bioavailable Fe<sup>3+</sup> concentration reported by Kennedy et al. (1999). Since this starting concentration for Fe<sup>3+</sup> was arbitrarily selected, two additional simulations were conducted using a homogenous Fe<sup>3+</sup> starting concentration of 50 µg Fe<sup>3+</sup>/g soil and 150 µg Fe<sup>3+</sup>/g soil, respectively. Heterogeneous realizations for the initial spatial distribution of Fe<sup>3+</sup> concentration were randomly generated and tested using the hypothetical model. No statistical parameters have been reported for bioavailable Fe<sup>3+</sup> distribution, so the correlation scale was arbitrarily chosen as equal to that of the hydraulic conductivity distribution (i.e. 1.5 m horizontally and 0.15 m vertically). To facilitate comparison between model results for the base case and results from heterogeneous distributions of Fe<sup>3+</sup>, the mean bioavailable Fe<sup>3+</sup> concentration was set equal to 100 µg Fe<sup>3+</sup>/g soil for all heterogeneous Fe<sup>3+</sup> distributions. A standard deviation for the log normal Fe<sup>3+</sup> distribution ( $\sigma_{\ln\text{Fe(III)}}$ ) was chosen as 0.5, which produced Fe<sup>3+</sup> concentrations that ranged between 10 to 1000 µg Fe<sup>3+</sup>/g soil. As with the hydraulic conductivity field, values for Fe<sup>3+</sup> at individual model nodes were generated using the turning bands method. Table 4 lists the naming convention that will be used in the results section to describe initial condition for each simulation.

### **Method of Analysis**

Hydrocarbon plume behavior was investigated using a combination of hydrocarbon contour plots, mass balance calculations, and method of moments calculations. Trends in contour plots of electron acceptor concentrations were also evaluated and included as part of model assessment. Cross sections for

contour plots were all taken along either the horizontal ( $y = 10$  m) or the vertical ( $z = 1.5$  m) centerlines of the model domain at 1000 and 2000 days into the model simulation. SEAM3D mass balance options were specified to report both the mass of hydrocarbon remaining in the domain and the mass of hydrocarbon biodegraded by each electron acceptor process at user specified times. This latter option was used to determine which electron acceptor process was dominant for a given simulation, and whether the dominant electron acceptor process varied with time.

The method of spatial moments was used to quantitatively access average, large-scale movement of the hydrocarbon plume. This method, as defined by Aris (1956) and implemented for SEAM3D by Waddill (1998), calculates the  $ijk^{th}$  spatial moment of a solute of concentration  $C$  at time  $t$  using

$$M_{ijk}(t) = \int_{-\infty}^{\infty} \int_{-\infty}^{\infty} \int_{-\infty}^{\infty} \mathbf{q}(x, y, z, t) \cdot C(x, y, z, t) \cdot x^i y^j z^k \cdot \mathbb{1}x\mathbb{1}y\mathbb{1}z \quad (8)$$

where  $\mathbf{q}$  is the porosity [ $L^3/L^3$ ]. The zero order moment ( $i = j = k = 0$ ) estimates the total mass of solute in the domain at any time ( $t$ ). The first spatial moments with respect to  $x$  ( $i = 1$ ),  $y$  ( $j = 1$ ), and  $z$  ( $k = 1$ ) ( $M_{100}$ ,  $M_{010}$ ,  $M_{001}$ ) locates the center of mass ( $x_c$ ,  $y_c$ ,  $z_c$ ) of the solute plume, and are calculated as

$$x_c = M_{100}/M_{000} \quad ; \quad y_c = M_{010}/M_{000} \quad ; \quad z_c = M_{001}/M_{000} \quad (9)$$

and describe the average location of the hydrocarbon plume. The spatial standard deviations ( $\sigma_{xx}$ ,  $\sigma_{yy}$ ,  $\sigma_{zz}$ ) of the plume quantifies the degree of plume spreading and are calculated using the second spatial moments ( $M_{200}$ ,  $M_{020}$ ,  $M_{002}$ ) for the  $x$  ( $i = 2$ ),  $y$  ( $j = 2$ ), and  $z$  ( $k = 2$ ) directions using:

$$\mathbf{s}_{xx} = \sqrt{\frac{M_{200}}{M_{000}} - x_c^2} \quad ; \quad \mathbf{s}_{yy} = \sqrt{\frac{M_{020}}{M_{000}} - y_c^2} \quad ; \quad \mathbf{s}_{zz} = \sqrt{\frac{M_{002}}{M_{000}} - z_c^2} \quad . \quad (10)$$

Hydrocarbon concentration versus time at two hypothetical monitoring points was also recorded and compared to quantify differences between model simulations. Both points were located at the mid-elevation ( $z = 1.5$  m) and on the transverse centerline ( $y = 10$ m) of the model domain. These points are shown in Figure 1 as monitoring point 1 (MP1) and monitoring point 2 (MP2). MP1 was 4 m

downgradient of the source area ( $x = 10$  m), while MP2 was 14 m downgradient of the source area ( $x = 20$  m).

## Results

### Tracer and Aerobic Biodegradation

Figure 3 depicts tracer, hydrocarbon, and oxygen concentration distributions for the aerobic only (Case A0) simulation along horizontal and vertical cross sections, taken through the model centerline, at 1000 and 2000 days. As shown in the top row of Figure 3, simulating conservative solute transport through the heterogeneous hydraulic conductivity field produced an irregularly-shaped solute plume, which was moving toward the downgradient boundary. By 2000 days, the majority of the tracer had left the source area, and the leading edge of the plume had reached the downgradient boundary. The middle row of Figure 3 shows that aerobic biodegradation produced a hydrocarbon plume that was smaller than the tracer plume in both the horizontal and vertical directions. The bottom row of Figure 3 indicates that the zone of oxygen depletion was nearly identical in size and shape to the hydrocarbon plume.

### Sequential Aerobic/Ferrogenic Biodegradation

The addition of ferrogenic biodegradation caused the model to predict increased hydrocarbon biodegradation, which was observed in model results as a general decrease in hydrocarbon concentrations and an increase in the mass of biodegraded hydrocarbon. Figure 4 depicts hydrocarbon and electron acceptor concentrations along the horizontal and vertical centerline cross sections for sequential aerobic/ferrogenic biodegradation of the hydrocarbon substrate (Case A1). As observed by comparing the middle row of Figure 3 with the top row of Figure 4, the addition of ferrogenic-based biodegradation had little effect on the longitudinal spread of the hydrocarbon plume (defined by the 0.01 and 0.1 mg/L contours) at both 1000 and 2000 days. Concentrations in the interior of the hydrocarbon plumes (defined here by the 1 and 10 mg/L contours) for Cases A0 and A1 were also similar at 1000 days. By 2000 days into the simulations, however, the volume of the Case A1 hydrocarbon plume defined by the 1 mg/L

contour was greatly reduced when compared to Case A0, and concentrations greater than 10 mg/L were nearly eliminated during the simulated sequential biodegradation of Case A1.

Figure 4 also shows the oxygen and  $\text{Fe}^{3+}$  concentration distributions at 1000 and 2000 days into Case A1. Although, the overall length of the oxygen-depleted zone was similar between Cases A0 and A1, the transverse width of the oxygen-depleted zone was approximately a meter narrower for the sequential biodegradation simulation. For both Case A0 and Case A1, oxygen concentrations in and around the source area were near zero at 1000 days, but were returning to background concentrations by 2000 days due to downgradient migration of the hydrocarbon and the ambient flux of oxygen into the source area from the upgradient model boundary. The zone of  $\text{Fe}^{3+}$  depletion for Case A1, shown in the bottom row of Figure 4, was much smaller than both the hydrocarbon plume and zone of oxygen depletion.  $\text{Fe}^{3+}$  concentrations in the source area were depleted by 1000 days into the Case A1 simulation, and the zone of  $\text{Fe}^{3+}$  depletion was observed to extend past  $x = 15$  m by 2000 days.  $\text{Fe}^{3+}$  depletion was greatest in and immediately downgradient of the source area, as the inhibition function limited ferrogenic activity to oxygen-depleted zones. Also note that  $\text{Fe}^{3+}$  concentrations did not return to ambient concentrations after downgradient migration of the hydrocarbon, as the reduced  $\text{Fe}^{2+}$  endproduct was assumed to precipitate into a non-bioavailable iron compound. By explicitly modeling  $\text{Fe}^{3+}$  utilization, this model result suggests that the future biodegradation potential of an aquifer system may be reduced following exposure to hydrocarbon contamination.

Figure 5 shows the mass of hydrocarbon remaining in the model domain (5A) and the total mass of biodegraded hydrocarbon (5B) as a function of time for the tracer and hydrocarbon in Cases A0 and A1. As shown in Figure 5A, the change in tracer mass in the model domain was negligible over the 2000 day duration of the model simulation, and mass balance calculations indicated a less than 0.5 percent change in tracer mass at 2000 days. In contrast, the mass of hydrocarbon in the model domain was observed to decrease with time when either aerobic (Case A0) or sequential aerobic/ferrogenic (Case A1) biodegradation was simulated. Considering that the mass of tracer leaving the domain was negligible over

the 2000-day simulation, observed decreases in the mass of hydrocarbon were produced solely by biodegradation. Figure 5B, which shows the cumulative mass of hydrocarbon biodegraded by all active biodegradation processes as a function of time, confirms this observation in that the mass of hydrocarbon biodegraded corresponds almost exactly to the difference between the mass of tracer and hydrocarbon in the domain at any given time. Figure 5B also shows that the mass of hydrocarbon biodegraded under sequential biodegradation conditions increased substantially over the mass of hydrocarbon biodegraded aerobically around 150 days, indicating that ferrogenic biodegradation caused the break between the aerobically degraded and sequentially degraded hydrocarbon mass in the domain observed in Figure 7A.

Biodegraded hydrocarbon mass calculations indicate that ferrogenic biodegradation caused a more than 300 percent increase in the mass of hydrocarbon biodegraded by 2000 days. Calculations of hydrocarbon mass loss by electron acceptor condition indicate that, by 500 days into the sequential biodegradation simulation, ferrogenic biodegradation accounted for more cumulative hydrocarbon mass loss than aerobic biodegradation. Further analysis shows that ferrogenic biodegradation remained the dominant mechanism for hydrocarbon mass loss through the remaining 1500 days of the simulation and that, by 2000 days, ferrogenic biodegradation was responsible for nearly 80 percent of the total hydrocarbon mass consumed during the sequential biodegradation simulation.

Figure 6 reports the results of spatial moment calculations for the tracer and hydrocarbon in Cases A0 and A1. Figures 6A, 6B, and 6C show the center of mass for the tracer and hydrocarbon plumes in the longitudinal, transverse, and vertical directions, respectively. As shown in Figure 6A, aerobic biodegradation caused the center of mass for the hydrocarbon plume to remain closer to the source area than center of mass for the tracer by approximately 700 days into the model simulation. Figure 6A also shows that adding ferrogenic biodegradation caused a further decrease in the downgradient migration of the hydrocarbon plume center of mass. The locations of the transverse and vertical centers of mass, shown in Figures 6B and 6C, respectively, were observed to oscillate for both the tracer and the hydrocarbon, reflecting that the plumes were meandering through the heterogeneous hydraulic conductivity field.

Figures 6D, 6E, and 6F show the spatial standard deviations for the tracer and hydrocarbon plumes for Cases A0 and A1 in the longitudinal, transverse, and vertical directions, respectively. The spatial standard deviations were consistently smaller for the hydrocarbons than the tracer, indicating that biodegradation was reducing the spread of the hydrocarbon plume. As shown in Figure 6D, sequential biodegradation caused a greater decrease in the longitudinal spatial standard deviation than aerobic only biodegradation, indicating that the addition of ferrogenic biodegradation produced less longitudinal concentration variation in the hydrocarbon plume. This effect was noted quantitatively in the discussion of Figure 4 in that the sequential biodegradation was observed to noticeably reduce the higher substrate concentrations in and around the source area but to not affect the lower concentrations located at the hydrocarbon plume boundaries. As shown in Figure 6E, the spatial standard deviation of the hydrocarbon plume in the transverse direction was not significantly affected by the addition of ferrogenic biodegradation to the aerobic only simulation, suggesting that aerobic biodegradation was controlling transverse spreading of the hydrocarbon plume. In the vertical direction, the spatial standard deviation was observed to decrease with the addition of each biodegradation process, indicating that ferrogenic biodegradation did affect vertical spreading of the hydrocarbon plume.

The inclusion of ferrogenic biodegradation also produced a decrease in hydrocarbon concentration at the two hypothetical monitoring points, MP1 and MP2. Figure 7 presents the tracer and hydrocarbon concentrations breakthrough curves at MP1 and MP2. At both monitoring points, the peak concentration for the aerobically biodegraded hydrocarbon was approximately 1 mg/L less than the tracer concentration. The addition of ferrogenic biodegradation in the sequential biodegradation model caused a 1.5 mg<sub>HC</sub>/L decrease in the peak hydrocarbon concentrations at MP1, and an 8 mg<sub>HC</sub>/L decrease at MP2. Thus, Ferrogenic biodegradation was not only observed to cause a larger decrease in hydrocarbon peak concentration at both monitoring points than was predicted by aerobic biodegradation, but was also observed to have an increased influence at the monitoring point which was located further from the source. Because oxygen was in the aqueous phase and moving downgradient with the dissolved

hydrocarbon, the majority of oxygen available for hydrocarbon biodegradation was the initial aqueous phase concentration of 3 mg/L. For an initial oxygen concentration of 3 mg/L and an oxygen use coefficient of 3.2 mg<sub>O2</sub>/mg<sub>HC</sub>, stoichiometric calculations indicate that the change in hydrocarbon concentration is 0.94 mg/L, which is nearly identical to the change in concentration observed at both hypothetical monitoring points. In contrast, simulating Fe<sup>3+</sup> as a non-mobile, solid phase electron acceptor caused the hydrocarbon to come into contact with fresh supplies of Fe<sup>3+</sup> during downgradient migration, resulting in the increased influence of ferrogenic biodegradation on hydrocarbon concentration observed in the direction of flow.

The above results suggest that inclusion of ferrogenic biodegradation may affect model predictions for MNA in several ways. The addition of ferrogenic biodegradation was observed to substantially increase the total mass of biodegraded hydrocarbon, which would produce a shorter estimate for the time to remediation, as defined by the time for complete contaminant mass removal from the aquifer. A justifiable reduction in the estimate for the time to remediation may make MNA more attractive when MNA is compared to other remediation alternatives. For the hypothetical case examined here, the addition of ferrogenic biodegradation was not shown to limit longitudinal spreading of the hydrocarbon plume or necessarily prevent downgradient aquifer locations from becoming contaminated, but it was demonstrated that ferrogenic biodegradation could reduce hydrocarbon contaminant concentrations by an order of magnitude or more. Considering that many MNA plans are contingent on reducing maximum contaminant concentrations below a specified level at potential POCs, the reduction in contaminant concentration realized by the inclusion of ferrogenic biodegradation may determine whether MNA can be considered an acceptable alternative in terms of meeting contaminant concentration goals.

### **Variation in Iron(III) Concentration**

Two additional homogeneous Fe<sup>3+</sup> initial conditions were investigated to determine how sensitive model results were to varying the initial bioavailable Fe<sup>3+</sup> concentration within the range reported in the

literature by Lovley and Phillips (1986) and Kennedy et al. (1999). For Case A2, the starting  $\text{Fe}^{3+}$  concentration was reduced by 50 percent to  $50 \mu\text{g Fe}^{3+}/\text{g soil}$ , while the starting  $\text{Fe}^{3+}$  concentration for Case A3 was increased by 50 percent to  $150 \mu\text{g Fe}^{3+}/\text{g soil}$ .

Figure 8 shows the hydrocarbon and electron acceptor concentration distributions for a horizontal slice through the model domain at  $z = 1.5\text{m}$  and 2000 days for Cases A2 and A3. Figure 8 (top row) shows that the overall length of the hydrocarbon plume (defined by the  $0.001 \text{ mg/L}$  contour) did not change with variation of the initial  $\text{Fe}^{3+}$  concentration. The interior of the hydrocarbon plume (defined here by the  $1 \text{ mg/L}$  contour) was notably smaller for an increase in the initial  $\text{Fe}^{3+}$  concentration. The oxygen concentration plots of Figure 8 show that the length of the oxygen-depleted zone did not vary between simulations, although the average horizontal width of the oxygen-depleted zone was observed to be approximately 1 m narrower for Case A3 than it was for Case A2. The horizontal width of the zone of oxygen depletion was observed to narrow for increases in initial  $\text{Fe}^{3+}$  concentration because increased hydrocarbon biodegradation led to a smaller concentration gradient and less hydrocarbon spreading in the transverse direction. Although the length of the depleted  $\text{Fe}^{3+}$  zone decreased with increasing initial  $\text{Fe}^{3+}$  concentrations (Figure 8, bottom row), mass calculations indicated that a larger mass of  $\text{Fe}^{3+}$  was consumed during Case A3 than was consumed during Case A2.

Figures 9A and 9B show the mass of solute in the domain and the location of the center of mass, respectively, versus time for the tracer and hydrocarbon in Cases A0, A1, A2, A3, and A4. As shown in Figure 9A, the mass of hydrocarbon remaining in the domain was observed to decrease for increases in the starting  $\text{Fe}^{3+}$  concentration, starting approximately 200 days into the model simulations. Figure 9B shows that the longitudinal hydrocarbon center of mass remained closer to the source area for increases in the  $\text{Fe}^{3+}$  concentration, although the variation from the base case (A1) was less than 10 percent at 2000 days. The remaining spatial moment calculations indicated that adjusting the initial  $\text{Fe}^{3+}$  concentration by  $\pm 50$  percent produced insignificant changes in the transverse center of mass, vertical center of mass, and spatial standard deviations for the sequentially biodegraded hydrocarbon (data not shown).

Hydrocarbon mass loss calculations indicate that, at 2000 days, a 50 percent decrease in the starting  $\text{Fe}^{3+}$  concentration produced a 22 percent decrease in total hydrocarbon biodegradation, whereas a 50 percent increase in  $\text{Fe}^{3+}$  concentration produced a 12 percent increase in biodegradation. Calculation of hydrocarbon mass consumed by electron acceptor condition indicated that aerobic biodegradation removed the majority of hydrocarbon mass during the first 200 days, regardless of the starting  $\text{Fe}^{3+}$  concentration. The majority of the hydrocarbon mass lost during the remainder of each simulation (i.e.  $200 < t < 2000$  days), however, was by the ferrogenic microbial population. Figure 10 shows the percentage of hydrocarbon biodegraded by each electron accepting process as a function of time for the various starting  $\text{Fe}^{3+}$  concentrations. This figure shows that increasing the starting  $\text{Fe}^{3+}$  concentration caused a decrease in the percentage of hydrocarbon biodegraded aerobically and a corresponding increase in the percentage of hydrocarbon biodegraded ferrogenically.

Hydrocarbon concentration breakthrough curves for the three starting  $\text{Fe}^{3+}$  concentrations are provided in Figure 11. As shown in this figure, increasing the  $\text{Fe}^{3+}$  concentration from 100 to 150  $\mu\text{g Fe}^{3+}/\text{g}$  soil generally produced minor changes in the hydrocarbon concentrations at MP1 and MP2. Decreasing the  $\text{Fe}^{3+}$  concentration from 100 to 50  $\mu\text{g Fe}^{3+}/\text{g}$  soil did not alter the peak concentration at MP1, although hydrocarbon concentrations. Decreasing the  $\text{Fe}^{3+}$  concentration by 50 percent did, however, produce a greater than 250 percent increase in the observed hydrocarbon concentration at MP1, relative to the base case concentration, between 500 and 850 days. The effects of decreasing the  $\text{Fe}^{3+}$  concentration were more dramatic at MP2, where the hydrocarbon concentration for Case A2 was observed to be larger than the concentration observed in the base case starting at 1000 days. By 2000 days, the hydrocarbon concentration was observed to increase from less than 1 mg/L for the base case to greater than 6 mg/L for Case A2. The observed increase in hydrocarbon concentration for decreasing  $\text{Fe}^{3+}$  availability was the result of  $\text{Fe}^{3+}$  depletion between the source area and MP2, and illustrates the advantage of explicitly simulating  $\text{Fe}^{3+}$  utilization during ferrogenic biodegradation.

These results demonstrate that changes in the starting bioavailable  $\text{Fe}^{3+}$  concentration primarily affected hydrocarbon concentrations in the interior of the hydrocarbon plume. Increasing the starting  $\text{Fe}^{3+}$  concentration was observed to increase the total mass of hydrocarbon biodegraded, while reducing the overall demand for dissolved oxygen. Observation of increased hydrocarbon concentrations at two hypothetical monitoring points for decreases in the bioavailable  $\text{Fe}^{3+}$  concentration indicated that decreasing the  $\text{Fe}^{3+}$  concentration limited hydrocarbon biodegradation by producing electron acceptor limited conditions in the aquifer. The observed limitation on ferrogenic hydrocarbon biodegradation due to  $\text{Fe}^{3+}$  availability can only be simulated in models that explicitly model  $\text{Fe}^{3+}$  utilization, and can not be accounted for in first-order kinetics models.

### **Variation in Iron(III) Distribution**

To investigate the effects of  $\text{Fe}^{3+}$  distribution on simulation results, hydrocarbon fate and transport was simulated for ten random heterogeneous  $\text{Fe}^{3+}$  concentration distributions. In terms of mass of hydrocarbon biodegraded, the results indicated that five of the simulations predicted an increase in the mass of hydrocarbon biodegraded relative to the results from Case A1, while the remaining five predicted a decrease in the mass of hydrocarbon biodegraded relative to the base case. The  $\text{Fe}^{3+}$  distributions for two simulations, designated as Cases A4 and A5, caused the model to predict the minimum and maximum masses of biodegraded hydrocarbon, respectively. For Case A4, the model predicted an 11 percent decrease in hydrocarbon biodegradation at 2000 days, when compared to the base case (A1). whereas hydrocarbon biodegradation was observed to increase by nearly 10 percent for Case A5.

Figure 12 reports the hydrocarbon concentration distribution at 2000 days and both the initial and 2000-day  $\text{Fe}^{3+}$  concentration distribution for Cases A4 and A5, taken as a horizontal slice through the model domain at  $z = 1.5$  m. For Case A4, hydrocarbon concentrations greater than 1 mg/L were observed to extend up to 25 m downgradient of the source area by 2000 days whereas, for Case A5, hydrocarbon concentrations greater than 1 mg/L extended less than 10 m downgradient of the source at 2000 days. Variation in interior hydrocarbon concentration distribution (and the total mass of hydrocarbon

biodegraded) was observed for different  $\text{Fe}^{3+}$  concentration distributions because the proximity of the source relative to high concentrations of  $\text{Fe}^{3+}$  was different for each  $\text{Fe}^{3+}$  distribution. A contour plot of the initial  $\text{Fe}^{3+}$  distributions for Case A4, provided as the middle left contour plot of Figure 12, shows that the initial  $\text{Fe}^{3+}$  concentrations in and immediately downgradient of the source area were consistently lower than the average concentration of  $100 \mu\text{g Fe}^{3+}/\text{g soil}$ . Thus, in locations where the hydrocarbon was located for the majority of the simulation (i.e. in and immediately downgradient of the source area), less  $\text{Fe}^{3+}$  was available for ferrogenic hydrocarbon biodegradation in Case A4 than was available for during the homogenous case, resulting in less hydrocarbon biodegradation over time. The final concentration distribution is also shown for Case A4 in Figure 12 (bottom left). From this plot, the area of  $\text{Fe}^{3+}$  depletion is observed to encompass an area nearly 4 m wide and 10 m long by 2000 days. Conversely, the randomly generated  $\text{Fe}^{3+}$  distribution for Case A5 (middle right contour plot in Figure 12) placed high concentrations of  $\text{Fe}^{3+}$  downgradient of the source area, which produced increased ferrogenic hydrocarbon biodegradation near the source. The  $\text{Fe}^{3+}$  distribution 2000 days into Case A5 is provided as the bottom right plot of Figure 12. The zone of  $\text{Fe}^{3+}$  depletion from Case A5 was notable smaller than that for Case A4, although mass calculations indicated that more  $\text{Fe}^{3+}$  was consumed during Case A5 than was consumed during Case A4.

### **Iron(III) Distribution Correlated to Hydraulic Conductivity**

For Case A6, the heterogeneous  $\text{Fe}^{3+}$  concentration distribution (mean =  $100 \mu\text{g Fe}^{3+}/\text{g}$ ,  $\sigma_{\text{InFe(III)}} = 0.5$ , horizontal correlation scale = 1.5 m) was specified as correlated to the hydraulic conductivity distribution. Figure 13 shows the 2000-day hydrocarbon, initial  $\text{Fe}^{3+}$ , and 2000-day  $\text{Fe}^{3+}$  concentration distribution along a horizontal slice of the model domain at  $z = 1.5 \text{ m}$ . The simulated hydrocarbon (top row, Figure 13) and oxygen (not shown) concentration distributions for Case A6 were nearly identical to the results from the base case (A1). As shown in the middle contour plot of Figure 13, the initial spatial distribution of  $\text{Fe}^{3+}$  for Case A6 placed lower than average  $\text{Fe}^{3+}$  concentrations in the source area, but higher than average  $\text{Fe}^{3+}$  concentrations immediately downgradient of the source area. As

shown in the bottom contour plot of Figure 13,  $\text{Fe}^{3+}$  depletion in the source area was nearly complete by 2000 days, and a finger of  $\text{Fe}^{3+}$  depletion was observed to extend approximately 10 m downgradient of the source by the end of the simulation. Mass loss calculations indicated that the mass of hydrocarbon biodegraded during Case A6 was consistently less than the hydrocarbon mass biodegraded in the base case (A1), although this difference was less than 5 percent at 2000 days.

### **Microbial Population Correlated to Hydraulic Conductivity**

For Case A7, both the aerobic and ferrogenic microbial populations were correlated to hydraulic conductivity to test how correlating microbial activity to zones of higher hydraulic conductivity affected model results. As shown in the left column of Figure 14, correlating microbial activity to hydraulic conductivity produced little deviation from the base case at 1000 days into the simulation. At 2000 days into the simulation, however, hydrocarbon concentrations greater than 10 mg/L have been nearly eliminated but the 1 mg/L contour of the hydrocarbon plume was observed to extend approximately 25 m downgradient from the source area.

An additional simulation was conducted with both the microbial populations and the  $\text{Fe}^{3+}$  distribution correlated to hydraulic conductivity (Case A8). The results from spatial moments calculations for Case A8 are provided along with results from the base case (A1), Case A6 ( $\text{Fe}^{3+}$  correlated to hydraulic conductivity), and Case A7 (microbial populations correlated to hydraulic conductivity) in Figure 15. As shown in Figure 15A, correlating either the  $\text{Fe}^{3+}$  distribution or the microbial population to hydraulic conductivity produced a decrease in the mass of hydrocarbon biodegraded, relative to the hydrocarbon mass biodegraded in the base case, after approximately 250 days into the simulation. Of the four cases presented in Figure 15A, Case A8 produced the least amount of hydrocarbon biodegradation. This result indicates that correlating both the microbial population and the  $\text{Fe}^{3+}$  distribution to hydraulic conductivity had an additive effect on hydrocarbon biodegradation. Figure 15B shows the results for center of mass calculations for the hydrocarbon plume in Cases A1, A6, A7, and A8. This figure shows that hydrocarbon center of mass was more sensitive to correlating the microbial population to hydraulic

conductivity than it was to correlating the  $\text{Fe}^{3+}$  distribution to hydraulic conductivity. Furthermore, specifying the microbial population as correlated to hydraulic conductivity caused the model to predict that the longitudinal hydrocarbon center of mass would migrate further from the source area than was observed for the hydrocarbon in the base case. Figure 15C depicts the longitudinal spatial standard deviation for the correlated cases (A6, A7, and A8) and the base case. As shown in Figure 15C, correlating the microbial population to the hydraulic conductivity resulted in less variation in the hydrocarbon plume in the longitudinal direction. This finding was consistent with the qualitative observation of the hydrocarbon in Case A7 in that the peak concentrations (greater than 10 mg/L) were observed to be degraded, while hydrocarbon concentrations greater than 1 mg/L were observed over much of the hydrocarbon plume. In effect, correlating the microbial population to hydraulic conductivity smoothed the hydrocarbon distribution by biodegrading peak concentrations to a greater extent than intermediate concentrations.

The results from this limited investigation indicate that using a heterogeneous initial condition for the starting microbial populations caused variation in the interior concentration distribution, but did not alter the overall plume dimensions. One reason that the heterogeneous microbial population had little impact on the hydrocarbon plume is that the numerical model implemented for this study accounts for microbial growth (and decay) in the presence (absence) of appropriate substrates and hydrocarbons. Since the yield coefficient for the aerobic population was a relatively high value, the model was able to ‘grow’ the aerobic population such that the overall plume dimensions were not affected by the heterogeneity in the initial condition. These results were interesting in that correlating the microbial population to hydraulic conductivity *decreased* the mass of biodegraded hydrocarbon for the chosen hydraulic conductivity distribution.

### **Sensitivity of Results to Hydraulic Conductivity Distribution**

Results shown thus far have been for a single hydraulic conductivity field. To illustrate the effects of varying the individual hydraulic conductivity field, a second hydraulic conductivity field of equal

statistical parameters to distribution A was developed using a different seed number in the turning bands program. Figure 16 depicts a horizontal and vertical slice of distribution B, which can be compared with Figure 2 to show that the individual hydraulic conductivity fields for distributions A and B were noticeably different. The following discussion is provided to illustrate how selected model output may vary between individual hydraulic conductivity realizations, and is not intended to serve as a surrogate for findings which may result from statistically analyzing a large number of simulations through heterogeneous flow fields generated using the statistical parameters contained in Table 1.

Solute concentration distributions are shown in Figure 17 for the conservative tracer (top row), the hydrocarbon subjected to aerobic biodegradation (Case B0, middle row), and the hydrocarbon subjected to sequential aerobic/ $\text{Fe}^{3+}$ -reducing biodegradation (Case B1, bottom row). As with simulations using hydraulic conductivity A, the inclusion of biodegradation in simulations using hydraulic conductivity B caused a decrease in concentration and overall extent of the hydrocarbon plume relative to the conservative tracer. Furthermore, addition of ferrogenic biodegradation caused hydrocarbon concentrations to decrease by an order of magnitude throughout the interior of the hydrocarbon plume relative to the aerobically biodegraded plume. Ferrogenic biodegradation also caused the sequentially biodegraded hydrocarbon plume to be smaller than the aerobically biodegraded hydrocarbon plume (as defined by the 0.001 mg/L contour).

As shown in Figure 18, the size and shape of the oxygen-depleted zones for Cases B0 and B1 were nearly identical in size to their corresponding hydrocarbon plumes, although the size of the oxygen-depleted zone for Case B1 was smaller than that for Case B0. As with simulations using hydraulic conductivity distribution A, the majority of  $\text{Fe}^{3+}$  consumption was simulated to occur in the source area prior to hydrocarbon migration downgradient.

Calculations for the mass of solute remaining in the domain and the location of the center of mass versus time are presented in Figures 19A and 19B, respectively, for the tracer and hydrocarbon from Cases B0, B1, B2, and B3. The results in Figure 19A indicate that aerobic biodegradation was able to

biodegrade approximately 37 percent of the hydrocarbon in 2000 days (Case B0), whereas the sequential biodegradation base case (B1) biodegraded over 98 percent of the hydrocarbon. Mass balance calculation by electron acceptor indicated that approximately 72 percent of the total hydrocarbon biodegraded during the length of the Case B1 simulation was due to ferrogenic biodegradation. Figure 19A also shows that decreasing the mass of bioavailable  $\text{Fe}^{3+}$  by 50 percent (Case B2) decreased the mass of hydrocarbon biodegraded, whereas increasing the mass of bioavailable  $\text{Fe}^{3+}$  by 50 percent (Case B3) had no significant impact on the mass of hydrocarbon biodegraded. Figure 19B indicates that the longitudinal center of mass of the hydrocarbon plumes subjected to sequential biodegradation were, in all cases, greater than the center of mass of the tracer. The center of mass for the aerobically biodegraded hydrocarbon and the tracer were nearly identical during the entire 2000-day simulation for Case B0. Furthermore, increasing the mass of bioavailable  $\text{Fe}^{3+}$  caused the center of mass of the hydrocarbon plume to move increasingly further downgradient. This finding was the opposite of the results for the longitudinal center of mass using hydraulic conductivity distribution A (Figure 6A), in that increasing the mass of available electron acceptor produced a decrease in downgradient migration of the longitudinal center of mass. Although the rapid increase in the center of mass location for the hydrocarbon in Cases B1 and B3 after approximately 1700 days into the simulation was likely an anomaly produced by the low hydrocarbon mass (and concentrations) remaining in the domain in the last 300 days of the simulation, the observation that the hydrocarbon center of mass was greater than that of the tracer for Case B2 and the earlier times of Cases B1 and B3 could not be ignored. This result was believed to occur for hydrocarbon migration through hydraulic conductivity distribution B due to local variations in the flow field that produced increased spreading of the hydrocarbon plume and resulted in increased mixing between the hydrocarbon and aqueous phase oxygen at the plume edges. The combination of increased aerobic biodegradation along the lateral edges of the plume and both aerobic and ferrogenic biodegradation in the back half of the plume may have caused the center of mass in the hydrocarbon plume to shift forward relative to the tracer.

The final initial  $\text{Fe}^{3+}$  condition examined for the second heterogeneous flow field was to correlate  $\text{Fe}^{3+}$  concentration to hydraulic conductivity distribution B, as was done in Case A6. Correlating  $\text{Fe}^{3+}$  concentration to hydraulic conductivity distribution B produced a slight *increase* (less than 0.5 percent at 2000 days) in the mass of biodegraded hydrocarbon. This result was the opposite effect of correlating  $\text{Fe}^{3+}$  to distribution A, when correlating  $\text{Fe}^{3+}$  concentration to hydraulic conductivity distribution A was observed to decrease the mass of hydrocarbon biodegraded. Although correlating the hydraulic conductivity and  $\text{Fe}^{3+}$  concentration distribution was expected to consistently enhance hydrocarbon biodegradation, the fact that the source was located in a relatively low hydraulic conductivity zone in distribution A resulted in less than an average mass of bioavailable  $\text{Fe}^{3+}$  in and around the source and, consequently, less ferrogenic biodegradation. The converse was true for correlating  $\text{Fe}^{3+}$  concentration to hydraulic conductivity distribution B, as the concentration of  $\text{Fe}^{3+}$  in and around the source area for this case was greater than the mean concentration, thereby producing increased ferrogenic (and total) biodegradation. These results indicate that correlating hydraulic conductivity to  $\text{Fe}^{3+}$  distribution does not produce a consistent increase or decrease in hydrocarbon biodegradation. Furthermore, these results indicate that, for the statistical parameters investigated in this study, correlating  $\text{Fe}^{3+}$  distribution to hydraulic conductivity did not have a significant impact on simulated mass versus time or hydrocarbon concentration distribution for either hydraulic conductivity realization.

## Summary and Conclusions

The results from this numerical experiment on hydrocarbon natural attenuation in a hypothetical, heterogeneous aquifer system demonstrate that, when compared to a hydrocarbon plume biodegraded solely under aerobic conditions, the addition of ferrogenic biodegradation caused an increase in the mass of hydrocarbon biodegraded, a reduction in peak hydrocarbon concentrations, an alteration in the location of the hydrocarbon center of mass, and a reduction longitudinal spreading of the hydrocarbon plume. For starting  $\text{Fe}^{3+}$  concentrations between 50 and 150  $\mu\text{g Fe}^{3+}/\text{g soil}$ , ferrogenic biodegradation was observed to be the dominant biodegradation process in terms of hydrocarbon mass removal by 200 days after

contaminant release. Although the inclusion of ferrogenic biodegradation was not shown to significantly impact longitudinal spreading of the hypothetical hydrocarbon plume (defined by a 0.001 mg/L contour), ferrogenic biodegradation was observed to reduce hydrocarbon concentrations in the interior of the hydrocarbon plume by as much as an order of magnitude relative to concentrations predicted for a hydrocarbon plume subjected solely to aerobic biodegradation. Changes in hydrocarbon concentration were found to be dependent on the starting concentration of  $\text{Fe}^{3+}$ , as simulations using a 50  $\mu\text{g Fe}^{3+}/\text{g}$  soil initial  $\text{Fe}^{3+}$  were observed to be electron acceptor limited in and around the source area. This result indicates that explicitly simulating  $\text{Fe}^{3+}$  utilization during ferrogenic biodegradation allowed the model to account for electron acceptor limited conditions, an effect which can not be simulated using constant rate biodegradation models.

Spatial moments calculations for the location of the longitudinal center of mass indicated that the local hydraulic conductivity distribution determined whether the center of mass of the hydrocarbon plume would move further downgradient than the tracer. This result was different from the conclusions drawn by MacQuarrie and Sudicky (1990), which suggested that the location of the center of mass for a biodegrading hydrocarbon plume will consistently be located downgradient of the center of mass of a conservative tracer plume in heterogeneous flow fields. The primary differences between these studies was that the current study simulated a non-sorbing hydrocarbon with biodegradation under two, sequential biodegradation processes (one of which was solid phase electron acceptor), whereas MacQuarrie and Sudicky (1990) simulated a sorbing hydrocarbon subjected only to aerobic biodegradation. Further study is needed to determine whether any conclusions can be drawn in terms of the location of the center of mass for a biodegradable hydrocarbon plume relative to the center of mass for a conservative tracer of equal initial starting concentration.

Results from simulations using random heterogeneous  $\text{Fe}^{3+}$  concentration distributions of equal mean concentration indicated that hydrocarbon biodegradation increased, relative to the homogeneous  $\text{Fe}^{3+}$  case, when high  $\text{Fe}^{3+}$  concentrations were found in and immediately downgradient of the source area.

Correlating either the starting  $\text{Fe}^{3+}$  concentration distribution or the microbial population to hydraulic conductivity was not found to consistently increase or decrease the mass of biodegraded hydrocarbon for the hypothetical model used in this study.

The finding that the initial  $\text{Fe}^{3+}$  concentration has a major influence on mass of biodegraded hydrocarbon is of significance, as future inclusion of ferrogenic biodegradation during MNA site-assessment may lead to justifiably smaller estimates for the time to remediation of petroleum hydrocarbon contaminated sites where MNA is applied. Furthermore, the finding that hydrocarbon concentrations may be decreased by an order of magnitude or more due to the presence of ferrogenic activity may increase the number of sites where MNA may be deemed an acceptable alternative in terms of meeting maximum concentration objectives.

Additional investigation is needed to extend the methodology used in this work to include a wider variety of source conditions and natural attenuation processes. For example, the influence of using various source configurations, such as constant concentration, pulsed, or rate-limited NAPL release, on model results needs to be investigated. Furthermore, the influence of sorption on model results should be investigated, as the majority of petroleum hydrocarbons of environmental and health concern are hydrophobic. Variation in the model input microbial parameters and their distribution is merited, as selection of these parameters may ultimately control the range of possible solutions for a given hydrocarbon release. Finally, this work suggests that accurate estimates for the mass of bioavailable  $\text{Fe}^{3+}$  immediately downgradient of contaminant spills may be critical in determining future contaminant migration if the contaminant can be shown to biodegrade under ferrogenic conditions.

## Acknowledgements

Financial support for this work was provided by the Via Foundation of the Charles Edward Via, Jr. Department of Civil and Environmental Engineering at Virginia Polytechnic Institute and State University. Deep appreciation is extended to Dr. Dan W. Waddill for his work on developing the mass tracking algorithms in the SEAM3D code that made this work possible.

**Table 1. Statistical parameters for the hypothetical hydraulic conductivity field, as reported for a sandy loam soil by Carsel and Parrish (1988).**

Hydraulic Conductivity Distribution Parameter	Value
<i>Distribution</i>	Log-normal
<i>Mean</i>	1.0 m/d
<i>Standard Deviation</i>	1.0
<i>Horizontal Correlation Scale</i>	1.5m
<i>Vertical Correlation Scale</i>	0.15m

Table 2. Solute transport parameters for the hypothetical transport model.

Solute Transport Parameter	Value
Dispersivity	
<i>Longitudinal</i>	0.01m
<i>Transverse</i>	0.001m
<i>Vertical</i>	0.0001m
Porosity	0.35
Bulk Density	$1.6 \times 10^6 \text{ g/m}^3$

Table 3. Biodegradation parameters for the hypothetical reactive solute transport model.

Biodegradation Parameter	Primary Electron Acceptor (Oxygen)	Terminal Electron Acceptor (Iron(III))
Maximum Substrate Utilization Rate ( $d^{-1}$ )	1.0	0.1
Substrate Half Saturation Constant ( $mg_S/L$ )	5.0	5.0
Electron Acceptor Half Saturation Constant ( $mg_{EA}/L$ )	0.5	n/a
Initial Biomass ( $g_{bio}/m^3$ )	0.1 <sup>*</sup>	0.01 <sup>*</sup>
Microbial Yield Coefficient ( $mg_S/mg_{bio}$ )	0.5	0.2
Electron Acceptor Use Coefficient ( $mg_{EA}/mg_S$ )	3.2	42.0
Inhibition Coefficient ( $mg_{O_2}/L$ )	n/a	0.10

\* Represents the mean starting concentration for simulations where the microbial population was heterogeneously distributed.

Table 4. Designations used to identify assumptions for a given simulation. For example, Case A3 was a simulation using hydraulic conductivity distribution ‘A’ and a heterogeneous iron(III) distribution of 150  $\mu\text{g Fe}^{3+}/\text{g}$  soil.

Designation	Description
A	Hydraulic conductivity distribution ‘A’
B	Hydraulic conductivity distribution ‘B’
0	No iron(III) biodegradation simulated (Aerobic Only)
1	Homogeneous $\text{Fe}^{3+}$ distribution of 100 $\mu\text{g/g}$
2	Homogeneous $\text{Fe}^{3+}$ distribution of 50 $\mu\text{g/g}$
3	Homogeneous $\text{Fe}^{3+}$ distribution of 150 $\mu\text{g/g}$
4	Random $\text{Fe}^{3+}$ distrib. with low $\text{Fe}^{3+}$ concentrations near the source
5	Random $\text{Fe}^{3+}$ distrib. with high $\text{Fe}^{3+}$ concentrations near the source
6	$\text{Fe}^{3+}$ distribution correlated to hydraulic conductivity
7	Microbial population correlated to hydraulic conductivity
8	Both $\text{Fe}^{3+}$ distribution and microbial population correlated to hydraulic conductivity

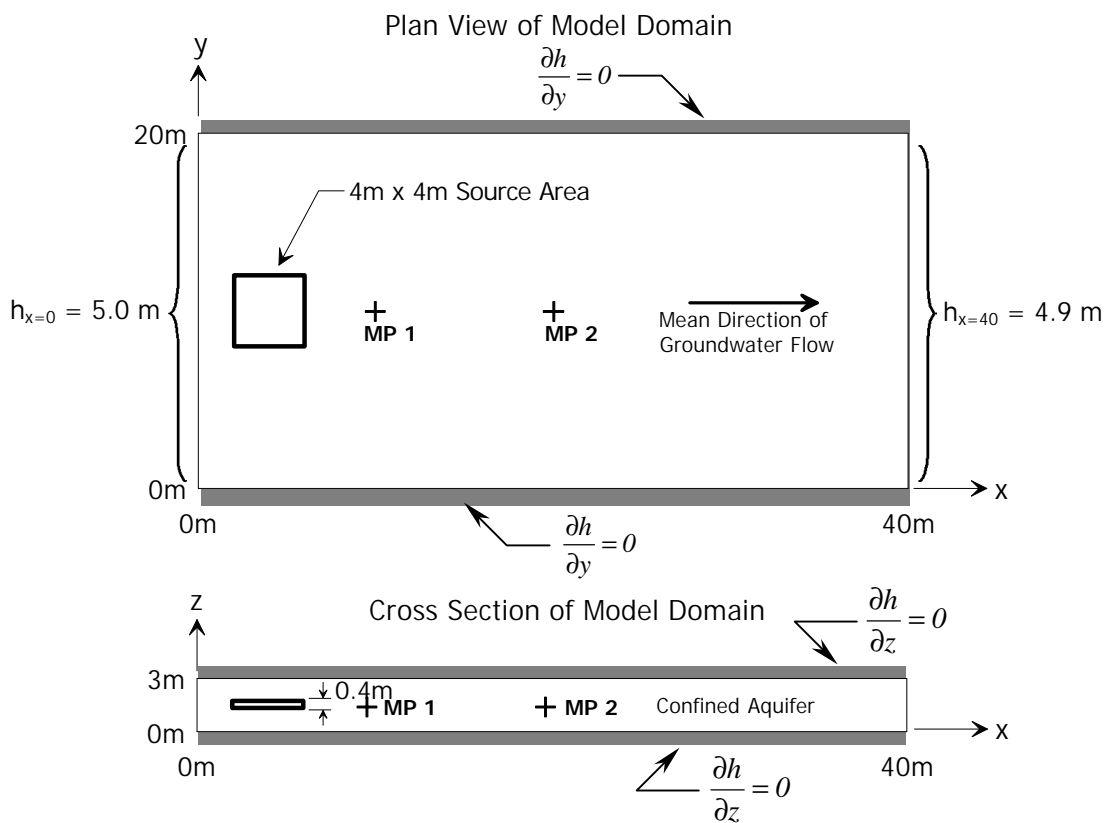


Figure 1. Boundary conditions and dimensions for the hypothetical numerical model domain.

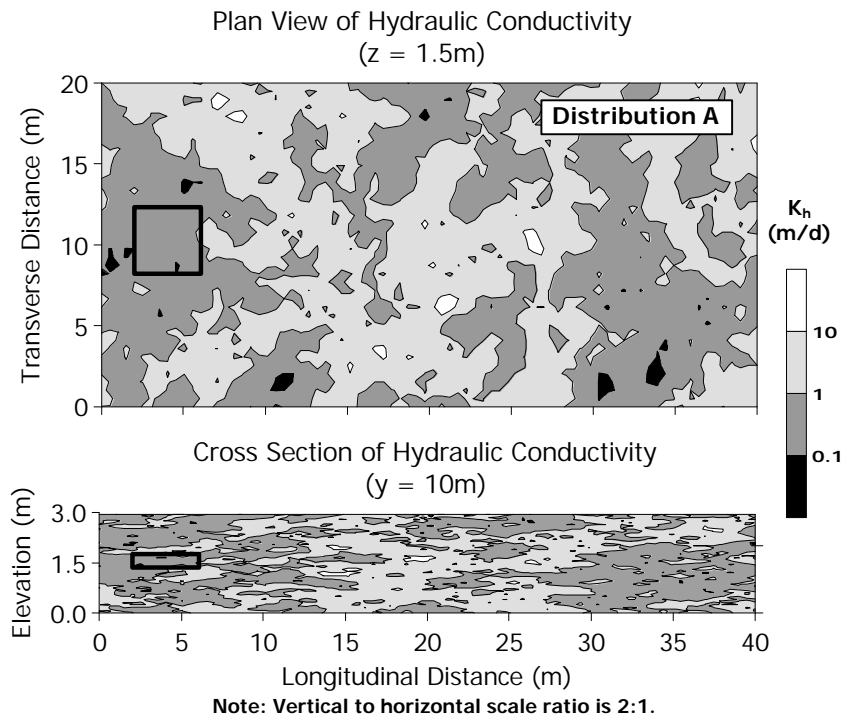


Figure 2. Cross sections of hydraulic conductivity distribution 'A', taken through the vertical ( $z = 1.5\text{ m}$ ) and horizontal ( $y = 10\text{ m}$ ) centerlines of the model domain.

CASE A0

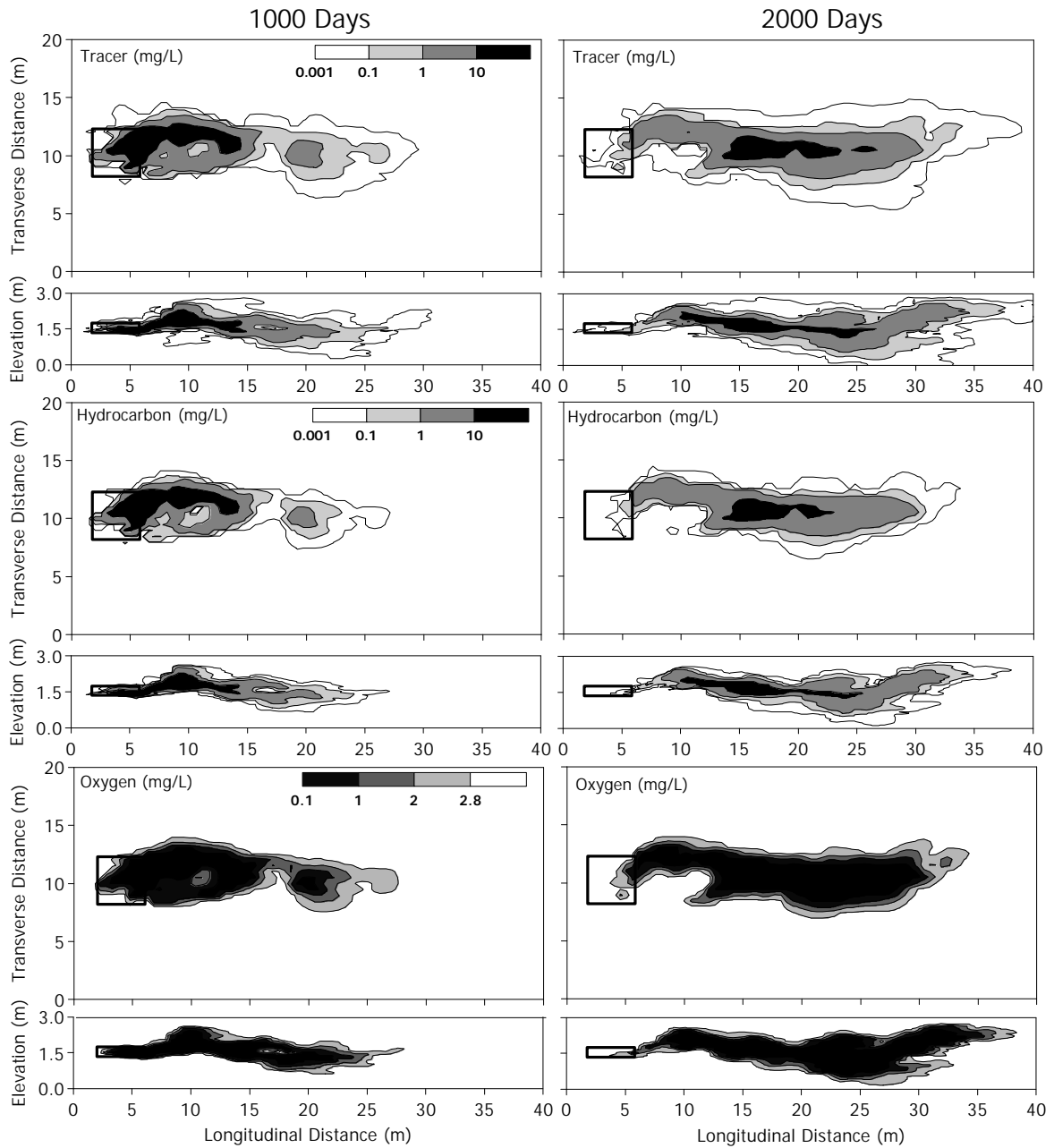
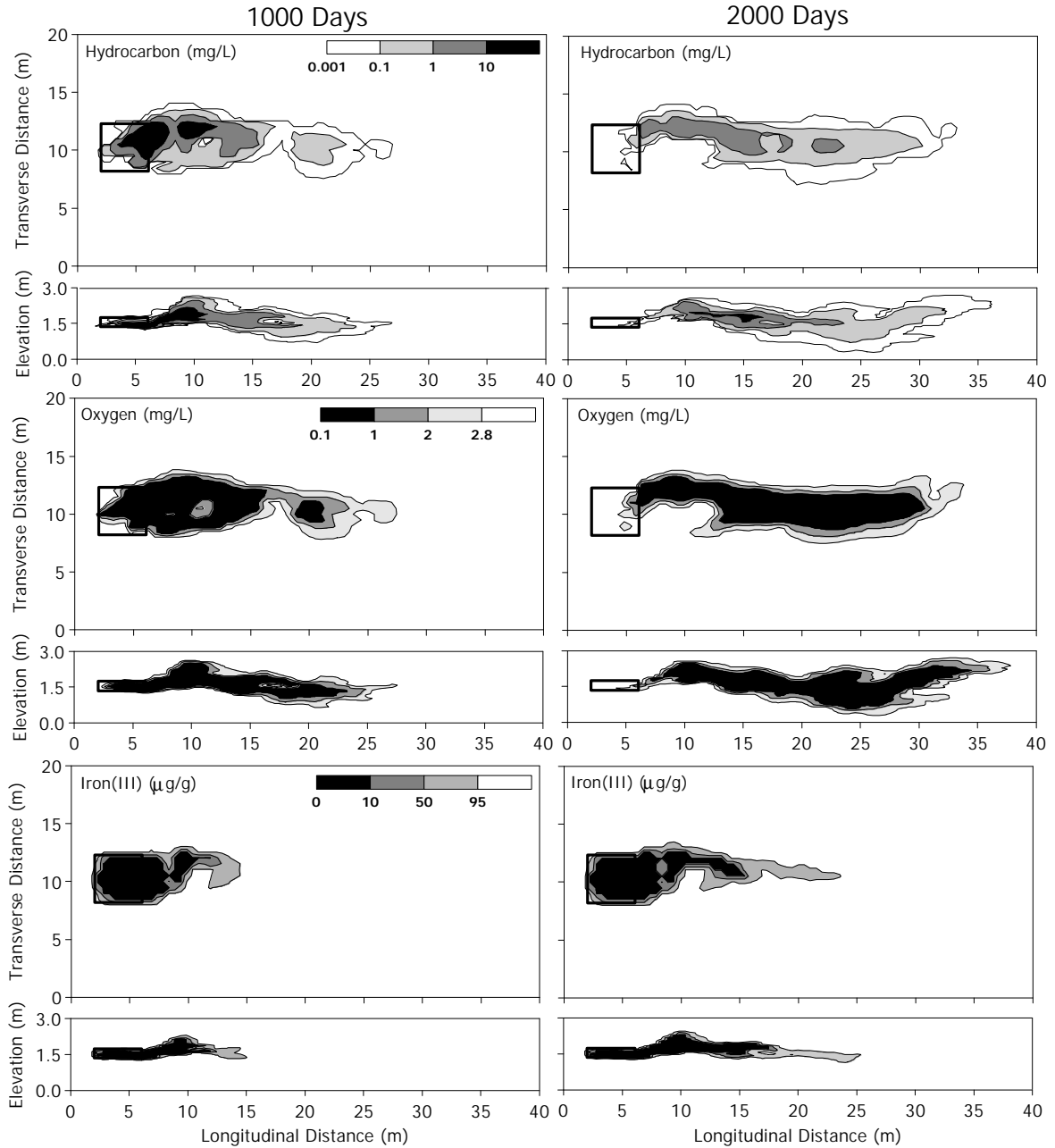


Figure 3. Horizontal and vertical cross sections through the centerline of the model domain depicting tracer (top row), hydrocarbon (middle row) and oxygen distributions (bottom row) for Case A0, taken at 1000 (left column) and 2000 (right column) days into the simulation. Hydrocarbon biodegradation for Case A0 was simulated under aerobic conditions.

BASE CASE A1



Note: Vertical to horizontal scale ratio is 2:1.

Figure 4. Horizontal and vertical cross sections through the centerline of the model domain depicting hydrocarbon (top row), oxygen (middle row), and  $\text{Fe}^{3+}$  distribution (bottom row) for Case A1, taken at 1000 (left column) and 2000 (right column) days into the simulation. Hydrocarbon biodegradation in Case A1 was simulated under sequential aerobic/ $\text{Fe}^{3+}$ -reducing conditions for a uniform initial  $\text{Fe}^{3+}$  concentration of  $100 \mu\text{g Fe}^{3+}/\text{g soil}$ .

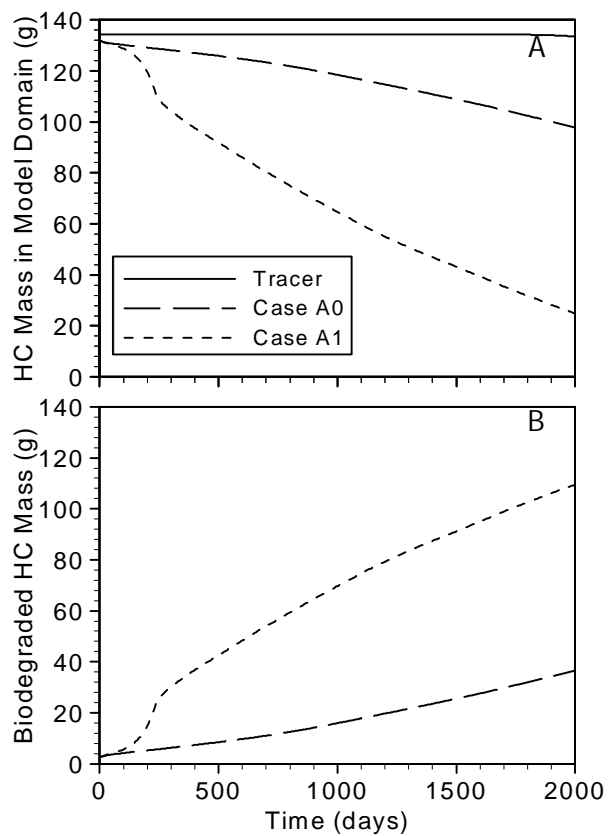


Figure 5. Tracer and hydrocarbon mass remaining in the model domain (A) and cumulative hydrocarbon mass biodegraded (B) as a function of time for model Cases A0 and A1.

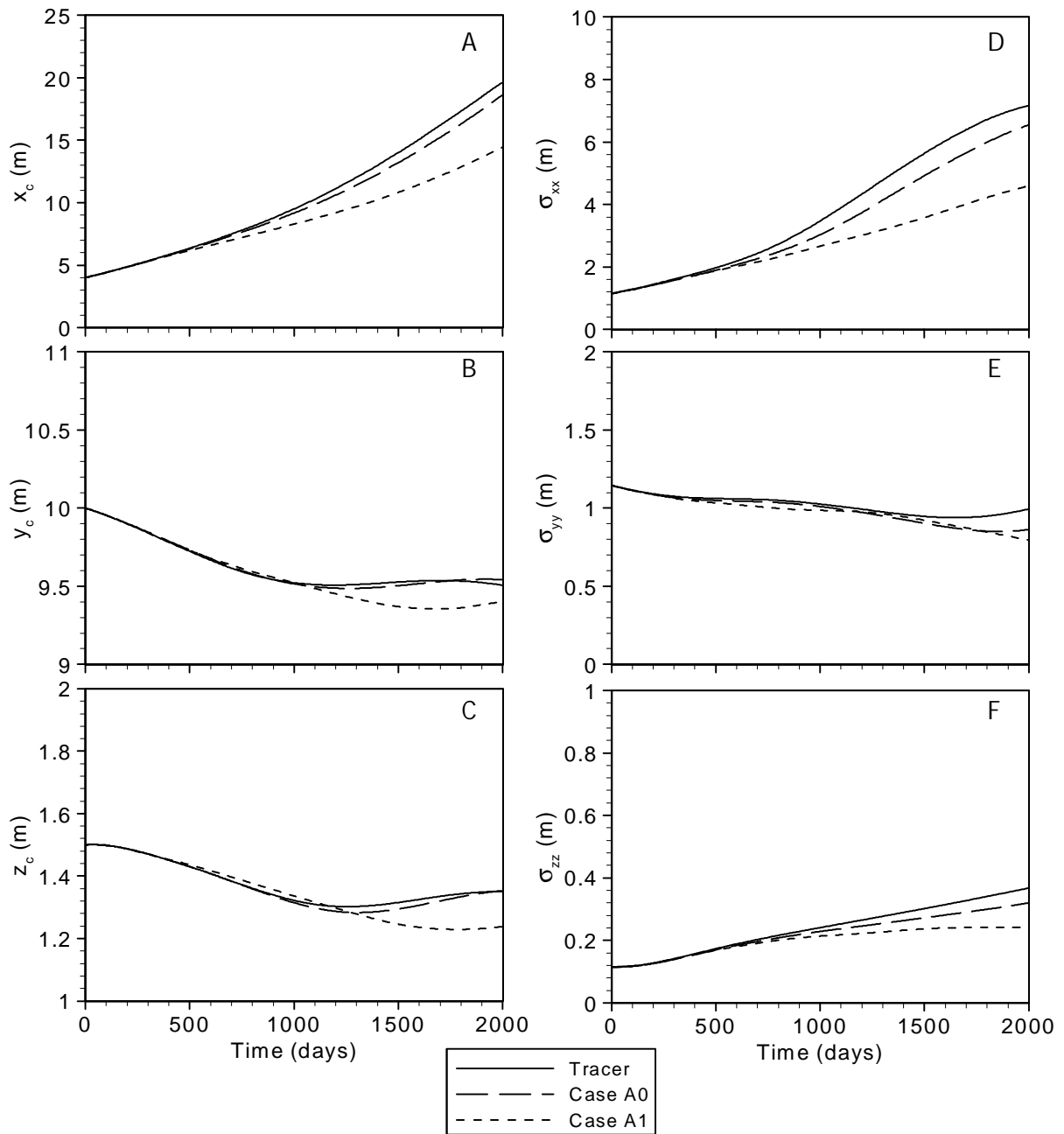


Figure 6. Spatial moments versus time for the centroid (left column) and spatial standard deviation (right column) in the longitudinal (x), transverse (y), and vertical (z) directions for the tracer, aerobically biodegraded hydrocarbon (A0), and sequentially biodegraded hydrocarbon (A1).

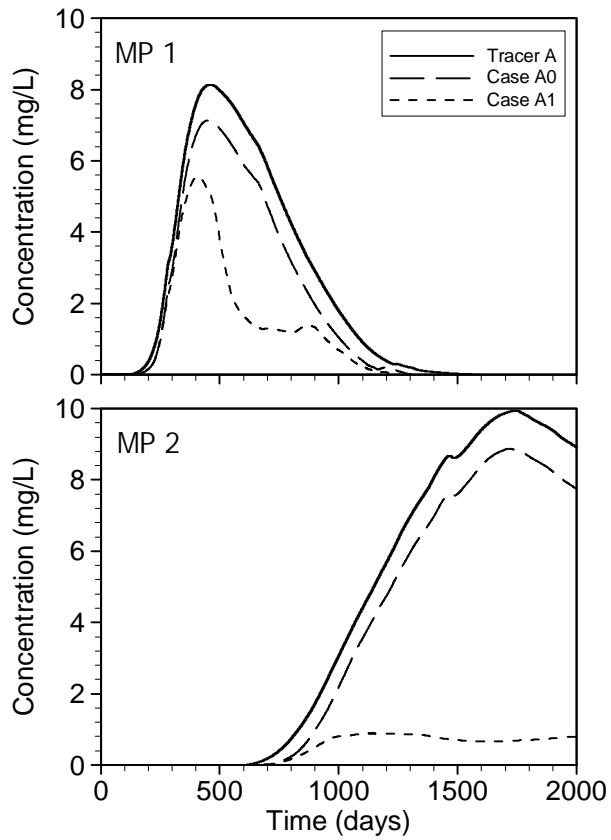


Figure 7. Tracer and hydrocarbon breakthrough curves at hypothetical monitoring points MP1 and MP2 for the aerobic only (A0) and sequential aerobic/ferrogenic (A1) biodegradation cases.

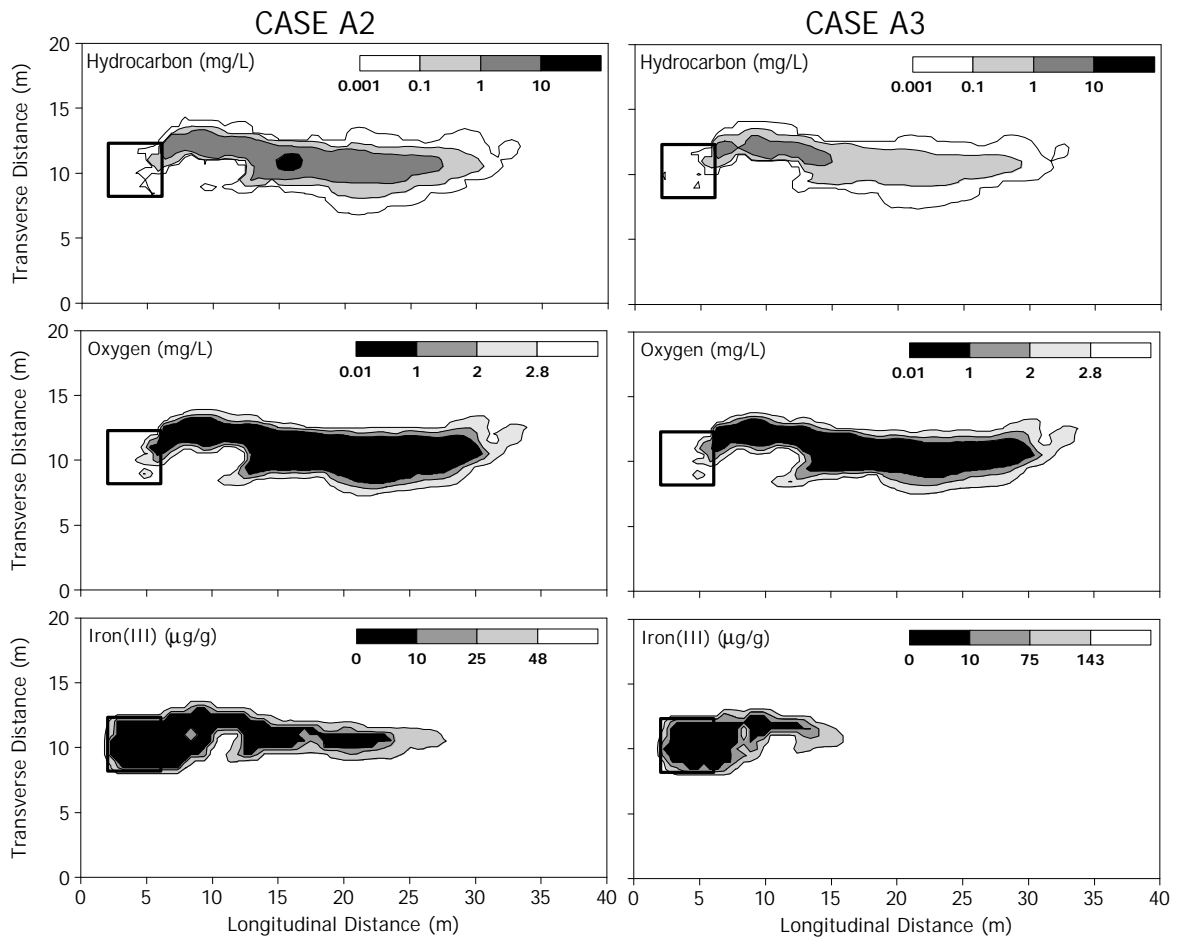


Figure 8. Horizontal hydrocarbon and electron acceptor distributions at  $z = 1.5$  m and 2000 days for Case A2 (left column,  $[\text{Fe}^{3+}] = 50 \mu\text{g Fe}^{3+}/\text{g soil}$ ) and Case A3 (right column,  $[\text{Fe}^{3+}] = 150 \mu\text{g Fe}^{3+}/\text{g soil}$ ).

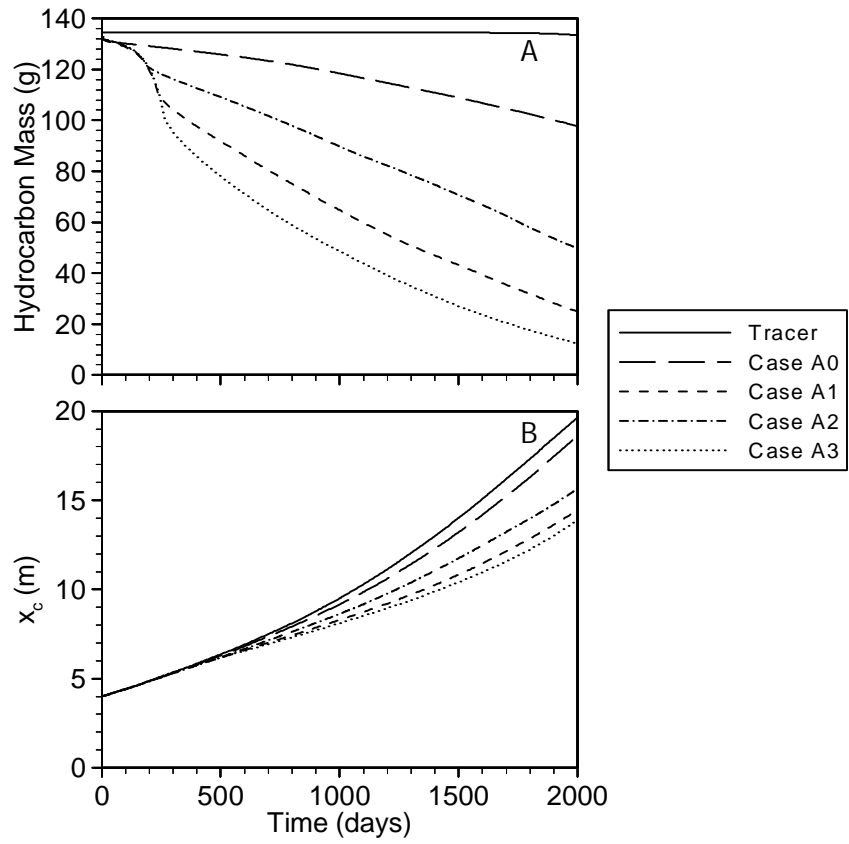


Figure 9. Tracer and hydrocarbon mass remaining in the model domain (A) and location of the longitudinal center of mass (B) versus time for Cases A0 through A3.

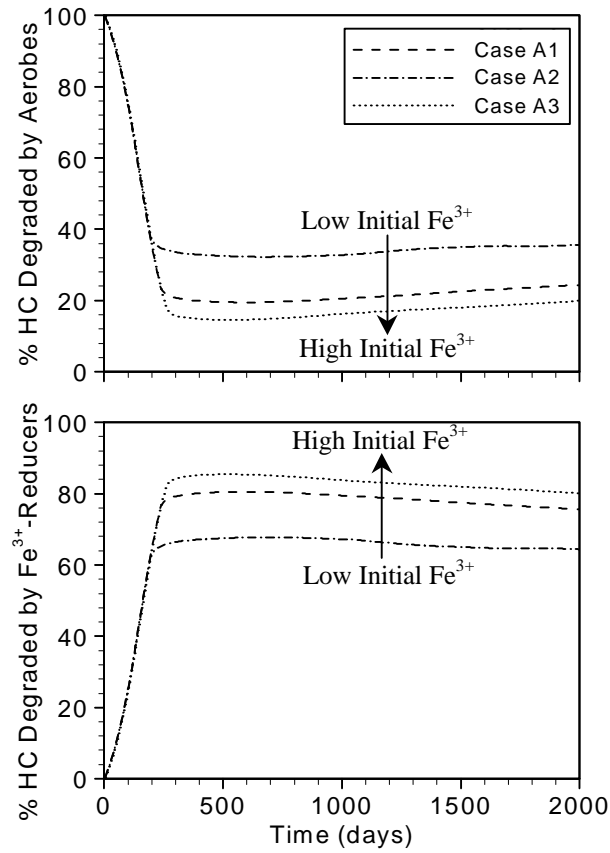


Figure 10. Percentage of hydrocarbon biodegraded by each electron acceptor process.

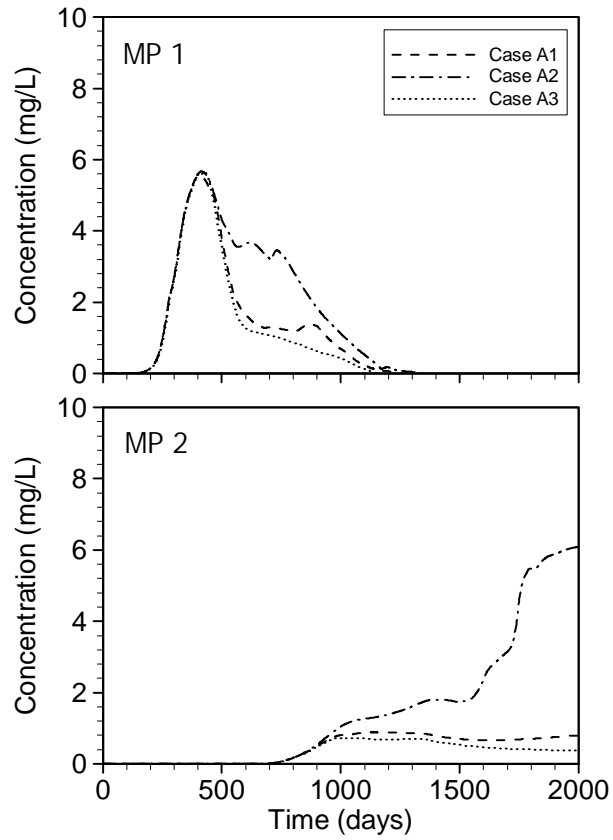


Figure 11. Hydrocarbon breakthrough curves at hypothetical monitoring points MP1 and MP2 for initial  $\text{Fe}^{3+}$  concentrations of  $50 \mu\text{g Fe}^{3+}/\text{g soil}$  (Case A2),  $100 \mu\text{g Fe}^{3+}/\text{g soil}$  (Case A1), and  $150 \mu\text{g Fe}^{3+}/\text{g soil}$  (Case A3).

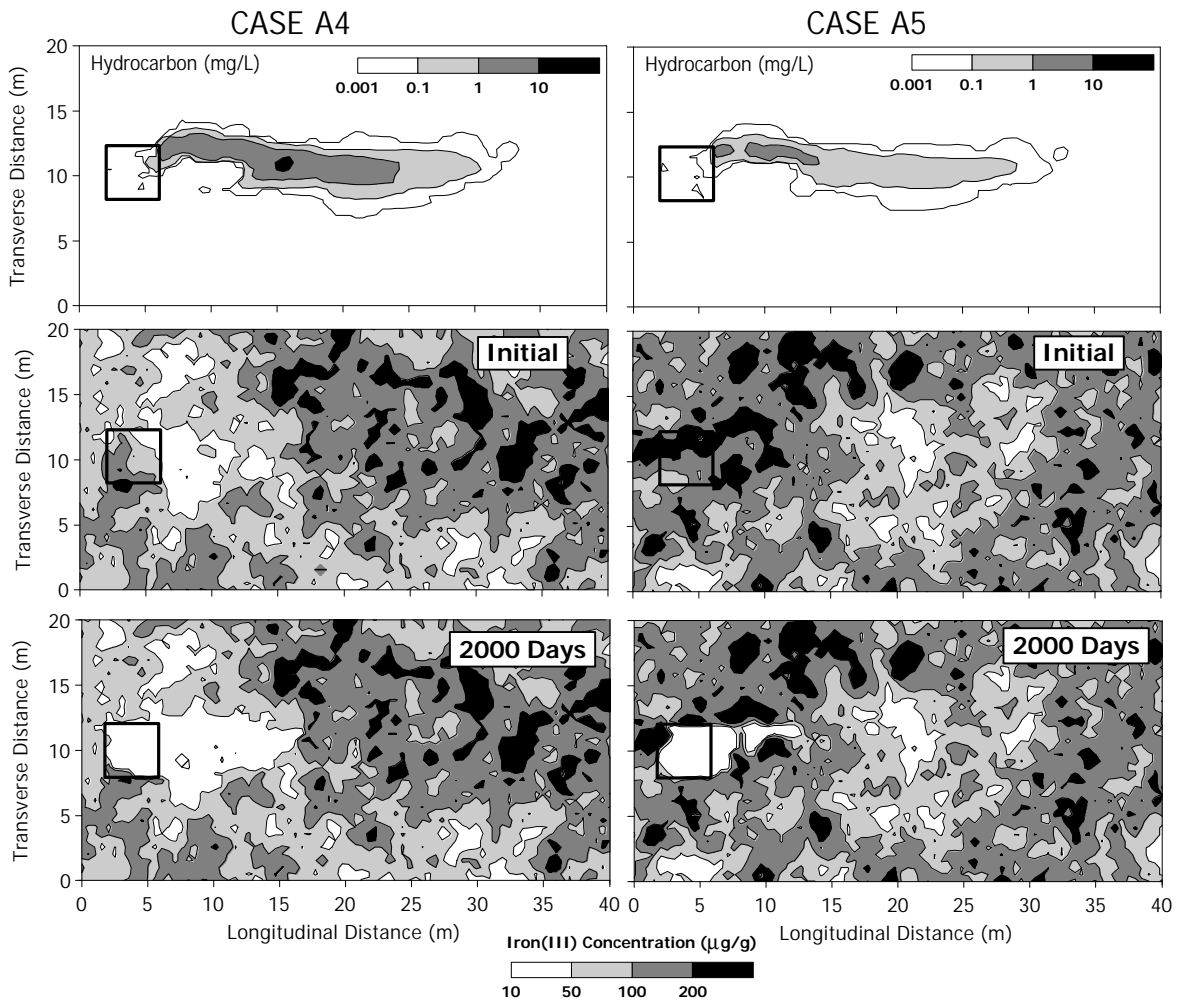


Figure 12. Hydrocarbon (top), initial Fe<sup>3+</sup> (middle), and 2000 day Fe<sup>3+</sup> (bottom) concentrations at z = 1.5 m and 2000 days for Cases A4 (left) and Case A5 (right).

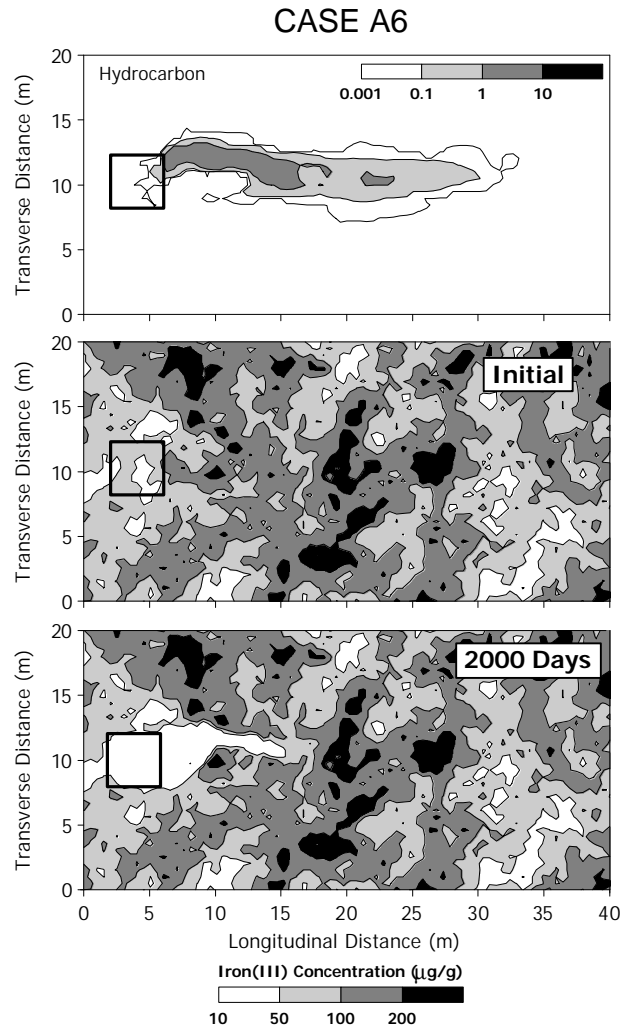


Figure 13. Hydrocarbon (top), initial  $\text{Fe}^{3+}$  (middle), and 2000-day  $\text{Fe}^{3+}$  (bottom) concentration distributions at  $z = 1.5$  m for simulations using an initial  $\text{Fe}^{3+}$  concentration distribution that was correlated to hydraulic conductivity (Case A6).

CASE A7

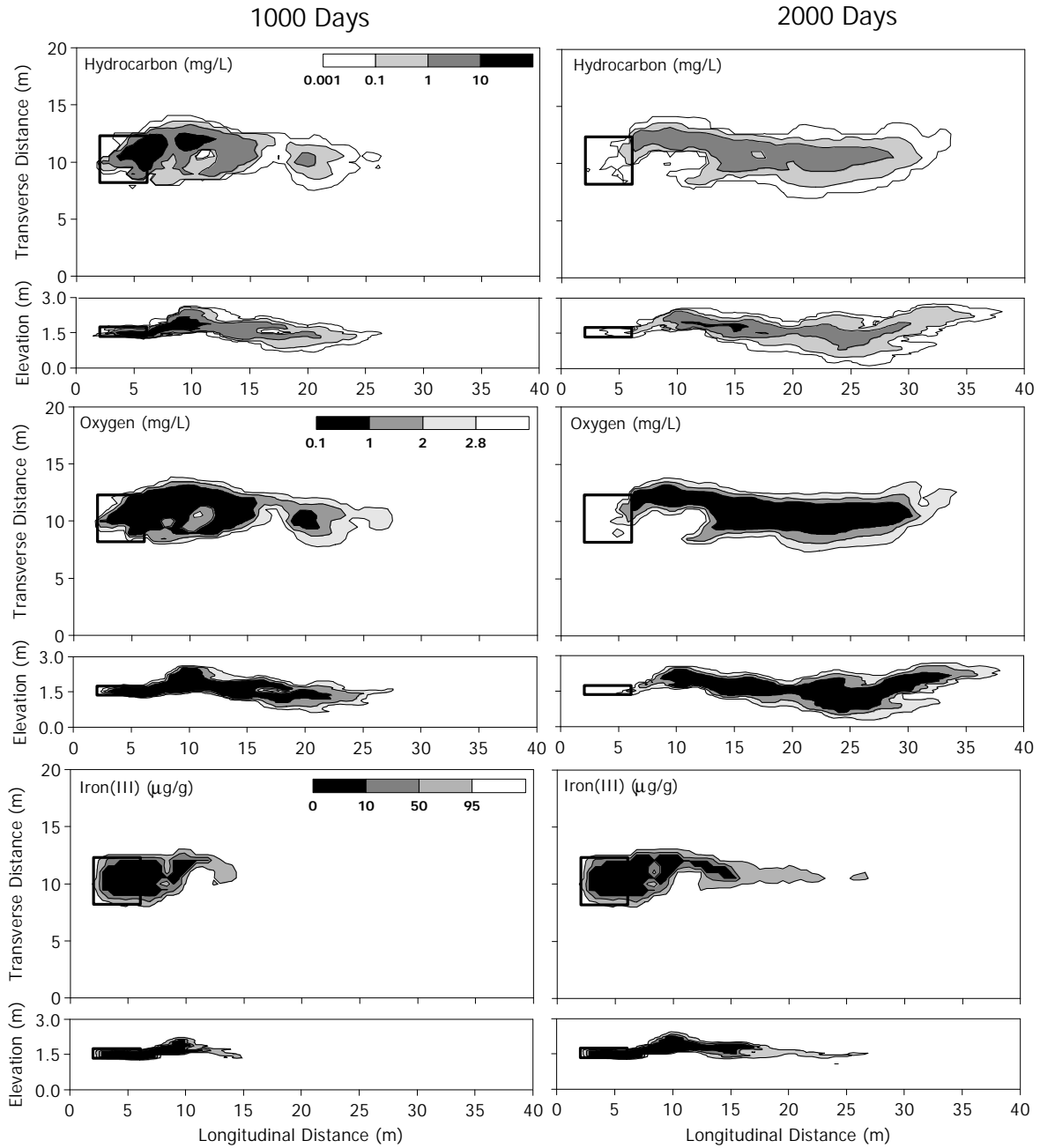


Figure 14. Hydrocarbon (top) and oxygen (bottom) concentration distributions for simulations using microbial population distributions that are correlated to hydraulic conductivity at 1000 days (left) and 2000 days (right) into simulation A7.

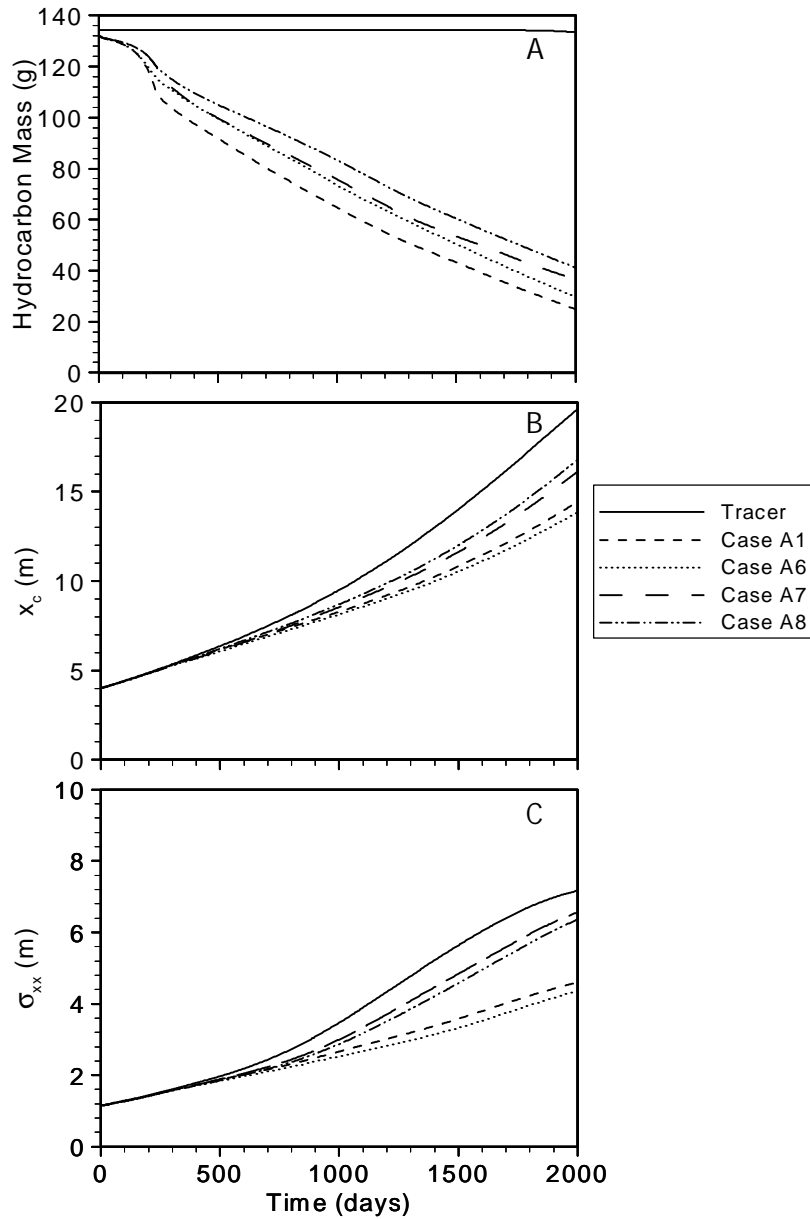


Figure 15. Longitudinal spatial moments calculations for the tracer and hydrocarbon of Cases A1, A6, A7, and A8 when either the  $\text{Fe}^{3+}$  concentration (A6), the microbial populations (A7), or both (A8) are correlated to hydraulic conductivity distribution A.

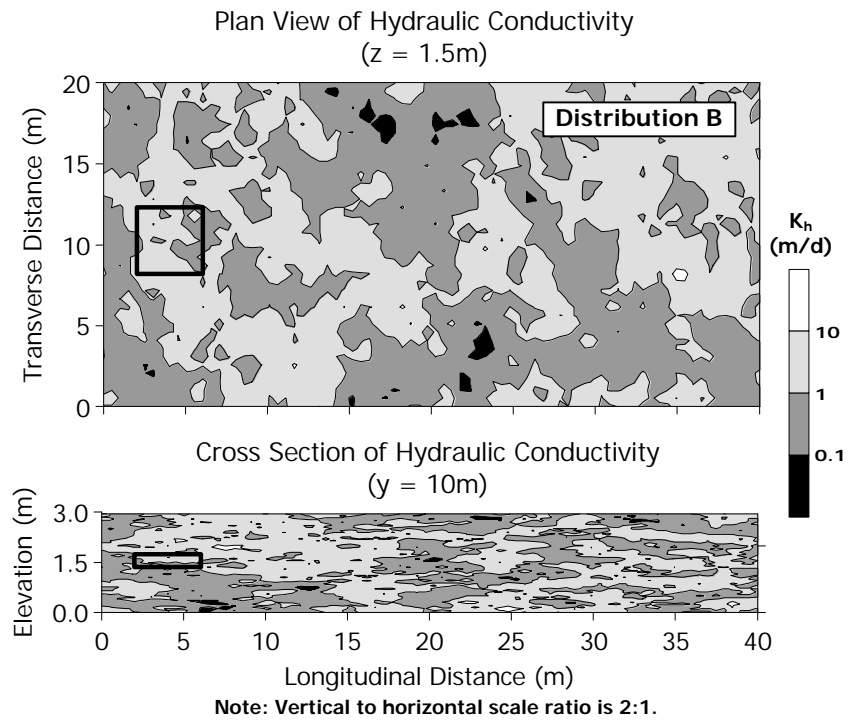


Figure 16. Cross sections of hydraulic conductivity distribution 'B', taken through the vertical ( $z = 1.5\text{ m}$ ) and horizontal ( $y = 10\text{ m}$ ) centerlines of the model domain.

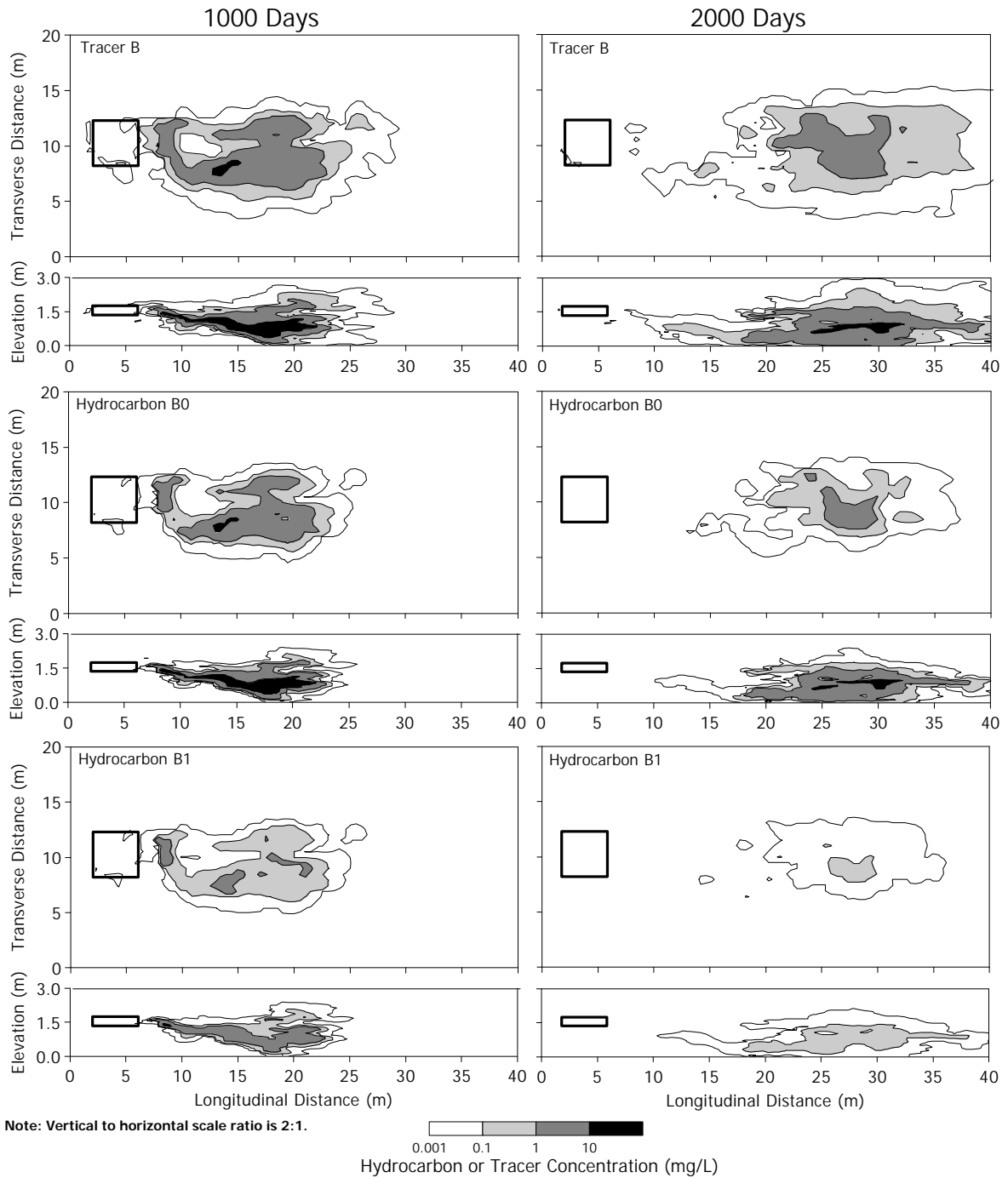


Figure 17. Horizontal and vertical cross sections through the centerline of the model domain depicting tracer (top row) and hydrocarbon distribution for Cases B0 (middle row) and B1 (bottom row), taken at 1000 (left column) and 2000 (right column) days into the simulation. Hydrocarbon biodegradation was simulated under aerobic conditions for Case B0 and under sequential aerobic/ $\text{Fe}^{3+}$ -reducing conditions for Case B1.

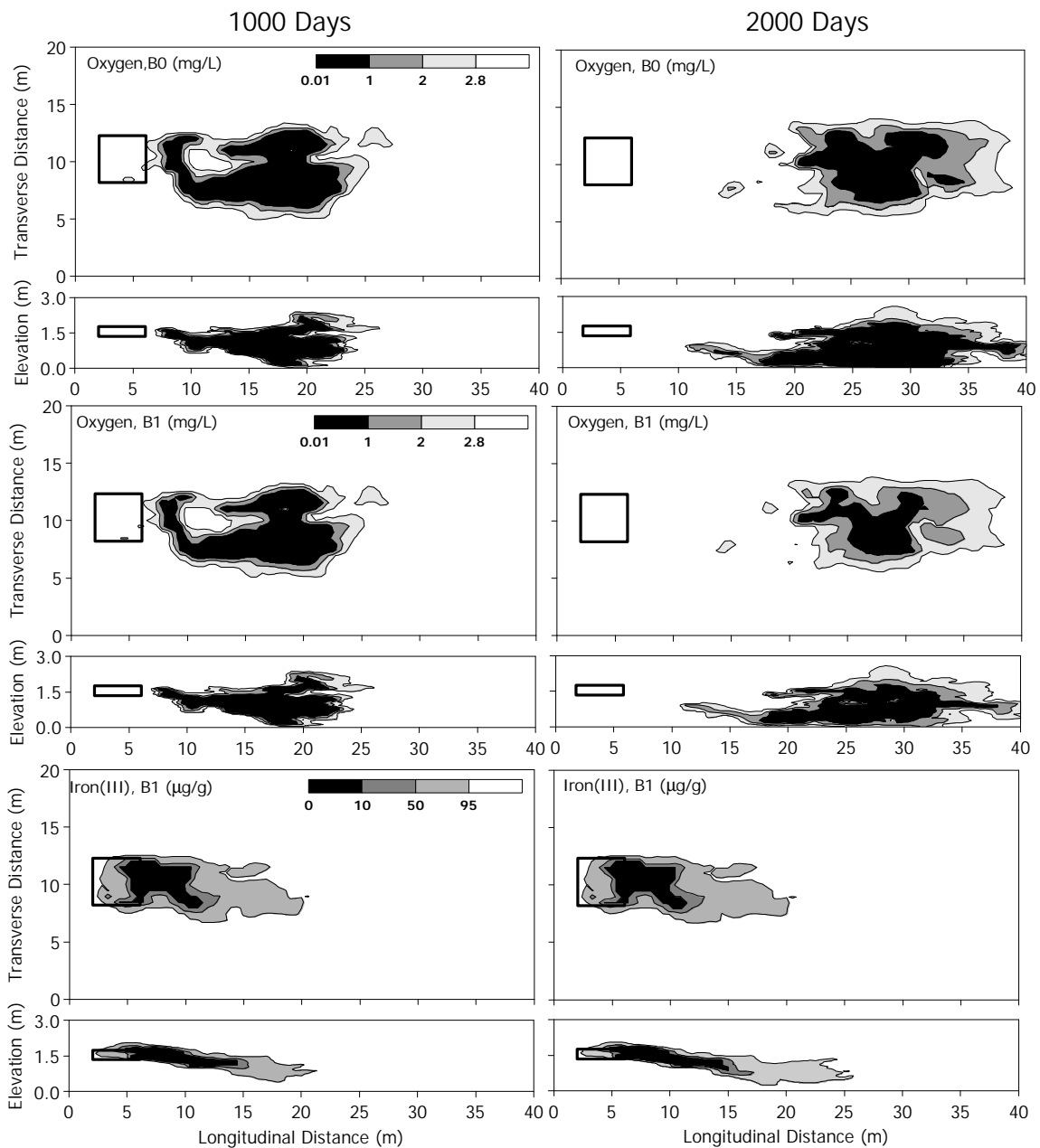


Figure 18. Horizontal and vertical cross sections through the centerline of the model domain depicting oxygen for Cases B0 (top row) and B1 (middle row) and  $\text{Fe}^{3+}$  for Case B1 (bottom row), taken at 1000 (left column) and 2000 (right column) days into the simulation. Hydrocarbon biodegradation was simulated under aerobic conditions for Case B0 and under sequential aerobic/ $\text{Fe}^{3+}$ -reducing conditions for Case B1.

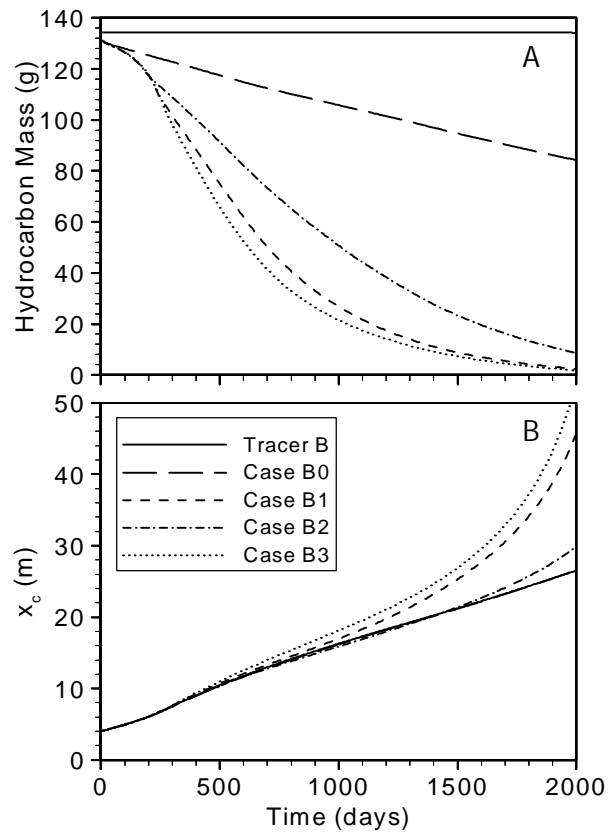


Figure 19. Method of moments calculations for the hydrocarbon mass remaining in the model domain (A) and the location of the longitudinal centroid,  $x_c$  (B) as a function of time for model simulations through hydraulic conductivity field 'B'.

## References

- Ababou, R. 1988. Three-dimensional flow in random porous media. *Ph.D. Thesis*. Mass. Inst. of Technol, Cambridge, MA.
- Aelion, C.M. and S.C. Long. 1994. Heterogeneity in contaminant concentration and microbial activity in subsurface sediments. In: *Hydrocarbon Bioremediation*, R.E. Hinchee, B.C. Alleman, R.E. Hoepfel, and R.N. Miller, Eds. Lewis Publishers, Boca Raton, FL. pp.192-200.
- Aris, R. 1956. On the dispersion of a solute in a fluid through a tube. *Proc. R. Soc. London, Ser. A*. 235:67-78.
- Brauner, J.S. and M.A. Widdowson. 2000. Numerical simulation of a natural attenuation experiment with a NAPL source: Contaminant dissolution and reactive transport. *In review*.
- Carsel, R.F. and R.S. Parrish. 1988. Developing joint probability distributions of soil water retention characteristics. *Water Resour. Res.* 24():755-769.
- Chao, T.T. and L. Zhou. 1983. Extraction techniques for selective dissolution of amorphous iron oxides from soils and sediments. *Soil Sci. Soc. Am. J.* 47:225-232.
- Chapelle, F.H. and P.M. Bradley. 1998. Selecting remediation goals by assessing the natural attenuation capacity of groundwater systems. *Bioremediation J.* 2(3-4):227-238.
- Chapelle, F.H. and D.R. Lovley. 1990. Rates of microbial metabolism in deep coastal plain aquifers. *Appl. Environ. Microbiol.* 56(6):1865-1874.
- Kennedy, L.G., J.W. Everett, T. Dewers, W. Pickens, and D. Edwards. 1999. Application of mineral iron and sulfide analysis to evaluate natural attenuation at fuel contaminated site. *J. Environ. Engr.* 125(1):47-56.
- Konopka, A. and R. Turco. 1991. Biodegradation of organic compounds in vadose zone and aquifer sediments. *Appl. Environ. Microbiol.* 57(8):2260-2268.
- Libelo, E.L., T.B. Stauffer, M.A. Greer, W.G. MacIntyre, and J.M. Boggs. 1997. A field study to elucidate processes involved in natural attenuation. In: *In-situ and On Site Bioremediation, Vol.1*, B.C. Alleman and A. Leeson (Eds.). Battelle Press, Columbus, OH. pp. 23-28.
- Leonard, B. P. 1988. Universal limiter for transient interpolation modeling of the advective transport equations: The ULTIMATE conservative difference scheme. *NASA Technical Memorandum 100916 ICOMP-88-11*, Washington, DC.
- Lovley, D.R., S.J. Giovannoni, D.C. White, J.E. Champine, E.J.P. Phillips, Y.A. Gorby, and S. Goodwin. 1993. *Geobacter metallireducens*, new genus species, a microorganism capable of coupling the complete oxidation of organic compounds to the reduction of iron and other metals. *Archive Microbiol.* 159(4):336-344.
- Lovley, D.R. and E.J.P. Phillips. 1986. Availability of ferric iron for microbial reduction in bottom sediments of the freshwater tidal Potomac River. *Appl. Environ. Microbiol.* 52(4):751-757.

- Lovley, D.R. and E.J.P. Phillips. 1987. Rapid assay for microbially reducible ferric iron in aquatic sediments. *Appl. Environ. Microbiol.* 53(7):1536-1540.
- Lovley, D.R., M.J. Baedecker, D.J. Lonergan, I.M. Cozzarelli, E.J.P. Phillips, and D.I. Siegel. 1989. Oxidation of aromatic contaminants coupled to microbial iron reduction. *Nature.* 339:297-299.
- Mantoglou, A. and J.L. Wilson. 1982. The turning bands method for simulation of random fields using line generation by a spectral method. *Water Resour. Res.* 18:1379-1394.
- MacQuarrie, K.T.B. and E.A. Sudicky. 1990. Simulation of biodegradable organic contaminants in groundwater, 2. Plume behavior in uniform and random flow fields. *Water Resour. Res.* 26(2):223-239.
- McDonald, J.M and A.W. Harbaugh. 1988. A modular three-dimensional finite difference ground-water flow model. *Techniques of Water Resources Investigations of the U.S. Geological Survey, Book 6.* 586pp.
- Miralles-Wilhelm, F., L. Gelhar, and V. Kapoor. 1997. Stochastic analysis of oxygen-limited biodegradation in three-dimensionally heterogeneous aquifers. *Water Resour. Res.* 24(4):615-619.
- Murphy, E.M., T.R. Ginn, A. Chilakapati, C.T. Resch, J.L. Phillips, T.W. Wietsma, and C.M. Spadoni. 1997. The influence of physical heterogeneity on microbial degradation and distribution in porous media. *Water Resour. Res.* 33(5):1087-1103.
- Munch, J.C. and J.C.G. Ottow. 1980. Preferential reduction of amorphous to crystalline iron oxides by bacterial activity. *Soil Sci.* 129(1):15-21.
- Parkhurst, D.L., S. Christenson, and G.N. Breit. 1993. Groundwater-quality assessment of the central Oklahoma aquifer, Oklahoma; Geochemical and geohydrologic investigations. *U.S. Geological Survey Open File Report 92-642.*
- Sturman, P.J., P.S. Stewart, A.B. Cunningham, E.J. Bouwer, and J.H. Wolfram. 1995. Engineering scale-up of in situ bioremediation processes: A review. *J. Contam. Hydrol.* 19:171-203.
- Suarez, M.P. and H. S. Rifai. 1999. Biodegradation rates for fuel hydrocarbons and chlorinated solvents in groundwater. *J. Bioremed.* 3(4):337-362.
- Tompson, A.F.B., R. Ababou, and L. Gelhar. 1987. Application and use of the three-dimensional Turning Bands random field generation: Single realization problem. *Research Report #313*, Ralph M. Parsons Laboratory, MIT, Cambridge, MA.
- Thomas, J.M and C.H. Ward. 1992. Subsurface microbial ecology and bioremediation. *J. Hazard. Mat.* 32:179-194.
- U.S. Environmental Protection Agency. 1999. Use of monitored natural attenuation at Superfund, RCRA corrective action, and underground storage tank sites. *U.S. Environmental Protection Agency OSWER Directive 9200.4-17P.*
- Waddill, D.W. and M.A. Widdowson. 1998. Three-dimensional model for subsurface transport and biodegradation. *ASCE J. Environ. Engr.* 124(4):336-344.

- Waddill, D.W. and M.A. Widdowson. 1997. SEAM3D: A numerical model for three-dimensional solute transport and sequential electron acceptor-based biodegradation in groundwater. *Documentation and User's Guide*. US Army Corps of Engineers Waterways Experiment Station, Vicksburg, MS.
- Waddill, D.W. 1998. Three-dimensional modeling of solute transport with in situ bioremediation based on sequential electron acceptors. *Ph.D. Dissertation*. Virginia Polytechnic Institute and State University, Blacksburg, VA.
- Zheng, C. and P. Wang. 1999. MT3DMS: A modular three-dimensional transport model for simulation of advection, dispersion, and chemical reactions of contaminants in groundwater systems. *Contract Report SERDP-99-1*. U.S. Army Engineer Research and Development Center, Vicksburg, MS.

## CHAPTER 5

### Numerical Simulation of a Natural Attenuation Experiment with a NAPL Source: Contaminant Dissolution and Reactive Transport

J. STEVEN BRAUNER AND MARK A. WIDDOWSON

*THE CHARLES E. VIA, JR. DEPARTMENT OF CIVIL AND ENVIRONMENTAL ENGINEERING*

*VIRGINIA POLYTECHNIC INSTITUTE AND STATE UNIVERSITY*

#### ABSTRACT

This study presents application of a three-dimensional reactive transport model to the Natural Attenuation Study (NATS), conducted at Columbus Air Force Base (CAFB) in Columbus, Mississippi. NATS was a unique investigation of monitored natural attenuation in that the mass and composition of the hydrocarbon source were known; the aquifer system was highly heterogeneous but well-characterized; and a full suite of hydrocarbon, electron acceptor, and reaction endproduct solute concentrations were collected at various times using a dense, three-dimensional multilevel sampling network. The contaminant source for NATS was a nonaqueous phase liquid (NAPL) mixture of benzene, toluene, ethylbenzene, p-xylene (BTEX), naphthalene, decane, and bromide (conservative tracer) that was released into the shallow unconfined aquifer. Conceptual and mathematical models were developed for NAPL source release, sequential aerobic/anaerobic biodegradation, and sorption during NATS. Using a previously-developed numerical site model for flow and conservative transport, a multiple species, reactive solute transport code (SEAM3D) was employed to simulate fully three-dimensional transport and aerobic, anoxic, iron(III)-reducing, and methanogenic hydrocarbon biodegradation in a 60-m x 60-m x 11-m thick model domain. Simulation results matched BTEX concentration distributions developed at five and nine month period following NAPL release. SEAM3D mass balance calculations showed that the majority (>99%) of hydrocarbon remained in the NAPL phase during the first 9 months of NATS. Of the BTEX and naphthalene source mass, model predictions indicate that 49% was biodegraded, 13% was sorbed, and

38% remained in the aqueous phase. The model also predicted that the complete range of terminal electron accepting processes were active within 9 months of NAPL release, and mass balance calculations indicated that aerobic biodegradation accounted for the majority of hydrocarbon attenuation (37% of the attenuated mass), followed by iron reduction (23%), sorption (21%), nitrate reduction (16%) and methanogenesis (< 4%). Sorption was the dominant attenuation process for both ethylbenzene and naphthalene. Model results were sensitive to the rate of NAPL release, initial condition of electron acceptors, hydrocarbon utilization rates and initial condition for the anaerobic microbial population groups, and dispersivity.

## Introduction

Regulatory acceptance of monitored natural attenuation at petroleum hydrocarbon contaminated sites requires proof that natural processes will achieve site-specific remediation objectives within a reasonable time frame when compared to other potential remediation methods (USEPA, 1999). Quantitative assessment of natural attenuation may require a numerical solute transport model capable of simulating complex biochemical interactions between petroleum hydrocarbon compounds (PHC) and multiple electron acceptors (Waddill and Widdowson, 1998). Several researchers have demonstrated the utility of numerical models that simulate sequential aerobic/anaerobic biodegradation by calibrating these models at petroleum hydrocarbon contaminated sites where the flow field is two dimensional and horizontal (Brauner and Widdowson, 1996; Waddill and Widdowson, 1997; Lu et al, 1999; and others).

The Natural ATtenuation Study (NATS) conducted at Columbus Air Force Base (CAFB) was specifically designed to investigate natural attenuation of PHCs derived from a controlled release in a heterogeneous aquifer (Stauffer et al., 1997) and resulted in a unique solute concentration data set to test numerical fate and transport modeling in heterogeneous groundwater flow systems. The NATS experimental data facilitated application and testing of numerical fate and transport modeling in three ways. First, the initial non-aqueous phase liquid (NAPL) mass of each hydrocarbon was measured prior to source emplacement. Second, the spatial distribution of hydraulic conductivity was well characterized

during previous investigations of the CAFB aquifer. Lastly, time series concentration data for multiple groundwater constituents, including individual PHCs, aqueous phase electron acceptors, and reaction endproducts, were collected from a high resolution, three-dimensional multilevel sampling network.

The purpose of this paper is to demonstrate and evaluate the application of a numerical model for biologically reactive PHC transport at the heterogeneous NATS site. The present study uses the multiple species, sequential electron acceptor model for three dimensional reactive transport (SEAM3D; Waddill and Widdowson, 1998) to recreate the concentration trends observed during the NATS experiment. Results of the numerical model facilitated interpretation of field data and assessment of the relative impact of multiple microbial processes on individual PHCs. The paper presents a brief summary of NATS experimental data, a site conceptual and numerical model, and simulation results. Discussion of model sensitivity and the dominant natural attenuation processes during NATS is also presented.

## Previous Work

The second MAcroDispersion Experiment (MADE-2) was the first of two controlled PHC release experiments in a shallow unconfined aquifer at the CAFB in Columbus, Mississippi. During MADE-2, dissolved p-xylene, benzene, naphthalene, and o-dichlorobenzene were injected into the CAFB aquifer through a line of closely spaced wells, and PHC migration was monitored using a dense network of multilevel samplers (MLS). Analysis of the MLS concentration data indicated that the PHCs were naturally attenuated primarily by a biotransformation and to a lesser degree by sorption (Boggs et al., 1993). Field and laboratory experiments were used to estimate retardation factors and an analytical solution was fitted to the concentration data to estimate first-order biodegradation rates for the injected PHCs, as summarized in Table 1.

The NATS experiment was the second PHC release at the CAFB, when a known mass of NAPL was placed into the Columbus aquifer (Boggs et al., 1995). The mass fraction of BTEX (benzene, toluene, ethylbenzene, p-xylene) and naphthalene in the NAPL was proportional to a typical JP-4 jet fuel, with decane serving as an octane surrogate for the remaining inert fraction of the fuel (Table 2). The NAPL

was mixed with 30 m<sup>3</sup> of clean sand, placed in an excavated trench (hereafter referred to the source trench), and back-filled to land surface with uncontaminated sand. Sheet piling, which had been installed along the walls of the trench to establish hydraulic control, was extracted and the natural groundwater gradient in the source area was restored to allow PHC dissolution into the groundwater. Solute concentrations from selected ports in the MLS network (see Figure 1) were measured 1, 3, 5, 9, 15, and 21 months after sheet pile removal. The most comprehensive collection and analysis was conducted during the sampling events 5 months and 9 months after source removal, hereafter referred to as Snapshot 3 and Snapshot 4, respectively. Analysis of solute concentrations by Libelo et al. (1997) indicated that multiple electron accepting processes were active during the NATS experiment and that PHC transport was influenced significantly by natural attenuation.

Julian et al. (2000) employed a dual domain mass transfer approach for simulating bromide transport during NATS and found general agreement with results from modeling tritium transport during the MADE-2 experiment (Harvey and Gorelick, 1999; Feehley et al., 1999). Julian et al. (2000) recreated the local groundwater flow field via an intermediate scale (ISM) groundwater flow model that preserved the hydraulic conductivity structure of the Columbus aquifer. These researchers simulated solute transport using a small-scale flow and transport model (SSM) of finer resolution than the ISM, with constant head boundaries on all sides of the SSM specified using heads from the calibrated ISM. Julian et al. (2000) interpolated hydraulic conductivity values to the SSM grid directly from flowmeter hydraulic conductivity measurements reported in Boggs et al. (1990). This approach took advantage of the finer spatial discretization of the SSM by preserving local-scale heterogeneity in hydraulic conductivity distribution that may have small effects on head distribution but more noticeable effects on solute transport. The SSM thus provided the base model grid for development of reactive transport simulations using SEAM3D.

## NATS Experiment: Hydrocarbon and Geochemical Observations

For the purpose of this study, hydrocarbon, electron acceptor, and reaction end product concentration data collected during NATS were interpolated onto a three-dimensional grid and two-dimensional contour plots were rendered along multiple vertical and horizontal transects through the hydrocarbon plume. Grid spacing for the interpolation scheme was chosen as 1-m by 1-m by 0.5-m vertical, which was of adequate resolution to preserve small-scale heterogeneity. Vertical and horizontal cross-sections provided a means for interpretation of field data, and later, for evaluating the accuracy of the three dimensional reactive solute model.

### Hydrocarbon and TEAP Distribution

Interpolated BTEX concentration data from Snapshot 3 exhibited distinctive fingering effects. Using the hydraulic conductivity distribution developed for the SSM by Julian et al. (2000), Figure 2 shows that observed toluene and ethylbenzene ‘fingers’ coincided with zones of high hydraulic conductivity immediately down-gradient (i.e. within 15-20m) of the source trench along the vertical transect indicated in Figure 1. Concentration plots of all five readily-soluble PHCs at several cross sections exhibited similar distinctive fingering, which was more pronounced than similar contour plots of the conservative tracer, bromide. The PHC plume was also spread over a smaller vertical and horizontal distance than bromide, which previous researchers have attributed to a combination of sorption and biodegradation of the PHCs (Libelo et al, 1997, Boggs and MacIntyre, 2000).

Figures 3A and 3B show that dissolved oxygen and nitrate concentrations, respectively, of less than 1 mg/L were generally located in zones of high hydraulic conductivity and that a zone of depletion was observed to increase in size between Snapshot 3 and Snapshot 4. Concentrations of two reaction endproducts, iron(II) and methane, were also observed to increase between Snapshots 3 and 4. The highest concentrations of iron(II) and methane were measured in zones where oxygen and nitrate were depleted (Figure 3C and 3D, respectively).

Libelo et al. (1997) and Boggs and MacIntyre (2000) noted that the concentration trends observed in the NATS experiment suggest biodegradation of at least some PHCs under multiple electron acceptor conditions. These findings support earlier work by Boggs et al. (1995) that both aerobic and anaerobic biodegradation processes were active in the Columbus aquifer. Stapleton et al. (1999) report that the aerobic microbial population possessing specific hydrocarbon-degrading genes was greater inside the plume when compared to the background population. Production of iron(II) and methane suggest that iron(III)-reducing and methanogenic microbial populations were also active in the anoxic zone created immediately downgradient of the source area. Although some data suggested localized sulfate consumption, there is no definitive evidence that sulfate-reducing bacteria were actively biodegrading PHCs during the NATS experiment (Boggs and MacIntyre, personal communication).

Terminal electron acceptor process (TEAP) zonation has been observed at numerous petroleum hydrocarbon sites where sequential biodegradation was observed (Boggs et al., 1993; Vroblesky and Chapelle, 1994; Wiedemeier et al., 1995; Borden et al., 1995 and others). Lovley et al. (1994) successfully correlated dissolved hydrogen ( $H_2$ ) concentrations to TEAPs by comparing field measured  $H_2$  concentrations to observed TEAPs in microcosm experiments. Measurements of background  $H_2$  concentration in the Columbus aquifer ranged from below detection to 0.2 nM. At Snapshots 3 and 4,  $H_2$  concentrations measured in the first MLS row downgradient of the source trench generally ranged between 0.3 nM to 0.6 nM, indicating iron(III)-reducing conditions. Although the increase in  $H_2$  concentration suggests moderately reduced conditions, the extreme heterogeneity of the Columbus aquifer may have produced localized anaerobic microenvironments at a vertical scale smaller than the spacing of the MLS ports. For example,  $H_2$  concentrations measured in one sampling point downgradient of the source area were consistently greater than the 5 nM concentration, which Lovley et al. (1994) suggest as a lower bound for defining methanogenic activity, whereas  $H_2$  concentrations measured at adjacent ports 0.5-m above and below this point were at background levels. Areal delineation of TEAP zones was also difficult for the Columbus aquifer since  $H_2$  was measured only at limited MLS locations, and it was

impossible to sample H<sub>2</sub> in the area immediately downgradient of the source trench due to an approximately 3-m gap between the source trench and the first MLS row.

### **Variability in Hydrocarbon Biodegradation**

Research has shown that toluene and p-xylene tend to biodegrade at higher rates and/or under more electron acceptor conditions than ethylbenzene and benzene in mixed PHC plumes (Acton and Barker, 1992; Chang et al., 1993; Arcangeli and Arvin, 1994; Borden et al., 1995; Borden et al., 1997). Although other experimental data (e.g., laboratory microcosm experiments) are required for conclusive proof, a novel approach was employed to assess variability in hydrocarbon degradation using the MLS concentration data. Figure 4 is a plot of toluene versus ethylbenzene concentrations at Snapshots 3 and 4, showing that toluene concentrations were decreasing with time relative to ethylbenzene concentrations. Even though the solubility of toluene is greater than ethylbenzene, toluene concentrations tended to be lower than ethylbenzene concentrations by Snapshot 4. A similar plot of p-xylene versus ethylbenzene (not shown) indicated similar trends. One explanation for the decline in toluene and p-xylene concentrations relative to ethylbenzene concentrations is that biodegradation under anaerobic conditions consumed more toluene and p-xylene relative to ethylbenzene during the NATS experiment. Figure 5 shows a strong linear relationship between benzene and ethylbenzene concentrations, suggesting that these compounds were attenuated by similar phenomena and at similar rates in the Columbus aquifer. The notion of comparable benzene and ethylbenzene biodegradation conditions and rates agreed with findings from multiple microcosm studies using soil samples from various PHC contaminated sites, as summarized in Salanitro et al. (1997).

### **Conceptual Model**

Based on the findings of Boggs et al. (1993, 1995), Libelo et al. (1997), Boggs and MacIntyre (2000) and the observations noted above, a conceptual model for a reactive solute transport model of the NATS experiment was developed. A single-solute, non-reactive transport model developed in Julian et al.

(2000) was adapted to the reactive solute model developed for this study by the addition of multiple solutes, NAPL source release, sequential aerobic/anaerobic biodegradation, and linear sorption.

### **Solutes**

The model for the NATS experiment was designed to simulate the fate and transport of eleven constituents: one conservative tracer (bromide), five non-conservative PHCs (BTEX and naphthalene), two aqueous phase electron acceptors (dissolved oxygen and nitrate), one solid phase electron acceptor (iron(III)), and two reaction end products (iron(II) and methane). Although decane was the largest mass percentage (75.6% by weight) of the source NAPL, Libelo et al. (1997) reported that the low solubility of decane ( $< 9 \mu\text{g/L}$ ) prevented migration from the source area. Decane was therefore not included as an aqueous phase solute in the conceptual model and was modeled only as an inert fraction of the NAPL.

### **Sorption, Phase Transfer, and the Dual Domain Approach**

Abiotic hydrocarbon attenuation in the Columbus aquifer was investigated using two different conceptual models. In the first model, hereafter referred to as the single porosity model, PHC sorption was assumed to follow a linear, isothermic relationship in the Columbus aquifer. BTEX and naphthalene were distributed between non-aqueous (NAPL), aqueous, and sorbed phases. The second model, hereafter referred to as the dual domain model, simulated the aqueous phase as two distinct mobile and immobile phases but did not simulate PHC concentration variables for the solid phase. Mass transfer between the aqueous mobile and immobile phases was allowed in the dual domain model, but biodegradation was assumed to occur only in the mobile phase. Zheng and Jiao (1998) and others found that modeling non-reactive solute transport in the Columbus aquifer using a dual domain approach improved model fit to bromide concentration measurements when compared to a Fickian advection-dispersion model. Considering that the PHC in the NATS experiment are strongly sorbing compounds relative to bromide, both models for abiotic PHC attenuation were employed to simulate the experiment. In both models, aqueous electron acceptors were modeled as a single mobile phase. Iron(III) was assumed to have a negligible aqueous component.

## **NAPL Release**

During the NATS experiment, mobile aqueous phase PHCs entered the Columbus aquifer by dissolution from the NAPL phase and physical transport from the source trench. Julian et al. (2000) noted that bromide release from the eastern half of the source trench was limited relative to the western half of the trench. Similarly, PHC concentrations down-gradient of the eastern half of the source trench suggested that the release of mass into this region was slower than release from the western half of the trench. Figure 6 shows the location of the source area relative to the hydraulic conductivity distribution on the down-gradient face of the source trench. Smearing of fine-grained sediments during sheet pile installation and removal may have more extensively clogged pores in the eastern portion of the trench relative to the western portion, thereby contributing to the differential contaminant migration observed in the transverse direction.

## **Biodegradation**

Based on field observation, PHC biodegradation was simulated by aerobic, anoxic, iron(III)-reducing, and methanogenic processes. Each readily-soluble PHC served as an electron donor/growth substrate, but PHC biodegradability was specified as variable by TEAP. Toluene and p-xylene were assumed to biodegrade under all simulated electron acceptor conditions. Ethylbenzene and benzene were assumed to biodegrade only under aerobic and methanogenic conditions. Naphthalene was simulated to biodegrade only under aerobic conditions. Decane was treated as an inert fraction of the source NAPL and was not simulated to biodegrade under any conditions.

## **Numerical Model**

### **Reactive Solute Transport Model**

The SEAM3D reactive transport model (Waddill and Widdowson, 1998) was chosen to simulate the NATS experiment, as the major features of this model (NAPL dissolution and sequential aerobic-anaerobic biodegradation) were present during the NATS experiment. SEAM3D input included specification of parameters for advection, dispersion, sorption, biodegradation, NAPL source release, and

output control options. SEAM3D output included both unformatted concentration files and columnar mass balance files. The mass balance files created by SEAM3D recorded the mass of each constituent remaining in a particular phase (i.e. NAPL, sorbed, or aqueous) and the mass of each substrate biodegraded under each TEAP.

### **Grid Design and Boundary Conditions**

The finite difference model grid for the present study was identical to the SSM described in Julian et al. (2000) and consisted of a 22 layer model with 60 nodes in both horizontal directions. Grid spacing was 1-m horizontally and 0.5-m vertically, which created the square model domain shown in Figure 1 (plan view). The reactive transport model was fully three-dimensional so that vertical flow and preferential pathways in the Columbus AFB aquifer may be simulated. Solute transport equations in the reactive transport model were solved using a third order total-variant-diminishing (TVD) scheme based on the ULTIMATE algorithm (Leonard, 1988). A Courant number of 1.0 was specified to satisfy stability and accuracy requirement of the model, thus limiting each transport step size to 0.17 days for the single porosity model and  $2.9 \times 10^{-2}$  days for the dual domain model.

Initial hydrocarbon, electron acceptor, and reaction end product concentrations were specified based on field observations outside the NATS contaminant plume. Initial aqueous phase PHC concentrations were specified as zero, as background concentrations in the Columbus aquifer were below detection. Initial oxygen and nitrate concentrations were uniformly set at 4.0 and 4.4 mg/L, respectively, based on concentrations measured prior to source emplacement. The initial concentration of bioavailable iron(III) for the NATS model was specified as  $50 \mu\text{g Fe}^{3+}/\text{g soil}$ . Maximum total iron(III) concentrations in the Columbus aquifer were reported as 1 percent of the total soil mass by Libelo et al (1997), but these researchers only found small quantities of ferrihydrite and no observed amorphous iron oxides. In a microcosm study using freshwater sediments from the Potomac River, Lovely and Phillips (1986) demonstrated that ferrihydrite and amorphous iron(III) oxyhydroxides were the only biologically reducible forms of iron(III). Based on MLS concentration data, initial iron(II) and methane

concentrations were set at zero. Boundary conditions were specified as zero flux for all constituents at each side of the model grid except for the upgradient (southern) flow boundary. Influent concentrations for all model constituents were specified as equal to the initial condition and held constant over time.

### Single Porosity Model: Governing Equations

The governing equation for PHC fate and transport in the single porosity model, as developed in Waddill and Widdowson (1997), was expressed as

$$R_{ls} \frac{\partial S_{ls}}{\partial t} = \frac{\partial}{\partial x_i} \left( D_{ij} \frac{\partial S_{ls}}{\partial x_j} \right) - \frac{\partial}{\partial x_i} (v_i S_{ls}) + R_{source,ls}^{NAPL} - R_{sink,ls}^{Bio} \quad (1)$$

where  $S_{ls}$  is the aqueous phase hydrocarbon concentration [ $M_{ls} L^{-3}$ ] for compound  $ls$  ( $ls = 1,2,\dots,5$ ),  $D_{ij}$  is the hydrodynamic dispersion coefficient tensor [ $L T^{-1}$ ],  $v_i$  is the average pore water velocity [ $L T^{-1}$ ],  $R_{source,ls}^{NAPL}$  is the rate of hydrocarbon transfer from the NAPL to the aqueous phase,  $R_{sink,ls}^{Bio}$  is the rate of hydrocarbon removal by biodegradation, and  $R_{ls}$  is the retardation factor, which accounts for sorption of each PHC. For a linear sorption model, the retardation factor was calculated as

$$R_{ls} = 1 + \frac{\rho_b}{\theta} k_{d,ls} \quad (2)$$

where  $\rho_b$  is the soil bulk density [ $M L^{-3}$ ],  $k_{d,ls}$  is the distribution coefficient [ $L^3 M^{-1}$ ], and  $\theta$  is the effective porosity.

Mass balance calculations for aqueous phase electron acceptors and reaction end products were made using Equations (3) and (4), respectively:

$$\frac{\partial E_{le}}{\partial t} = \frac{\partial}{\partial x_i} \left( D_{ij} \frac{\partial E_{le}}{\partial x_j} \right) - \frac{\partial}{\partial x_i} (v_i E_{le}) - R_{sink,le}^{Bio} \quad (3)$$

$$R_{lp} \frac{\partial P_{lp}}{\partial t} = \frac{\partial}{\partial x_i} \left( D_{ij} \frac{\partial P_{lp}}{\partial x_j} \right) - \frac{\partial}{\partial x_i} (v_i P_{lp}) + R_{source,lp}^{Bio} \quad (4)$$

where  $E_{le}$  is the aqueous phase concentration [ $M_{le} L^{-3}$ ] of electron acceptor  $le$  ( $le = 1$  for oxygen, and 2 for nitrate),  $R_{sink,le}^{Bio}$  is the rate of electron acceptor removal by biodegradation,  $P_{lp}$  is the aqueous phase

concentration [ $M_{ip} L^{-3}$ ] of biodegradation end product  $lp$  ( $lp = 1$  for iron(II), and 2 for methane), and  $R_{source,lp}^{Bio}$  is the rate of end product generation. The mass balance equation for the solid-phase electron acceptor ( $le = 3$  for iron(III)) was expressed as

$$\frac{\partial E_{le}}{\partial t} = -R_{sink,le}^{Bio} \quad (5)$$

### Dual Domain Model: Governing Equations

The general equation of transport in the dual domain model was expressed as

$$\theta_m \frac{\partial C_m}{\partial t} + \theta_{im} \frac{\partial C_{im}}{\partial t} = \frac{\partial}{\partial x_i} \left( \theta_m \hat{D}_{ij} \frac{\partial C_m}{\partial x_j} \right) - \frac{\partial}{\partial x_i} (q_i C_m) + \theta_m R_{source}^{NAPL} + \theta_m R_{source}^{Bio} - \theta_m R_{sink}^{Bio} \quad (6)$$

where  $C_m$  is the solute concentration in the mobile domain [ $M L^{-3}$ ],  $C_{im}$  is the solute concentration in the immobile domain [ $M L^{-3}$ ],  $\theta_m$  is the portion of the total porosity filled with mobile water,  $\theta_{im}$  is the portion of the total porosity filled with immobile water,  $\hat{D}_{ij}$  is the apparent dispersion coefficient tensor [ $L T^{-1}$ ] (calculated from the Darcy flux rather than the seepage velocity), and  $q_i$  is the Darcy flux [ $L T^{-1}$ ]. Equation (6) may be modified for each solute category (i.e., hydrocarbon, electron acceptor, and biodegradation end product). A reversible, first-order mass transfer function simulated solute transfer between the mobile and immobile zones, expressed as

$$\theta_{im} \frac{\partial C_{im}}{\partial t} = \beta (C_m - C_{im}) \quad (7)$$

where  $\beta$  is the mass transfer rate [ $T^{-1}$ ] between the mobile and immobile zones (Zheng and Wang, 1999).

### NAPL Dissolution

Hydrocarbon dissolution from the NAPL phase to the aqueous phase was simulated as a rate limited mass transfer function. Waddill and Widdowson (1997) expressed the rate of NAPL release,  $R_{source,ls}^{NAPL}$ , as a function of a mass transfer rate coefficient ( $k^{NAPL}$ ) and the phase concentration differential:

$$R_{source,ls}^{NAPL} = k^{NAPL} (S_{ls}^{eq} - S_{ls}). \quad (8)$$

where  $S_{ls}^{eq}$  is the equilibrium concentration for PHC compound  $ls$ . Since all PHCs included in the NATS model were similar in structural hydrophobicity, the equilibrium concentration of each hydrocarbon was assumed as equal to the effective aqueous solubility. Using the effective solubility approach developed in Banerjee (1984), the molar concentration of the  $i^{th}$  component in a mixture ( $S_i^{eq}$ ) was estimated as:

$$S_i^{eq} = f_i S_i^{sol} \quad (9)$$

where  $f_i$  was the mole fraction of the  $i^{th}$  constituent in the NAPL and  $S_i^{sol}$  was the pure phase solubility of the  $i^{th}$  solute in water. A mass balance equation was also solved for each component in the NAPL phase.

### Biodegradation Kinetics

Hydrocarbon mass loss due to biodegradation was expressed as the sum of aerobic and anaerobic processes, which was a function of PHC and electron acceptor concentrations and was given by:

$$R_{sink,ls}^{Bio} = \sum_{le} \sum_x \frac{M_x}{\theta_m} v_{x,ls,le}^{max} \left[ \frac{\bar{S}_{ls}}{\bar{K}_{x,ls,le}^s + \bar{S}_{ls}} \right] \left[ \frac{\bar{E}_{le}}{\bar{K}_{x,le}^e + \bar{E}_{le}} \right] I_{le,li} \quad (10)$$

where  $M_x$  is the population of microcolony  $x$  [ $M_b L^{-3}$ ],  $v_{x,ls,le}^{max}$  is the maximum specific rate of substrate utilization for microcolony  $x$  growing on substrate  $ls$  and electron acceptor  $le$  [ $M_{ls} M_b^{-1} T^{-1}$ ],  $\bar{K}_{x,ls,le}^s$  is the effective half saturation constant for substrate  $ls$  utilizing electron acceptor  $le$  [ $M_{ls} L^{-3}$ ];  $\bar{K}_{x,le}^e$  is the effective half saturation constant for electron acceptor  $le$  [ $M_{le} L^{-3}$ ];  $\bar{S}_{ls}$  is the effective concentration of substrate  $ls$  [ $M_{ls} L^{-3}$ ]; and  $\bar{E}_{le}$  is the effective concentration of electron acceptor  $le$  [ $M_{le} L^{-3}$ ].  $I_{le,li}$  is an inhibition function defined by

$$I_{le,li} = 1 \quad \text{for } le = 1 \quad (11a)$$

$$\text{and} \quad I_{le,li} = \prod_{li=1}^{le-1} \left[ \frac{\kappa_{le,li}}{\kappa_{le,li} + \bar{E}_{li}} \right] \quad \text{for } le = 2, 3 \text{ or } 4 \quad (11b)$$

where  $k_{le,li}$  is the electron acceptor inhibition coefficient [ $M_{le} L^{-3}$ ] representing inhibited utilization of electron acceptor  $le$  in the presence of electron acceptor  $li$ . In the case of methanogenesis, the electron acceptor Monod term in Equation (10) is not present.

Aqueous phase electron acceptor mass loss due to biodegradation was summed over all applicable microbial populations (oxygen may be utilized by strict aerobic bacteria and facultative, nitrate-reducing bacteria) and over all applicable PHC compounds:

$$R_{sink,le}^{Bio} = \sum_{ls} \sum_x \frac{M_x}{\theta_m} \gamma_{x,ls,le} v_{x,ls,le}^{max} \left[ \frac{\bar{S}_{ls}}{\bar{K}_{x,ls,le}^s + \bar{S}_{ls}} \right] \left[ \frac{\bar{E}_{le}}{\bar{K}_{x,le}^e + \bar{E}_{le}} \right] I_{le,li} \quad (12)$$

where  $g_{x,ls,le}$  is the electron acceptor use coefficient [ $M_{le} M_{ls}^{-1}$ ], representing the mass of electron acceptor  $le$  used per unit mass of substrate  $ls$ . Iron(III) utilization ( $x = le = 3$ ) was expressed as

$$R_{sink,le}^{Bio} = -\frac{M_x}{\rho_b} \sum_{ls} \gamma_{x,ls,le} v_{x,ls,le}^{max} \left[ \frac{\bar{S}_{ls}}{\bar{K}_{x,ls,le}^s + \bar{S}_{ls}} \right] I_{le,li} \quad (13)$$

Equation 13 is set at zero in the event that microbial utilization results in depletion of iron(III).

The rate of iron(II) generation was a function of the rate of electron acceptor ( $x = le = 3$ ) utilization, given by

$$R_{source,le}^{bio} = \mathbf{z}_{x,le} \frac{M_x}{\mathbf{q}} \sum_{ls} \mathbf{g}_{x,ls,le} \mathbf{n}_{x,ls,le}^{max} \left[ \frac{\bar{S}_{ls}}{\bar{K}_{x,ls,le}^s + \bar{S}_{ls}} \right] I_{le,li} \quad (14)$$

where  $\mathbf{z}_{x,le}$  is the product generation coefficient [ $M_{lp} M_{le}^{-1}$ ]. For the methane production ( $x = le = 4$ ), the source term is a function of the rate of substrate utilization, given by

$$R_{source,CH_4}^{bio} = \sum_{ls} \mathbf{z}_{x,ls} \frac{M_x}{\mathbf{q}} \mathbf{n}_{x,ls,le}^{max} \left[ \frac{\bar{S}_{ls}}{\bar{K}_{x,ls,le}^s + \bar{S}_{ls}} \right] I_{le,li} \quad (15)$$

where  $\mathbf{z}_{x,ls}$  is the methane generation coefficient [ $M_{lp} M_{ls}^{-1}$ ].

## Model Parameter Selection

### Solute Transport and Phase Transfer Parameters

Solute transport and phase transfer parameters for both the single porosity and dual domain model were derived from previous studies at the NATS site and are summarized in Table 3. As part of model calibration, longitudinal dispersivity was varied between 0 and 1 m, while the ratio of longitudinal to transverse to vertical dispersivity was maintained at 1.0 to 0.1 to 0.01. Retardation factors for benzene and naphthalene were specified within the range reported by Boggs et al. (1993), while retardation factors for the remaining PHCs were chosen based on literature values. For the dual domain model, the mass transfer coefficient between the mobile and immobile phases ( $b$ ) and the values for mobile and immobile porosity were identical to those reported for bromide transport by Julian et al. (2000).

### NAPL Dissolution Parameters

Table 2 lists input parameters required for each NAPL component when the SEAM3D NAPL package is used to simulate mass transfer to the aqueous phase. Two of the input parameters, solubility and molecular weight, are widely available in chemical handbooks and were used to calculate the effective solubility for each NAPL constituent. The total NAPL mass and mass fraction of each NAPL component (by weight) are site-specific parameters and often require estimation for each source. The NATS experiment was unique in that both the total NAPL mass and the initial mass fraction of each PHC was known, and therefore did not need to be estimated. The initial NAPL mass was 608.4 kg and mass fraction of each NAPL component is reported in the last column of Table 2.

The SEAM3D NAPL package also requires a mass transfer coefficient ( $k^{NAPL}$ ) for simulating NAPL release to the aqueous phase. Through trial-and-error parameter adjustment and the matching of PHC concentration data measured at the first line of MLS transverse to flow,  $k^{NAPL}$  was estimated as  $5 \times 10^{-3} \text{ days}^{-1}$  for the NATS source. The observed additional clogging noted in the eastern portion of the source by Julian et al. (2000) was accounted for by reducing  $k^{NAPL}$  by one order of magnitude for selected eastern source nodes.

## Biodegradation Parameters

Table 4 lists the biokinetic and stoichiometric parameters for the calibrated single porosity model. Half saturation constants and yield coefficients were chosen within the range of values typically reported in the literature for PHC sites (e.g., Waddill and Widdowson, 1997). Electron acceptor use coefficients and methane production coefficients were calculated using stoichiometric relationships that account for PHC oxidation and conversion to biomass, originally developed in McCarty (1975). The iron(II) production coefficient was adjusted such that model predicted iron(II) concentrations were consistent with field measured values. The calibrated value is lower than that predicted stoichiometrically, as aqueous phase iron(II) is highly reactive and often precipitates to the solid phase in the subsurface environment (Lovley et al., 1994). Inhibition coefficients were chosen based on observations of electron acceptor disappearance and reaction end product formation.

Waddill and Widdowson (1998) indicated that adjustments to the maximum specific utilization rate ( $\mu_{x,ls,le}^{max}$ ) govern the overall importance of a particular electron accepting process, while changes in the initial microbial population served to simulate the lag-time often noted prior to the onset of biodegradation. The initial microbial population and  $\mu_{x,ls,le}^{max}$  were adjusted to the values reported in Table 5 by trial-and-error to attain the calibrated single porosity model. The methanogenic microbial population was specified as constant with time ( $Y_{x,ls,le} = 0$  for  $le = 5$ ), which caused substrate utilization under methanogenic conditions to be calculated at a first order decay rate of 0.0017 days<sup>-1</sup> following the depletion of oxygen, nitrate, and iron.

## Results and Discussion

### Model Calibration

Trial-and-error parameter adjustment was used to calibrate the reactive transport model to solute concentration distributions collected at Snapshots 3 and 4, respectively. Model calibration was evaluated by comparing simulated concentrations with field data at selected MLS locations and at three vertical

cross sections oriented in the main direction of flow. The vertical transect shown in Figure 1 offered an optimal profile for comparing experimental and model results at Snapshots 3 and 4. Comparisons between model-generated vertical and horizontal cross sections and those developed using field data were useful in determining whether a particular model parameter set was recreating the general trends observed during NATS. Zheng and Jiao (1998) and Julian et al. (2000) successfully employed a similar qualitative approach to model calibration, as opposed to a point-by-point comparison, for non-reactive transport in the Columbus aquifer of tritium and bromide, respectively.

### **Single Porosity Model**

Figure 7 presents contour plots of field data (left column) and calibrated single porosity model results (right column) for a vertical cross section located 4-m west of the source centerline for benzene, toluene, ethylbenzene, p-xylene, and naphthalene. Comparison between columns in Figure 7 shows that the calibrated model recreated the fingering observed for the 1 mg/L BTEX contour at Snapshot 3, and generally reproduced the vertical and longitudinal extent of BTEX concentration plumes. The vertical and longitudinal dimensions of the naphthalene plume were also reproduced by the single porosity model, but field measured naphthalene concentrations in and around the source area were approximately five times higher than model predicted values at Snapshot 3. The calibrated single porosity model was compared with field observations at Snapshot 4 along the same vertical cross section, as presented in Figure 8. The calibrated single porosity model was able to recreate the observed concentration distribution of BTEX at Snapshot 4, as both the field and model simulated BTEX concentrations were observed to increase in the upper portion (i.e. greater than 59-m) of the plume relative to the lower portion (i.e. less than 59-m). As with Snapshot 3, the single porosity model reproduced the longitudinal and vertical extent of the observed naphthalene plume at Snapshot 4, but observed concentrations were an order of magnitude greater in the observed plume relative to the model predicted values.

Horizontal slices of the field measured and model simulated PHC concentrations, taken at an elevation which passed through the source trench (i.e. 60-m), showed that the reactive transport model

captured horizontal variations in PHC transport. As an example, Figure 9 depicts horizontal contour plots of toluene concentration developed from field data (left column) and the calibrated single porosity model (right column) for Snapshots 3 and 4. Figure 9 shows agreement between field observations and model simulations in that toluene migration in the western portion of the plume was greater than the eastern portion. The model simulated reduced PHC migration downgradient of the eastern portion of the source trench by inhibited PHC release and decreased solute transport due to the low hydraulic conductivity in that area.

Figure 10 contains a plot of model calculated toluene concentration versus ethylbenzene concentration for all sampled MLS locations for Snapshots 3 and 4. Similar to Figure 4, results of the calibrated single porosity model predicted decreasing toluene concentrations with time relative to the ethylbenzene concentrations. In addition, the model predicted that toluene concentrations were near zero at multiple sampling points where ethylbenzene was present. A plot of model calculated benzene concentration versus ethylbenzene concentration for all sampled MLS points (Figure 11) showed that the single porosity model predicted a nearly perfectly linear trend between ethylbenzene and benzene concentration. A cross plot of field measure benzene versus ethylbenzene concentration, shown in Figure 5, also showed a direct correlation between these compounds, although there was more scatter in the field data than predicted by the model.

Simulation results for electron acceptor and reaction end product concentration distributions along the vertical transect are depicted in Figure 12 at Snapshots 3 and 4. Simulation of PHC biodegradation under aerobic and anoxic conditions produced a oxygen- and nitrate depleted zone from the source trench to approximately 14-m downgradient of the source area, as shown in Figures 12A and 12B, respectively. The zone of oxygen and nitrate depletion grew slightly larger between Snapshots 3 and 4, primarily in the upper part of the PHC plume shown in the selected cross section. Figure 12C shows that the calibrated model predicted iron(III)-reduction as active by Snapshot 3, and the increasing size of the iron(II) plume from Snapshots 3 to Snapshot 4 shows that the zone of iron(III)-reduction is growing

with time. The calibrated model also predicted methane production in zones that were otherwise depleted of electron acceptors, and Figure 12D shows that the model simulated increasing methane concentrations with time. Comparison of model simulated oxygen and nitrate concentrations with field measurements of these electron acceptors (as shown in Figures 3A and 3B, respectively) indicated that the model predicted a more clearly defined anaerobic zone than field data. One explanation for the disparity between the model and simulated results is that transient and spatial variation in the levels of oxygen and nitrate were not fully captured in the model-specified initial and upgradient boundary conditions. Better agreement between model predicted and field measured concentrations was realized for the reaction endproducts. The longitudinal extent and concentration distribution of both the iron(II) and methane plumes and concentration levels were comparable to the field data cross-sections shown in Figures 3C and 3D, respectively.

### **Dual Domain Model**

Using the microbial parameters from the calibrated single porosity model listed in Tables 3 and 4, the dual domain approach was applied for reactive transport during the NATS experiment. Figure 13 presents contour plots for results of the dual domain model at Snapshots 3 and 4 for BTEX and naphthalene. The left column of Figure 13 shows that the dual domain model for solute transport did not reproduce the distinctive hydrocarbon fingering observed for the toluene, ethylbenzene, and p-xylene during Snapshot 3 as was simulated with the single porosity model (see Figure 7). Model-predicted BTEX concentration distributions at Snapshot 4 (right column of Figure 13) were in better agreement with field measured concentrations, although the 5 mg/L contour for toluene was further down-gradient in the dual domain model than the field data indicated. Overall, the single porosity (right column of Figure 8) and dual domain (right column of Figure 13) models showed similar results at Snapshot 4. Although these results show that the single porosity model was better able to reproduce observed PHC transport through preferential flow paths at Snapshot 3, simulating biodegradation obscured the differences between these models by Snapshot 4.

## Model Sensitivity

The reactive transport model was most sensitive to the NAPL mass transfer rate ( $k^{NAPL}$ ), the initial concentration of bioavailable iron(III), the substrate utilization rate ( $\mathbf{n}_{x,ls,le}^{max}$ ) and initial microbial population ( $M_x$ ) for the iron(III)-reducing and methanogenic populations, and dispersivity. PHC attenuation was also sensitive to the ambient oxygen and nitrate concentration, but field measurements indicated that the influent concentrations for these aqueous electron acceptors were not highly variable with time.

Order of magnitude changes in  $k^{NAPL}$  caused changes in both the concentration and length of the simulated PHC plumes. For example, an order of magnitude decrease in the dissolution parameter resulted in PHC transport of less than 5 m at Snapshot 4, compared to the observed length of approximately 15 m. Increasing  $k^{NAPL}$  by an order of magnitude resulted in simulated PHC plumes that were greater than 20 m in length at some locations, with PHC concentrations greater than 5 mg/L extending more than 10 m downgradient of the source trench by Snapshot 4.

Background concentration of bioavailable iron(III) was unknown for the Columbus aquifer, so the initial iron(III) concentration was allowed to vary between 10 and 200  $\mu\text{g}/\text{kg}$  during calibration. The effects of changing the iron(III) initial condition were most noticeable at Snapshot 4. Increasing the iron(III) concentration to 200  $\mu\text{g}/\text{kg}$  caused the model to overpredict toluene and p-xylene biodegradation, as observed in toluene and p-xylene concentrations near the source trench less than 5 mg/L by Snapshot 4. Reducing the iron(III) concentration below the calibrated initial condition (50  $\mu\text{g}/\text{kg}$ ) resulted in insufficient attenuation of toluene and p-xylene.

Model predicted PHC concentrations were more sensitive to changes in  $\mathbf{n}_{x,ls,le}^{max}$  and  $M_x$  for anaerobic populations (i.e.  $x = 3, 4$ ) than higher-energy TEAP populations. Order of magnitude variation in the initial aerobic and facultative microbial populations had little effect on PHC biodegradation, indicating that electron acceptor availability was the limiting factor. A 50 percent decrease in either

$n_{x,ls,le}^{max}$  or  $M_x$  for the iron-reducing population resulted in minimal anaerobic PHC biodegradation through Snapshot 4, causing the model to over-predict toluene and p-xylene concentrations. Increasing either of these variables for the iron-reducing population by 50 percent had little effect on model results through Snapshot 4, as iron(III) depletion limited further biodegradation. A 50 percent increase in the rate of methanogenic PHC biodegradation resulted in an over-prediction of field-measured methane concentrations, but had little noticeable effect on PHC concentration distribution at Snapshots 3 or 4.

No noticeable differences were observed in model predictions of PHC transport for a longitudinal dispersivity at or below the local scale (i.e.,  $\alpha_L \leq 1.0$  cm). Increasing the longitudinal dispersivity to 1.0 m ( $\alpha_{TH} = 0.10$  m and  $\alpha_{TV} = 0.010$  m), however, resulted in model simulations which over-predicted the horizontal extent of PHC transport, under-predicted PHC concentrations in and around the source trench, and did not recreate the hydrocarbon fingering observed at Snapshot 3.

### **PHC Attenuation**

SEAM3D mass balance calculations using the single porosity model with zero dispersivity were compiled to quantify biotic PHC mass loss (specified by TEAP) and abiotic PHC mass attenuation for the NATS experiment. At Snapshot 4, the SEAM3D model predicted that approximately 99 percent of the original BTEX and naphthalene mass was still in the NAPL phase. For the BTEX and naphthalene mass which was simulated to dissolve into the aqueous phase by Snapshot 4, mass balance calculations indicated that 49 percent was biodegraded, 13 percent was sorbed to the aquifer, and the remaining 38 percent was present in the aqueous phase. Aerobic biodegradation was calculated to have transformed more aqueous phase PHC than any other simulated process, and accounted for 37 percent of the transformed PHC. Mass balance calculations indicated that iron(III)-reduction accounted for 23 percent of aqueous phase PHC removal, followed by sorption (21%), nitrate reduction (16%) and methanogenesis (< 4%).

Figure 14 reports the cumulative PHC mass transformed by each simulated natural attenuation process at Snapshots 3 and 4. The results in Figure 14 indicate that the principal natural attenuation

process varied by PHC and, in some cases, with time. For example, the calibrated single porosity model calculated that the dominant transformation process for toluene and p-xylene was aerobic biodegradation, while sorption was simulated as the dominant attenuation process for ethylbenzene and naphthalene. No single transformation process accounted for benzene attenuation, as the model indicated that the mass of transformed benzene was comparable for all three simulated processes (aerobic biodegradation, methanogenic biodegradation, and sorption). The increasing importance of toluene removal by iron(III)-reduction with time is also illustrated in Figure 14, as toluene mass transformation under iron(III)-reduction was predicted to increase by more than a factor of three between Snapshots 3 and 4.

## Conclusions

This study was successful in developing a numerical model to simulate PHC transport during the NATS experiment. Model calibration was realized at Snapshot 3 (5 months after NAPL release) using a single porosity transport model with zero dispersivity. Model calibration to observed BTEX concentration distributions was more successful than results for naphthalene, although the overall length and width of the simulated naphthalene plume compared favorably with field observations. The numerical model for the NATS site was verified using a second data set at Snapshot 4 (9 months after NAPL release). Considering that anaerobic processes had little effect on PHC attenuation at Snapshot 3, matching field observations at Snapshot 4 served more to complete the calibration process than as a true model verification step.

The model also predicted the development of multiple TEAP zones following PHC release, which agreed with analysis of field data reported by Libelo et al. (1997) and Boggs and MacIntyre (2000). Simulation results for oxygen and nitrate may improve if a non-uniform initial and/or boundary concentration could be used for these electron acceptors, but insufficient data was available prior to the NATS experiment to create a non-uniform initial condition. Model predictions for the formation of two reaction endproducts, iron(II) and methane, were in agreement with field observations. Both field data and model results suggested that the anaerobic processes, including methanogenesis, were active and

detectable less than 9 months after NAPL release. In contrast, observations at a gasoline-contaminated site in a relatively homogeneous aquifer at Laurel Bay, South Carolina did not detect methanogenic activity in the source area five years after contaminant introduction (Landmeyer et al., 1996). The rapid development of a methanogenic zone in the NATS experiment relative to other studies may have been caused by the formation of localized anaerobic environments, the rapid depletion of other available electron acceptors (particularly iron(III)), and/or a shorter acclimation period for microbial population due to previous PHC exposure during MADE-2.

Model predicted PHC concentrations were particularly sensitive to changes in the NAPL mass transfer rate ( $k^{NAPL}$ ) and, for toluene and p-xylene, the starting concentration of bioavailable iron(III). Model sensitivity to  $k^{NAPL}$  indicates that field studies are needed to test various NAPL dissolution models and develop methods for estimating *in situ* NAPL mass transfer parameters, while sensitivity to the starting iron(III) concentration suggests a need for accurate analytical techniques for measuring bioavailable iron(III). The results of this study also indicate that the PHC concentration distribution at Snapshot 3 was better simulated using a single porosity, linear sorption model, relative to the dual domain model, but that the differences between the two models were minimal by Snapshot 4. At the time of this study, SEAM3D did not have the capability to combine dual domain transport with sorption to the solid phase and sequential electron acceptor biodegradation. Future research may show that use of a dual domain transport model may improve model calibration if all natural attenuation processes can be simulated.

SEAM3D mass balance calculations for the calibrated single porosity model provided a unique method for evaluating the NATS experiment. Model calculations indicated that aerobic biodegradation transformed more total PHC than any other natural attenuation process. This finding was not uniform for all PHCs, as results from the calibrated model also indicated that sorption was the dominant natural attenuation process for ethylbenzene and naphthalene. The calibrated model predicted that the importance of iron(III)-reduction to toluene and p-xylene transformation was increasing with time, but that the

mixing of ambient dissolved oxygen and nitrate at the edges of the PHC plume resulted in a continuous contribution of all TEAP processes to natural attenuation during the NATS experiment.

## Acknowledgements

Primary funding for this work was received from the Strategic Environmental Research and Development Program (SERDP) of the U.S. Department of Defense, Environmental Protection Agency, and Department of Energy, as part of Project CU-1062, “Development of Simulators for In-Situ Remediation Evaluation, Design, and Operation”. The contract that funded this study was procured by the U.S. Army Engineer Research and Development Center, Waterways Experiment Station, the lead agency for SERDP Project CU-1062. The study presented here was part of a cooperative effort among the Tennessee Valley Authority, the U.S. Air Force Armstrong Laboratory, the University of Alabama, and Virginia Polytechnic Institute and State University. The Chief of Engineers, U.S. Army Corps of Engineers, has granted permission to publish this paper. Additional funding for this project was received from the Via Foundation of the Charles E. Via, Jr. Department of Civil and Environmental Engineering at and Virginia Polytechnic Institute and State University.

This paper benefited from discussions with Carlos Ruiz, and from reviews by and discussion with Mark Dortch, Mark Boggs, and Hank Julian. Appreciation is also extended to Chunmaio Zheng and Erin Feehley for providing the local-scale groundwater flow model and numerical interpretation of local hydraulic conductivity distribution. The authors also appreciate the access to field data provided by Tom Stauffer, Bill MacIntyre, and Jeff Chanton.

Table 1. Range of values for the retardation factor and first-order biodegradation rate for benzene, p-xylene, and naphthalene reported from MADE-2 (Boggs et al., 1993).

<b>Component</b>	<b>Retardation Factor</b>	<b>First-order Biodegradation Rate (day<sup>-1</sup>)</b>
Benzene	1.2-1.3	0.008-0.010
p-Xylene	1.16-1.24	0.011-0.016
Naphthalene	1.42-1.45	0.007-0.013

Table 2. Composition and chemical properties of the NAPL source for the NATS experiment. Solubility, molecular weight, and initial percentage of the NAPL (by weight) were required SEAM3D input parameters.

<b>NAPL Component</b>	<b>Solubility (mg/L)</b>	<b>Molecular Weight (g/mol)</b>	<b>% of NAPL (by weight)</b>
Benzene	1790	78.1	0.05
Toluene	500	92.1	6.6
Ethylbenzene	165	106.7	7.1
p-Xylene	185	106.7	6.9
Naphthalene	34	128.2	7.8
Decane (Inert)	0.009	142.3	71.5

Table 3. SEAM3D input parameters for aquifer, soil, and PHC sorption properties.

<b>Parameter</b>		<b>Value</b>	
Bulk density		1.77 g/cm <sup>3</sup> <sup>(1)</sup>	
Diffusion Coefficient		10 <sup>-4</sup> m <sup>2</sup> /d	
		<b>Single Porosity Model</b>	<b>Dual Porosity Model <sup>(2)</sup></b>
Porosity	Mobile	0.30	0.05
	Immobile	n/a	0.30
Dual domain mass transfer coefficient		n/a	0.0025
Retardation Factor			
	Benzene	1.20 <sup>(3)</sup>	n/a
	Toluene	1.35	n/a
	Ethylbenzene	1.35	n/a
	p-Xylene	1.35	n/a
	Naphthalene	1.45 <sup>(3)</sup>	n/a

<sup>(1)</sup> Boggs et al. (1990); <sup>(2)</sup> Julian et al. (1999); <sup>(3)</sup> Boggs et al. (1993)

Table 4. Biodegradation parameters for microbial kinetics, inhibition, electron acceptor consumption and reaction endproduct formation.

Microbial Population	$K_{x,le}^s$ (g m <sup>-3</sup> )	$K_{x,le}^e$ (g m <sup>-3</sup> )	$Y_{x,ls,le}$ (g g <sup>-1</sup> )	$g_{x,ls,le}$ (g g <sup>-1</sup> )	$z_{x,li}$ (g g <sup>-1</sup> )	$k_{le,li}$ (g m <sup>-3</sup> )
Aerobes	0.5	1.25	0.50	1.6	--	2.0
Nitrate reducers	0.5	0.5	0.30	3.4	--	1.5
Iron reducers	0.5	--	0.20	35.0	0.1	1000.0
Methanogens	0.5	--	0.00	--	0.8	--

Table 5. Maximum specific utilization rates ( $n_{x,ls,le}^{max}$ ) and initial microbial population concentration ( $M_x$ ) for each simulated electron acceptor condition. NS means that hydrocarbon biodegradation was not simulated for that electron accepting condition.

Electron Accepting Condition	Maximum specific utilization rates, $n_{x,ls,le}^{max}$ (day <sup>-1</sup> )					$M_x$ (g m <sup>-3</sup> )
	Benzene	Toluene	Ethylbenzene	p-Xylene	Naphthalene	
Aerobic	0.025	0.70	0.025	0.15	0.01	0.05
Nitrate-reducing	NS	0.35	NS	0.075	NS	0.05
Iron(III)-reducing	NS	0.07	NS	0.007	NS	0.05
Methanogenic	0.005	0.005	0.005	0.005	NS	0.10

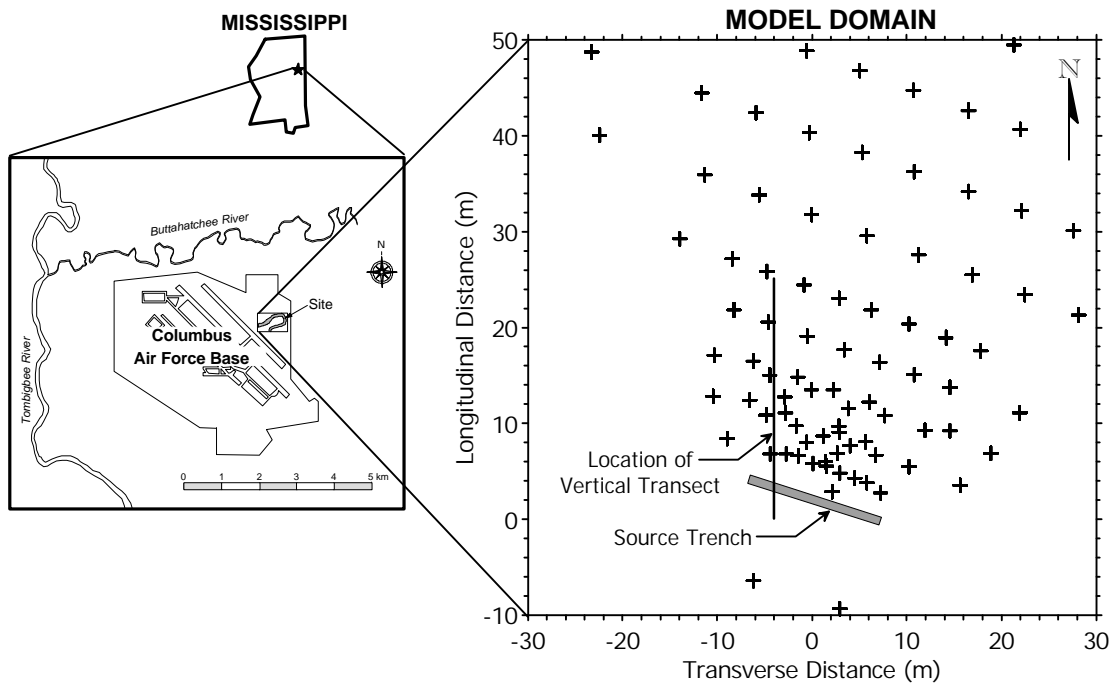


Figure 1. NATS test site location map and orientation map for model domain relative to multi-level sampling locations and the NAPL source trench location.

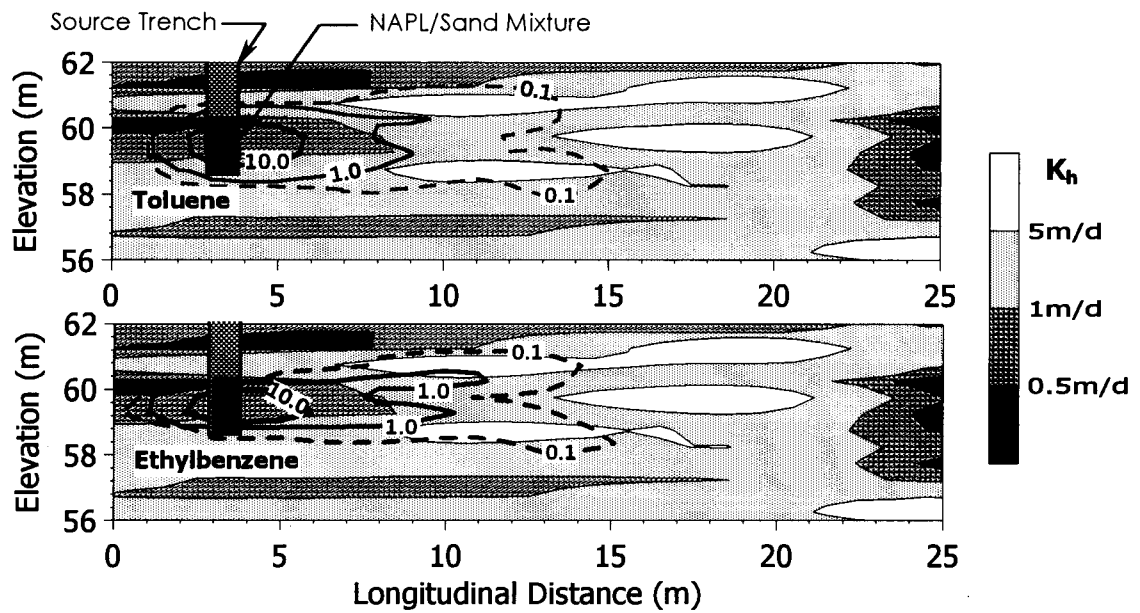


Figure 2. Correlation between contaminant contours (ppm) and hydraulic conductivity for a vertical slice taken 4 m west of the source trench centerline at Snapshot. The top figure depicts toluene concentrations, while the bottom figure is for ethylbenzene.

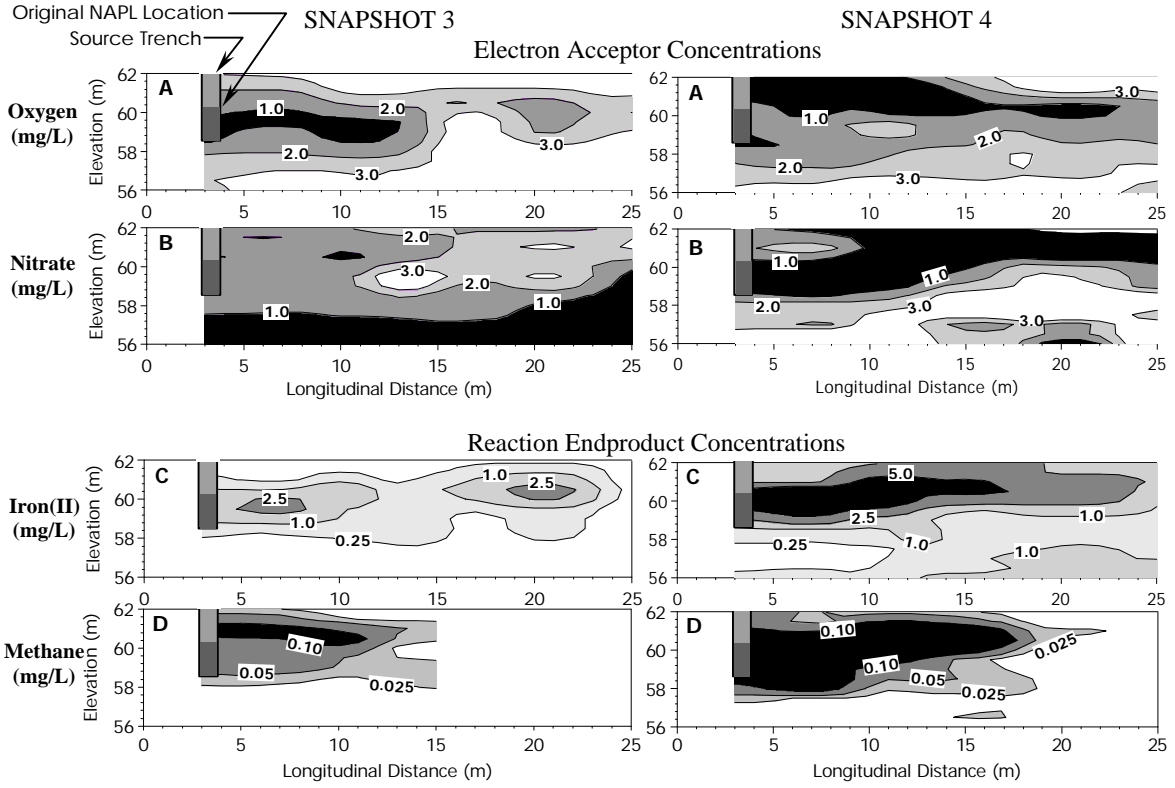


Figure 3. Electron acceptor and reaction endproduct concentration distributions at Snapshots 3 and 4. All cross sections are taken 4-m west of the source centerline, as shown in Figure 1.

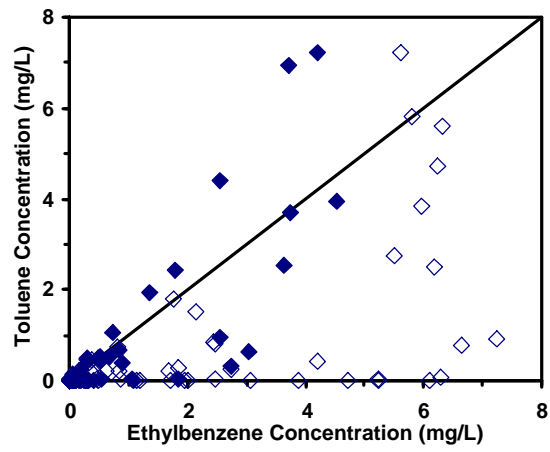


Figure 4. Comparison of field measured toluene and ethylbenzene concentrations for all monitoring points. Filled diamonds ( $\blacklozenge$ ) are for Snapshot 3 and empty diamonds ( $\lozenge$ ) are for Snapshot 4.

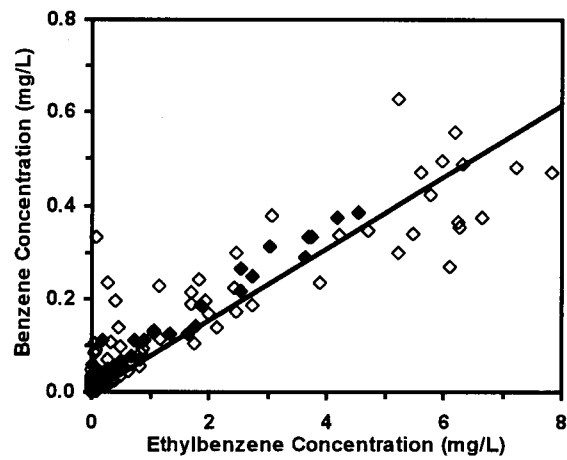


Figure 5. Comparison of field measured benzene and ethylbenzene concentrations for all monitoring points. Filled diamonds ( $\blacklozenge$ ) are for Snapshot 3 and empty diamonds ( $\lozenge$ ) are for Snapshot 4.

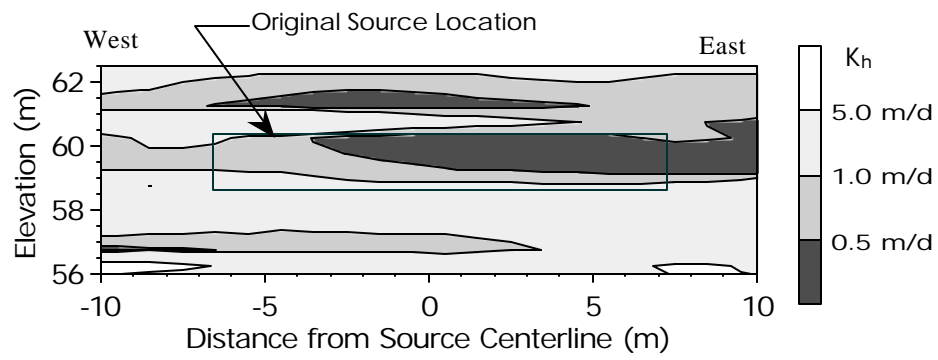


Figure 6. Hydraulic conductivity distribution immediately down-gradient of the NAPL source area.

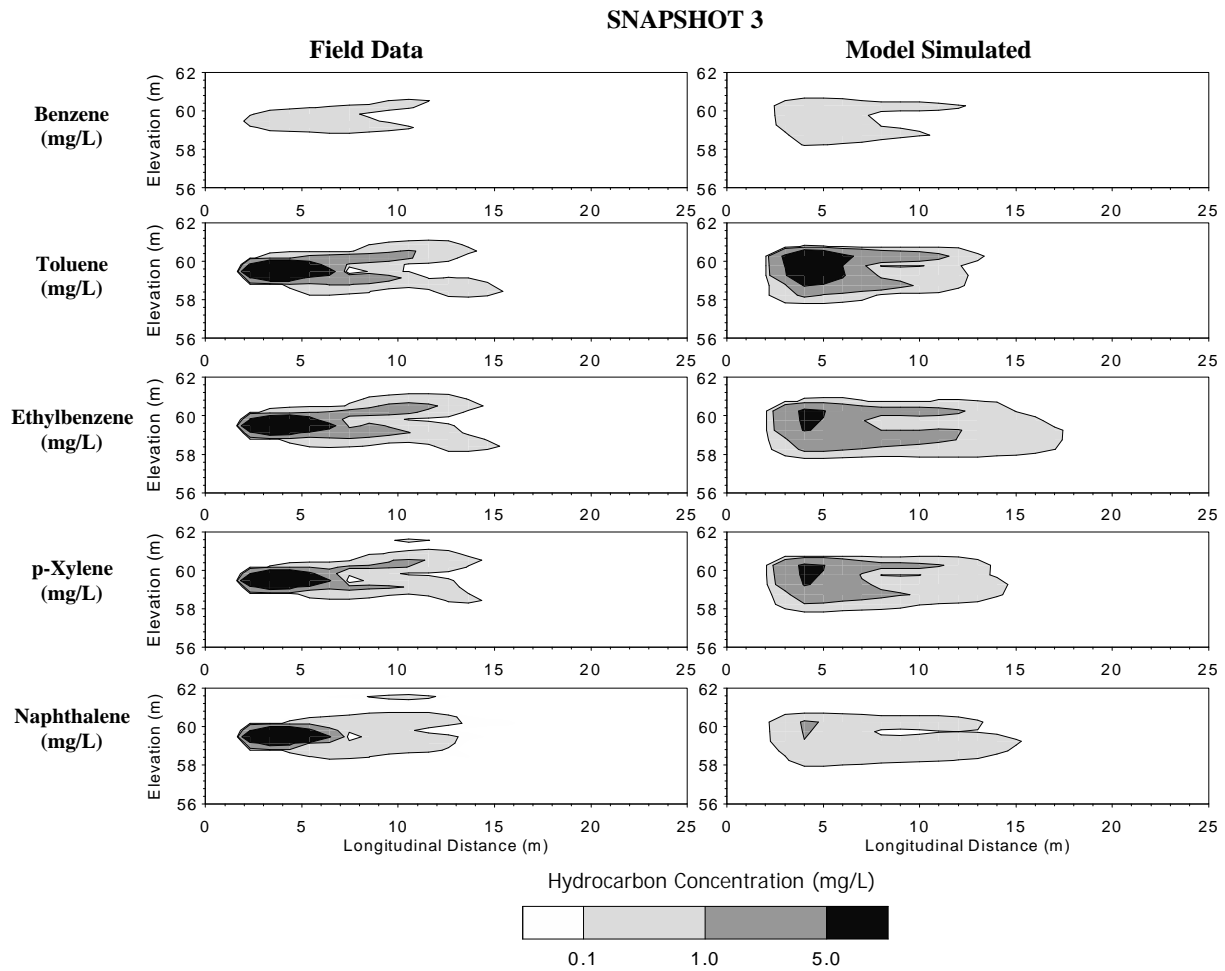


Figure 7. Comparison of field measured BTEX and naphthalene concentrations with model simulations for the single porosity model along a vertical cross section 4-m west of the source centerline for Snapshot 3.

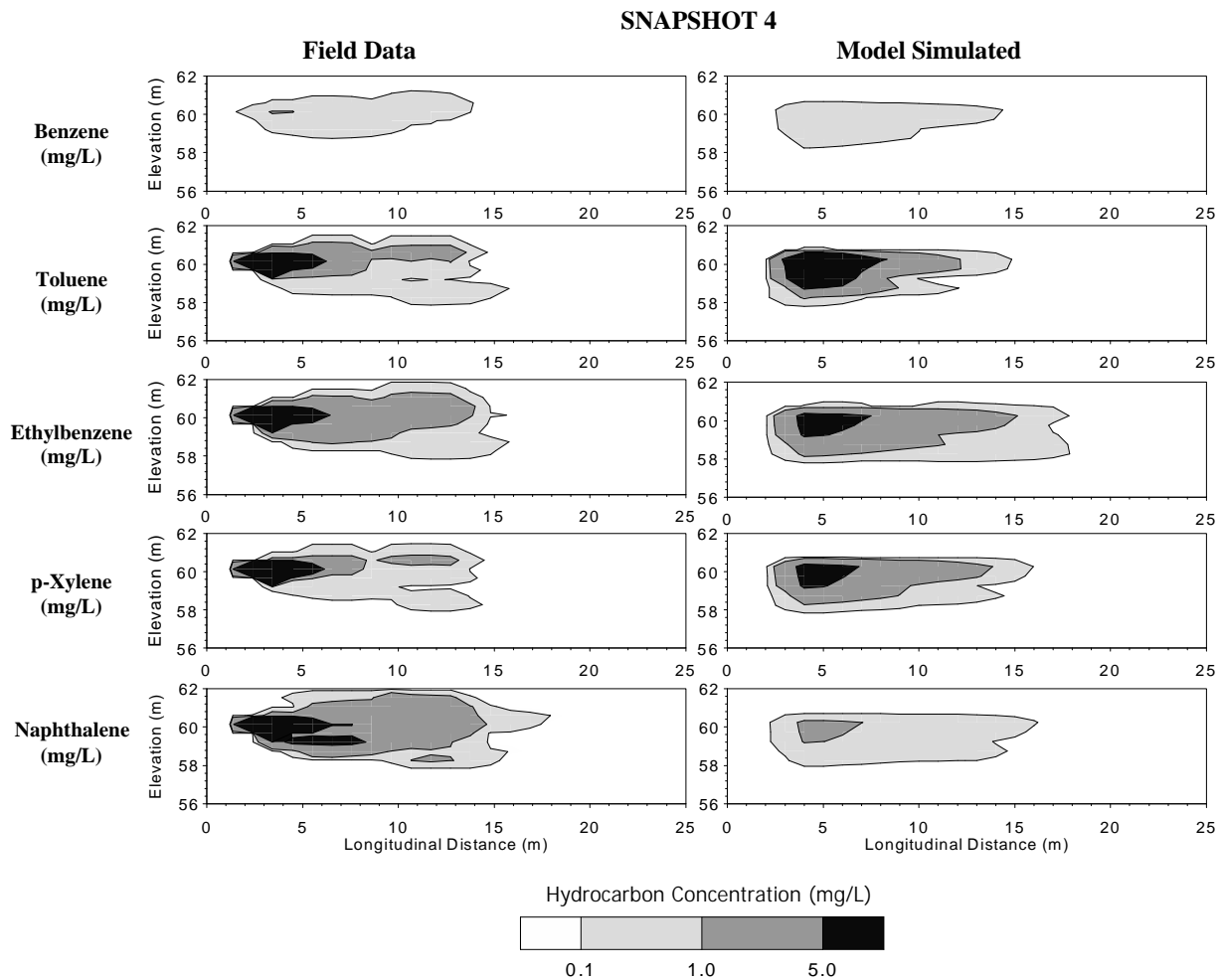


Figure 8. Comparison of field measured BTEX and naphthalene concentrations with model simulations for the single porosity model along a vertical cross section 4-m west of the source centerline for Snapshot 4.

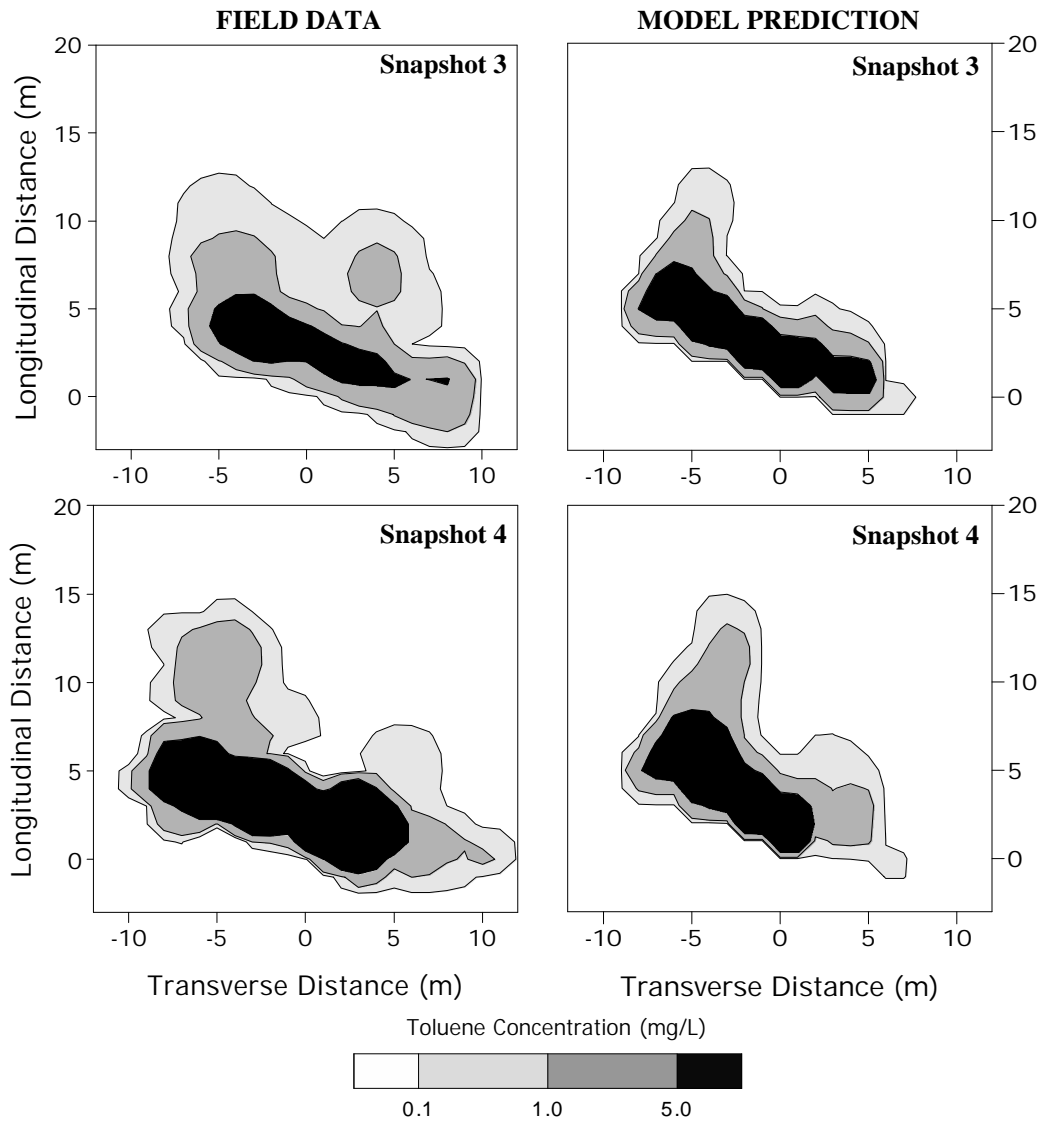


Figure 9. Comparison of field measured toluene concentrations with model simulated values for a horizontal cross section at  $z = 60\text{m}$  at Snapshots 3 and 4.

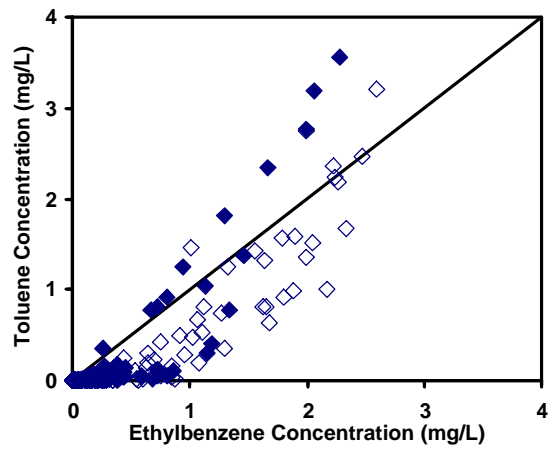


Figure 10. Comparison of model simulated toluene and ethylbenzene concentrations for all monitoring points. Filled diamonds ( $\blacklozenge$ ) are for Snapshot 3 and empty diamonds ( $\lozenge$ ) are for Snapshot 4.

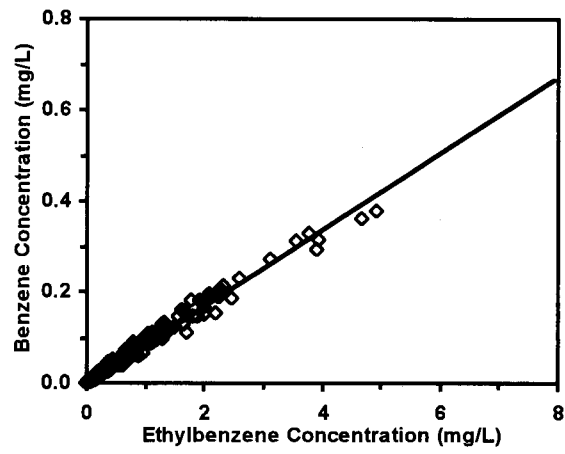


Figure 11. Comparison of model simulated benzene and ethylbenzene concentrations for all monitoring points. Filled diamonds (◆) are for Snapshot 3 and empty diamonds (◇) are for Snapshot 4.

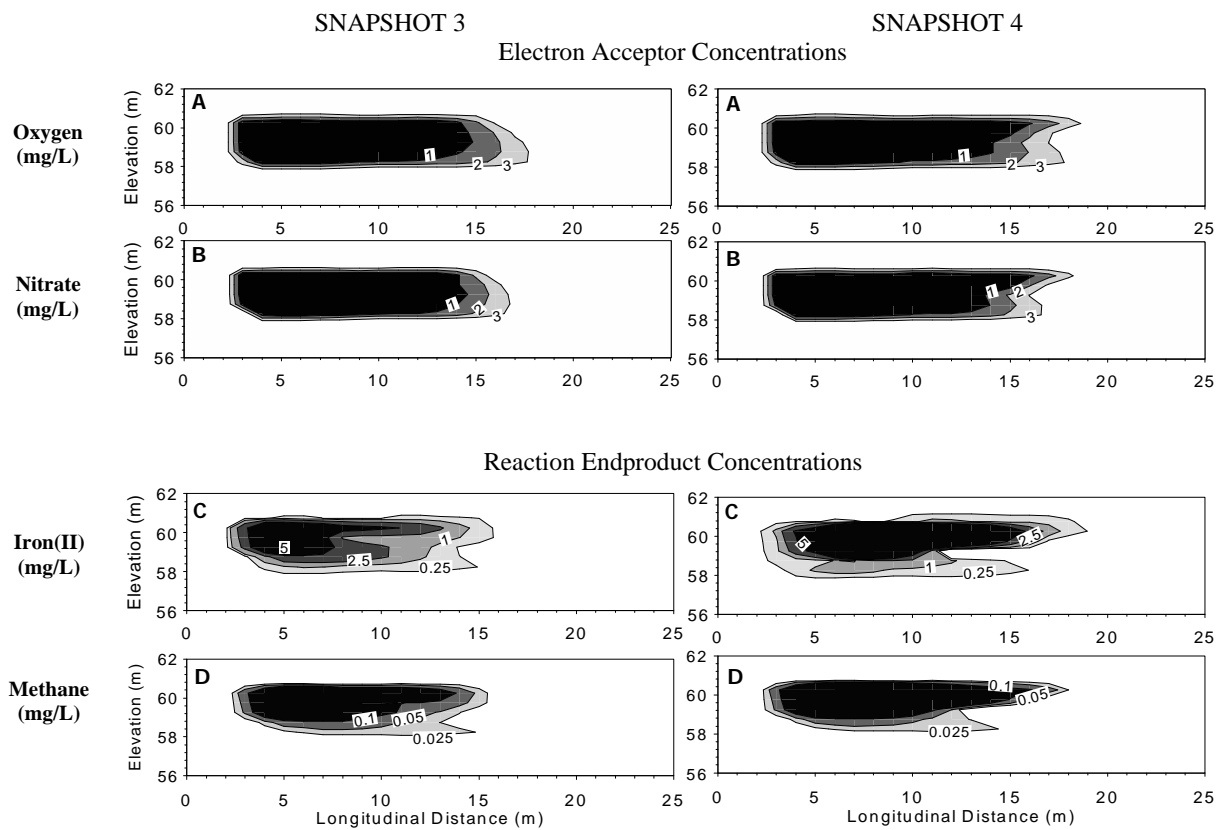


Figure 12. Model calculated electron acceptor and reaction endproduct concentration distributions at Snapshots 3 and 4 for the single porosity reactive transport model. All cross sections are taken 4 m west of the source centerline.

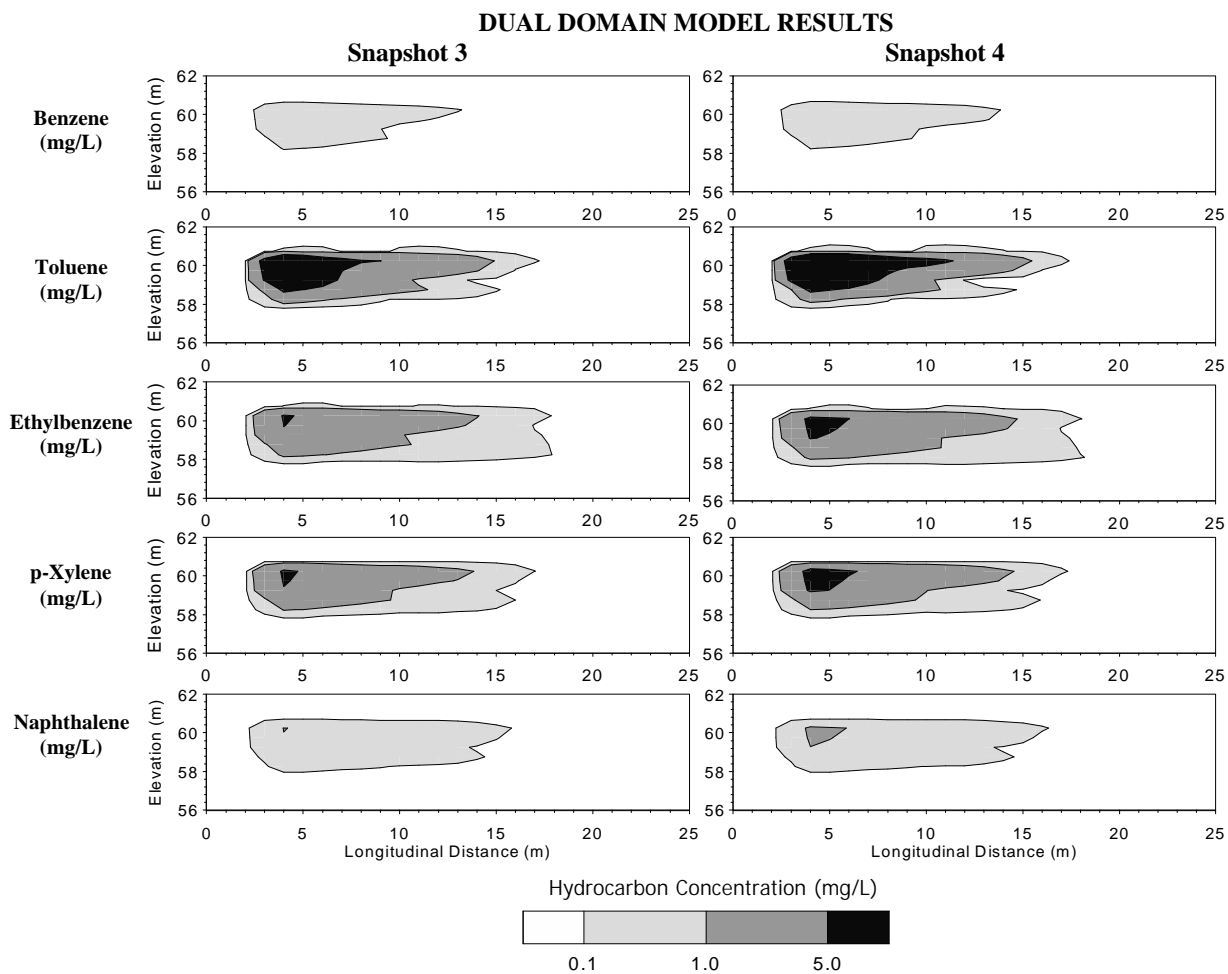
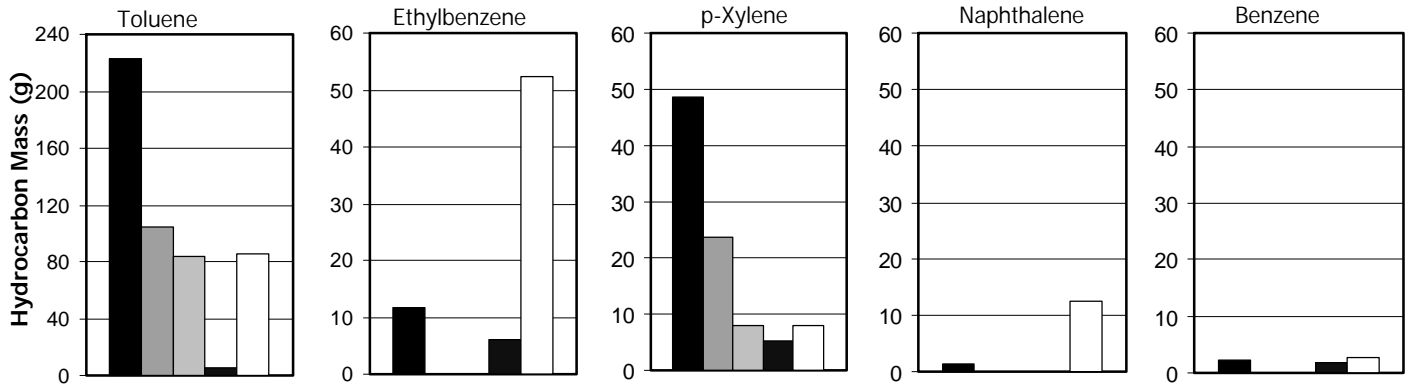


Figure 13. BTEX and naphthalene concentrations for model simulations using the dual domain reactive transport model along a vertical cross section 4-m west of the source centerline for Snapshots 3 and 4.

### Snapshot 3



### Snapshot 4

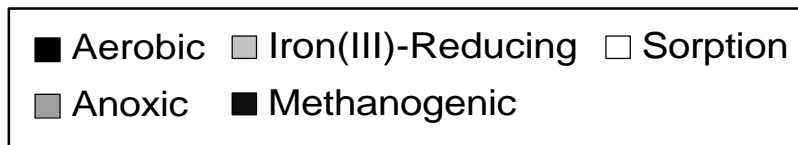
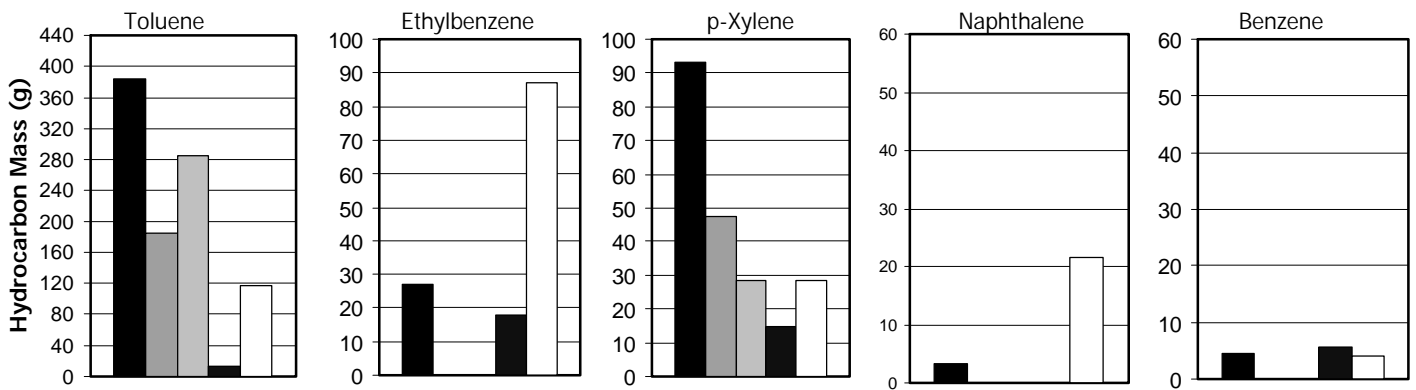


Figure 14. Mass balance calculations for hydrocarbon transformation at Snapshots 3 and 4.

## References

- Acton, D.W. and J.F. Barker. 1992. In situ biodegradation potential of aromatic hydrocarbons in anaerobic groundwaters. *J. Contam. Hydrol.* 9:325-352.
- Arcangeli, J.P. and E. Arvin. 1994. Biodegradation of BTEX compounds in a biofilm system under nitrate-reducing conditions. In: *Hydrocarbon Bioremediation*. R.E. Hinchee, B.C. Alleman, R.E. Hoepfel, and R.N. Miller (Eds.). Lewis Publishers, Boca Raton, FL. pp.374-382.
- Banerjee, S. 1984. Using models to simulate the movement of contaminants through groundwater flow systems. *CRC Critical Reviews in Environmental Control.* 9(2):97-156.
- Boggs, J.M., S.C. Young, D.J. Benton, and Y.C. Chung. 1990. Hydrogeologic characterization of the MADE site. EPRI Report EN-6915, Project 2485-05. Electric Power Res. Inst., Palo Alto, CA.
- Boggs, J.M., L.M. Beard, W.R. Waldrop, T.B. Stauffer, W.G. MacIntyre, and C.P. Antworth. 1993. Transport of tritium and four organic compounds during a natural-gradient experiment (MADE-2). *EPRI TR-101998. Research Project 2485-05*. TVA Eng. Lab., Norris, TN.
- Boggs, J.M., J.A. Schroeder, and S.C. Young. 1995. Data to support model development for natural attenuation study. *Report No. WR28-2-520-197*. TVA Engineering Laboratory, Tennessee Valley Authority, Norris, TN.
- Boggs, J.M. and W.G. MacIntyre. 2000. Manuscript in preparation.
- Borden, R.C., Daniel, R.A., LeBrun IV, L.E. and C.W. Davis. 1997. Intrinsic biodegradation of MTBE and BTEX in a gasoline-contaminated aquifer. *Water Resour. Res.* 33(5): 1105-1115.
- Borden, R.C., C.A. Gomez, and M.T. Becker. 1995. Geochemical indicators of intrinsic bioremediation. *Ground Water.* 33(2):180-189.
- Brauner, J.S. and M.A. Widdowson. 1996. Sequential electron acceptor model for evaluation of *in situ* bioremediation of petroleum hydrocarbon contaminants in groundwater. *Ann. NY Acad. Sci.* 829:263-279.
- Chang, M-K., T.C. Voice, and C.S. Criddle. 1993. Kinetics of competitive inhibition and cometabolism in the biodegradation of benzene, toluene, and p-xylene by two *Pseudomonas* isolates. *Biotechnol. Bioeng.* 41:1057-1065.
- Feehley, C.E., C. Zheng, and F. Molz. 1999. A dual-domain mass transfer approach for modeling solute transport in heterogeneous aquifers: Application to the MADE site. Submitted to *Water Resour. Res.*
- Julian, H.E., J.M. Boggs, C. Zheng, and C.E. Feehley. 2000. Numerical simulation of a natural gradient tracer experiment for the Natural Attenuation Study: Flow and physical transport. Submitted to *Ground Water*.
- Harvey, C.F. and S.M. Gorelick. 1999. Rate-limited mass transfer or macrodispersion: Which dominates plume evolution at the Macrodispersion Experiment (MADE) site? In Press *Water Resour. Res.*

- Landmeyer, J.E., Chapelle, F.H., and Bradley, P.M. (1996). Evaluation of intrinsic bioremediation as an option to contain gasoline contamination, Laurel Bay Exchange, Marine Corps Air Station, Beaufort, South Carolina. *USGS Water Res. Inv. Rep. No. 96-4026*, Denver, CO.
- Leonard, B. P. 1988. Universal limiter for transient interpolation modeling of the advective transport equations: The ULTIMATE conservative difference scheme. *NASA Technical Memorandum 100916 ICOMP-88-11*, Washington, DC.
- Libelo, E.L., T.B. Stauffer, M.A. Greer, W.G. MacIntyre, and J.M. Boggs. 1997. A field study to elucidate processes involved in natural attenuation. In: *In-situ and On Site Bioremediation, Vol.1*, B.C. Alleman and A. Leeson (Eds.). Battelle Press, Columbus, OH. pp. 23-28.
- Lovley, D.R., F.H. Chapelle, and J.C. Woodward. 1994. Use of dissolved H<sub>2</sub> concentrations to determine distribution of microbially catalyzed redox reactions in anoxic groundwater. *Environ. Sci. Tech.* 28(7):1205-1210.
- Lovley, D.R. and E.J.P. Phillips. 1986. Availability of ferric iron for microbial reduction in bottom sediments of the freshwater tidal Potomac River. *Appl. Environ. Microbiol.* 52(4):751-757.
- Lu, G., T.P. Clemet, C. Zheng, and T.H. Wiedemeier. 1999. Natural attenuation of BTEX compounds: Model development and field-scale application. *Ground Water.* 37(5):707-717.
- McCarty, P.L. 1975. Stoichiometry of biological reactions. *Progress in Water Tech.* 7(1):157-172.
- Salanitro, J.P., Wisniewski, H.L., Byers, D.L., Neaville, C.C. and R.A. Schroder. 1997. Use of aerobic anaerobic microcosms to assess BTEX biodegradation in aquifers. *Ground Water Monit. Remed.*, 17(3): 210-221.
- Stapleton, R.D., G.S. Saylor, J.M. Boggs, E.L. Libelo, T.B. Stauffer, and W.G. MacIntyre. 1999. Changes in surface catabolic gene frequencies during natural attenuation of petroleum hydrocarbons. Submitted to *Environ. Sci. Technol.*
- Stauffer, T.B., J.M. Boggs, and W.G. MacIntyre. 1997. Ten years of research in groundwater transport studies at Columbus Air Force Base, Mississippi. In: *Biotechnology in the Sustainable Environment*, K. Davis, J. Sanseverino, and G.S. Saylor (Eds.).
- US Environmental Protection Agency. 1999. Use of monitored natural attenuation at Superfund, RCRA corrective action, and underground storage tank sites. *U.S. Environmental Protection Agency OSWER Directive 9200.4-17P*.
- Vroblesky, D.A. and F.H. Chapelle. 1994. Temporal and spatial changes of terminal electron-accepting processes in a petroleum hydrocarbon-contaminated aquifer and the significance for contaminant biodegradation. *Water Resour. Res.* 30(5):1561-1570.
- Waddill, D.W. and M.A. Widdowson. 1998. Three-dimensional model for subsurface transport and biodegradation. *ASCE J. Environ. Engr.* 124(4):336-344.
- Waddill, D.W. and M.A. Widdowson. 1997. SEAM3D: A numerical model for three-dimensional solute transport and sequential electron acceptor-based biodegradation in groundwater. *Documentation and User's Guide*. US Army Corps of Engineers Waterways Experiment Station, Vicksburg, MS.

- Wiedemeier, T.H., M.A. Swanson, J.T. Wilson, D.H. Campbell, R.N. Miller, and J.E. Hansen. 1995. Patterns of intrinsic bioremediation at two U.S. Air Force bases. In: *Intrinsic Bioremediation*, R.E. Hinchee, J.T. Wilson, and D.C. Downey (Eds.). Battelle Press, Columbus, OH. pp. 31-51.
- Zheng, C. and J.J. Jiao. 1998. Numerical simulation of tracer tests in a heterogeneous aquifer. *ASCE J. Environ. Engr.* 124(6) 510-516.
- Zheng, C. and P. Wang. 1999. MT3DMS: A modular three-dimensional transport model for simulation of advection, dispersion, and chemical reactions of contaminants in groundwater systems. *Contract Report SERDP-99-1*. U.S. Army Engineer Research and Development Center, Vicksburg, MS.

## VITA

John Steven Brauner was born on 25 May 1971 in Harrisburg, Pennsylvania. Steve was married to Jennifer L. Thomason on 7 August 1999 in Hershey, Pennsylvania, five years after they met at an ultimate frisbee tournament in Savannah, Georgia.

Steve earned his Bachelor's Degree in Civil Engineering with honors from Lehigh University in 1993 and his Masters' Degree in Civil Engineering from Virginia Tech in 1995. Following completion of his dissertation, Steve continued his research at Virginia Tech as a Post Doctoral Researcher.